High-Density Hydrogen Monolayer Formation and Isotope Diffusion in Porous Media

High-Density Hydrogen Monolayer Formation and Isotope Diffusion in Porous Media

Von der Fakultät Mathematik und Physik der Universität Stuttgart
zur Erlangung der Würde eines Doktors der Naturwissenschaften
(Dr. rer. nat.) genehmigte Abhandlung

Vorgelegt von
Rafael Balderas Xicohténcatl
aus Puebla, Mexiko

Hauptberichterin: Prof. Dr. G. Schütz

Mitberichter: Prof. Dr. T. Pfau

Tag der mündlichen Prüfung : 22.11.19

Max-Planck-Institut für Intelligente Systeme
Stuttgart
2019

Al maestro, amigo y guía
Dr. Ciro Falcony

Declaration

I hereby declare that except where specific reference is made to the work of others, the contents of this dissertation are original and have not been submitted in whole or in part for consideration for any other degree or qualification in this, or any other university. This dissertation is my own work and contains nothing which is the outcome of work done in collaboration with others, except as specified in the text and Acknowledgements.

Rafael Balderas Xicohténcatl
Stuttgart
2019

Zusammenfassung

Die Erzeugung von Energie aus erneuerbaren Quellen mit CO_2-neutralen Emissionen stellt politische, wirtschaftliche, technologische und wissenschaftliche Herausforderungen, die in den nächsten Jahrzehnten angegangen werden müssen. Produktionsschwankungen, die den erneuerbaren Quellen eigen sind, schränken die Anwendbarkeit in großem Maßstab ein und erfordern effiziente und schnelle Energiespeichersysteme.
Wasserstoff als Energiespeicher hat die höchste gravimetrische Energiedichte unter allen chemischen Brennstoffen und wird als attraktiver Energieträger für mobile Anwendungen derzeit intensiv erforscht und diskutiert. Er kann durch Spaltung des Wassermoleküls mittels Elektrolyse hergestellt und direkt als Brennstoff (über seine Verbrennung) oder zu Stromerzeugung (über eine elektrochemische Zelle) verwendet werden. In beiden Fällen rekombiniert Wasserstoff mit Sauerstoff und ergibt nur Wasser in einem CO_2-freien geschlossenen Kreislauf.
Neben der Druck- und chemischen Speicherung kann molekularer Wasserstoff auch durch Physisorption in einem Feststoff mit genügend großen inneren Oberflächen gespeichert werden. Die Wechselwirkung zwischen Gasmolekülen und der festen Oberfläche über Dispersionskräfte (Van-der-Waals-Wechselwirkung) weist aufgrund der geringen Polarisierbarkeit des H_2-Moleküls typicherweise niedrige Adsorptionsenergien (1-10 kJ/mol) und, was die Anwendbarkeit auf niedrige Betriebstemperaturen ($\sim$77 K) beschränkt. Ein großer Vorteil der

Wasserstoffphysisorption ist allerdings die schnelle Kinetik, geringe Wärmeentwicklung und vollständige Reversibilität.
Die neuartigen Metal-Organic Frameworks (MOFs) besitzen einstellbare und genau definierte Porenstrukturen mit spezifischen Oberflächen, die das Doppelte der besten Aktivkohle erreichen können. Dies hat zu Materialien mit einer gravimetrischen Speicherkapazität des H_2 (H_2 Kapazität pro Masseneinheit) von über 12 wt% bei kryogenen Temperaturen geführt [1, 2]. Die Erzeugung hoher spezifischer Oberflächen fällt jedoch typischerweise mit niedrigeren Dichten der porösen Strukturen zusammen und verringert somit die volumetrische Kapazität (H_2 Kapazität pro Volumeneinheit) [3]. Kürzlich wurde die gravimetrische und volumetrische Aufnahme für viele MOFs mit der Oberfläche korreliert, was eine durchschnittliche Wasserstoffoberflächendichte von $1{,}9{\cdot}10^{-2}$ mg/m^2 ergab [3]. Dies entspricht einem intermolekularen (H_2-H_2) Abstand von 4,74 Åund ist damit größer als der Abstand in festem (3,76 Å) und flüssigem (4,05 Å) Zustand. Bereits vor ca. 70 Jahren gab es jedoch experimentelle Indizien, dass sich in graphit-ähnlichem Kohlenstoff bei 20 K eine etwa 2 mal höhere Dichte formierten könnte [4], was in weiteren Arbeiten seit 1990 auch in Silikat beobachtet wurde [5, 6]. Obwohl diese deutliche Zunahme der adsorbierten Schichtdichte (oder die Verringerung des intermolekularen Abstandes H_2-H_2) von großer grundlagenphysikalischer sowie technologischer Bedeutung für die Speicherkapazität sein sollte, wurde das Phänomen wenig beachtet, kontrovers diskutiert und blieb unverstanden.
Ein weiterer wichtiger Aspekt für die Wasserstoffwechselwirkung in porösen Materialien ist die Diffusion, charakterisiert durch den Diffusionskoeffizienten. Die Kinetik von H_2 sowie D_2 ist von vielfältigem grundlegendem, materialwissenschaftlichem sowie technologischem Interesse. Sie spielt auch eine große Rolle bei der Möglichkeit poröse Strukturen zur Isotopentrennung auf der Basis des Quantensiebens zu nutzen. Der experimentelle Zugang zu Wasserstoffkinetik bei tiefen Temperaturen beschränkte sich allerdings auf die äußerst anspruchsvolle Methode der quasi-elastischen Neutronenstreuung und war im Labormaßstab bisher nicht möglich.

Diese Arbeit konzentriert sich daher auf diese zwei grundlegenden Aspekte der Wasserstoffphysisorption:
In umfassenden, systematischen Studien wurde die **Dichte der ersten adsorbierten Wasserstoffschicht** bei niedrigen Temperaturen ($\sim$20 K) an Strukturen mit unterschiedlichen Oberflächentopologien untersucht, die nahezu ebene bis zu fragmentierte Oberflächen enfassen. Es wurden mehrere Proben von porösem Siliziumdioxid und Kohlenstoff mit großen Porengrößen (> 10 nm) analysiert, die ein Beispiel für eine flache Oberfläche im Vergleich zur Größe des H_2 (2,89 Å) darstellten. Als Modellmaterial wurde das geordnete mesoporöse Siliziumdioxid KIT-6 untersucht, das aus einem wohl definierten 3D-Netzwerk mit ausschließlich Mesoporen einer engen Porengrößenverteilung von 10 nm besteht. Zusätzlich wurden poröse und nicht poröse Siliziumdioxid Nanopartikel untersucht, um einen Einfluss der Porengröße oder reduzierten Dimension auf die H_2-Adsorption auszuschließen. Zum weiteren Vergleich wurden kohlenstoffbasierte Materialien mit unterschiedlichen Porositäten herangezogen. Dazu gehören der graphitisierte Kohlenstoff Carbopack-B als Beispiel einer flachen und chemisch homogenen Oberfläche, die frei von funktionellen Hydroxylgruppen ist. Als Prototyp fragmentierter Oberflächen wurde MOF-205 aus der neuen Klasse der MOFs mit extrem hohen Oberflächen ausgewählt.
Eine hochauflösende Gasadsorptionsapparatur, die in der Lage ist Drücke von nur 10^{-8} bar zu messen, die an einen Kryokühler mit geschlossenem Kreislauf gekoppelt ist, wurde zur Charakterisierung der Oberflächen bei extrem niedrigen Drücken verwendet. Die Adsorption von vier verschiedenen Gasen (Ar, N_2, H_2 und D_2) bei ihrer Kondensationstemperatur wurde verglichen. Es konnte die adsorbierte Phase von H_2 untersucht und cleren Schichtdichte bei 20,37 K bestimmt werden, indem die Monoschichtkapazität von H_2 und D_2 mit der durch Ar gemessenen spezifischen Oberfläche verglichen wurde.
In allen untersuchten Beispielen für ebene Oberflächen (Siliziumdioxid und Kohlenstoff) ergibt die H_2-Monoschichtkapazität bei Kondensationstemperatur (20,37 K) im Vergleich zu den anderen untersuchten Gasen (Ar (87,3 K) und N_2 (77,3 K)) fast zweimal mehr Moleküle pro Fläche. Die Dichte der 2D-Schicht aus

adsorbiertem Wasserstoff ist mehr als doppelt so hoch wie die Dichte von festem Wasserstoff (80.0 kg/m^3) und bis zu 200 kg/m^3 groß. Solche hohen Dichten entsprechen kurzen intermolekularen Abständen in der Größenordnung von 2,9 Å oder molekularen Querschnittsflächen von 7,1 Å^2. Die wert ist signifikant kleiner als im H_2-Feststoff (3.76 Å).

An der Hochfluss-Neutronen-Spallationsquelle am Oak Ridge National Laboratory liefert das neue Schwingungsspektrometer VISION eine inelastische Zählrate, die mehr als zwei Größenordnungen über vergleichbaren verfügbaren Instrumenten liegt. Dies ermöglichte erstmals die Untersuchung der Bildung der Wasserstoffschicht *in situ* durch inelastische Neutronenstreuung (INS) für unterschiedliche adsorbierte Mengen und Temperaturen mit bisher noch nie erreichter Auflösung.

Inelastische Neutronenstreuungexperimente an allen Siliziumdioxidproben zeigen zwei Energieübergänge (11 und 14 meV) bereits ab dem ersten Beladungspunkt, der 0,125 Monolagen entspricht. Die beiden Rotationsmaxima bei 11 und 14 meV liegen in der Nähe der Energie des freien Rotors von H_2 (14,5 meV). Dies weist darauf hin, dass die hochdichte 2D-Schicht ähnliche Eigenschaften wie die feste Phase von Wasserstoff (feststoffartig) besitzt. Beide Rotationsübergänge werden anhand des Evett-Modells erklärt. Die energetisch niedriger liegende Linie bei 11 meV kann hierbei einer gehinderten Rotation bzw. Rotationsbarriere durch die Anwesenheit von Hydroxylgruppen auf der Siliziumdioxidoberfläche zugeordnet werden. Für einen graphitisierten Kohlenstoff zeigen die INS-Spektren nur einen Peak nahe 14,5 meV, was sich durch das Fehlen von Hydroxylgruppen an der Oberfläche einfach erklären lässt.

Diese Kombination der Adsorptionsisothermen mit den INS-Spektren zeigt zum ersten Mal einen eindeutigen Hinweis für die Bildung einer hochdichten 2D-Wasserstoffschicht auf ebenen Oberflächen.

Die hohe Dichte der 2D-Schicht aus adsorbiertem Wasserstoff bei niedriger Temperatur wird unter Verwendung von *ab initio* Berechnungen der intermolekularen H_2-H_2 Wechselwirkung für eine Adsorptionsstärke im Bereich von 1 bis 10 kJ/mol beschrieben. Für einen typischen Wert der H_2-Adsorptionsstärke ($\sim$4

kJ/mol für Siliziumdioxid) beträgt die intermolekulare H_2-H_2 Wechselwirkung 0,6 kJ/mol (6 meV), was signifikant geringer ist als die Adsorptionswechselwirkung. Die kleine intermolekulare Wechselwirkung führt zu einem geringen intermolekularen Abstand ($\sim$2,9 Å), d.h. einer hochdichten 2D-Schicht. Solche Dichten sind nur aufgrund der starken Kompressibilität der H_2-Monoschicht möglich. Durch das Fehlen von Rumpfelektronen ist es viel einfacher, die erste Schicht von H_2 zu komprimieren, als dies bei schwereren Elementen der Fall ist, da die Pauli-Abstoßung der Elektronenwolken beim Überlappen bei der Komprimierung erheblich schwächer ist.
Im Gegensatz zu flachen Oberflächen mit einer hochdichten 2D-Phase wurde die H_2-Adsorption an der fragmentierten Oberfläche eines metallorganischen Gerüsts MOF-205 untersucht. Bei dieser Art von Oberflächen werden die H_2-Moleküle an lokalisierten Adsorptionsstellen mit einer mittleren Dichte nahe der von flüssigem Wasserstoff adsorbiert. Die INS-Experimente mit Wasserstoff, der an MOF-205 adsorbiert ist, zeigen ein komplexes Spektrum, das sich aus mehreren Peaks in der Nähe des freien Rotors (14,5 meV) zusammensetzt, die sukzessive mit zunehmender Dosierung auftreten. Dies bedeutet, dass zuerst die energetisch stärksten Adsorptionsplätze besetzt und anschließend die schwächeren Plätze gefüllt werden.
Diese systematischen Experimente zusammen mit den Berechnungen der Gruppe von Thomas Heine erklären die in den letzten 70 Jahren beobachtete, aber nie vollständig verstandene Phase adsorbierten Wasserstoffs mit hoher Dichte. Dies hochdicht Wasserstoff könnte eine interessante Rolle für kryogene Wasserstoffspeichersysteme mit extrem hohen Speicherkapazitäten spielen.

Die Untersuchung der **Diffusion von Wasserstoffisotopen in porösen Materialien** erfordert gewöhnlich anspruchsvolle experimentelle Anordnungen der Neutronenstreuung. Im zweiten Teil dieser Arbeit wird eine Methode zur Untersuchung der Wasserstoffisotopendiffusion in porösen Materialien vorgestellt, die auf der Messung der Adsorptionskinetik durch einen Sieverts-Apparat basiert.

Das Framework ZIF-8 ist ein Modellmaterial zur Untersuchung der Wasserstoffspeicherung und -diffusion basierend auf seiner relativ großen Oberfläche (∼1200 m^2/g) und engen Porenöffnung (3,4 Å) in der Nähe des kinetischen Durchmessers von H_2 (2,9 Å). Jüngste Fortschritte in der Synthese von MOFs durch die Gruppe von D. Fairen-Jimenez an der Universität Cambridge ermöglichen die Herstellung von ZIF-8 als Monolith mit makroskopischen Dimensionen [7].
Die Diffusion von H_2/D_2 in ZIF-8 bei niedriger Temperatur wird an zwei Proben mit unterschiedlicher Partikelgröße untersucht; Monolithe (∼3 mm) und Pulver (60 - 70 nm). Die Oberfläche beider Proben wurde unter Verwendung von Ar-Isothermen charakterisiert und zeigte, dass Monolithe und Pulver eine nahezu identische Oberfläche und Porenstruktur besitzen. Mit einer hochauflösenden Adsorptionsapparatur, die in der Lage ist, bis zu kleinsten Drücken von nur $1{\cdot}10^{-8}$ bar zu messen, wurden H_2 und D_2 Adsorptionsisothermen aufgenommen. Die Temperatur wurde mit einem geschlossenen He-Kryokühler geregelt, der Temperaturen herunter bis zum Siedepunkt von Wasserstoff (∼20 K) mit hoher Stabilität (±0,05 K) erreicht. Für jeden Dosierungsschritt der Isotherme wurde der zeitliche Verlauf des Drucks bis zum Erreichen des Gleichgewichtsdrucks, der typischerweise erst nach mehreren Stunden erreicht wurde, gemessen. Ein Modell basierend auf dem 2. Fick'schen Gesetz mit Randbedingungen für kugelförmige poröse Partikel wurde zur Analyse der Adsorptionskinetik verwendet und damit die Diffusionskoeffizienten berechnet.
Die Messung der Adsorptionskinetik ist begrenzt durch die zeitliche Auflösung und Temperaturstabilität der Adsorptionsapparatur. Die kleine Partikelgröße (∼60 nm) der Pulverprobe resultiert in einer sehr schnellen Adsorptionskinetik (in der Größenordnung von Sekunden). Folglich mussten für den Einsatz dieses Verfahrens Partikel mit makroskopischer Größe (*i.e* Monolithen) herangezogen werden, die in Kombination mit niedrigen Temperaturen (∼20 K) Wasserstoffdiffusionszeiten in der Größenordnung von Stunden pro Dosierungspunkt ergeben. Die H_2- und D_2-Diffusionskoeffizienten dieser Monolithen nehmen mit zunehmender Gasaufnahme ab. Eine solche Verringerung des molekularen Transports ist mit einer struktureller Umwandlung des Materials bei Gasadsorption

gut erklärbar. Der Imidazolat-Linker von ZIF-8 schwingt mit wachsender Temperatur im mer stärke in Richtung der Porenöffnung und verringert so deren Größe, was mit den Adsorptionsexperimenten von Ar und N_2 übereinstimmt und aus der Literatur bekannt ist.
Ein zehnmal höherer D_2-Diffusionskoeffizient im Vergleich zu H_2 wird bei hoher Aufnahme und nahe der Kondensationstemperatur ($\sim$20 K) beobachtet, was darauf hinweist, dass die verringerte Porenöffnung nicht nur den molekularen Transport begrenzt, sondern auch das kinetische Quantensieben (KQS) verbessert, was zu einem schnelleren Transport des schweren Isotops (D_2) führt. Das vorgestellte Verfahren verwendet eine handelsübliche Adsorptionsapparatur, um die Tieftemperatur-Adsorptionsisothermen von H_2/D_2 zu messen zu können und gleichzeitig die H_2/D_2-Diffusivitäten als Funktion von Temperatur und Gasaufnahme zu berechnen. Hiermit kann gezeigt werden, dass Adsorptionsexperimente zur Untersuchung der Wasserstoffdiffusion und der Isotopentrennung nahe der Kondensationstemperatur erfolgreicht verwendet werden können.

Contents

List of Figures

List of Tables

Chapter 1

Introduction and motivation

The generation of energy by renewable sources with CO_2 neutral emissions set political, economic, technological and scientific challenges that require to be addressed during the next decades. Production fluctuations, inherent to the renewable sources, limit the applicability on a large scale and demand efficient and rapid energy storage systems.

Hydrogen as energy storage medium has the highest gravimetric energy density among all chemical fuels. Therefore, H_2 is currently being intensively investigated and discussed as an attractive source of energy for mobile applications. It can be produced by splitting the water molecule by electrolysis and used directly as fuel (via its combustion) or for power generation (via an electrochemical cell). In both cases, hydrogen recombines with oxygen yielding only water in a CO_2-free closed cycle.

Under ambient conditions, hydrogen is a volatile gas with a volumetric density that is too low for practical applications. The commercially available hydrogen storage systems are based on the physical compression in high-pressure tanks requiring pressures as high as 700 bar; on the other hand, liquid storage requires temperatures close to boiling $\sim$20 K. Alternatively, hydrogen can be stored also in solid-state materials via the chemical bonding of atomic hydrogen (chemi-

sorption) or by the physical adsorption (physisorption) on large-surface-area materials.

In chemisorption, hydrogen is bonded to the bulk solid forming a hydride by either metallic, ionic or covalent bonds with high volumetric storage capacities. Because the high interaction energy of the chemical bonding ($\sim$ 200 kJ/mol [2 eV]), hydrides usually require additional thermal management.

On the other hand, molecular hydrogen can be stored on a solid by physisorption given by the interaction between gas molecules and the solid surface via dispersive forces (van der Waals interaction). In consequence, H_2 physisorption is restricted to low operating temperatures ($\sim$77 K) due to the low polarizability of the H_2 molecule that results in low adsorption energies (1-10 kJ/mol [10-100 meV]). As an advantage, hydrogen physisorption exhibits fast kinetics and full reversibility.

Physisorption of hydrogen is governed by the surface of the storage medium with a linear correlation between the specific surface area (area per unit of mass) and the H_2 gravimetric capacity given by the so-called Chaine's rule [8]. This empirical relation establishes a proportion where 500 m^2/g of surface area is equivalent to 1 wt% of hydrogen capacity at 77 K [1].

In consequence, porous materials with high specific surface area are desired to store molecular hydrogen. Porous carbons [9] and zeolites [10] have been extensively studied with the H_2 highest uptake given by activated carbons (5.5 wt%) possessing surface areas over 3000 m^2/g. The novel metal-organic frameworks (MOFs) possess tunable and well-defined pore structures with specific surface areas that can be as high as double of the best activated carbon. These materials provide high H_2 gravimetric storage capacities (H_2 capacity per unit of mass) up to 12 wt% at cryogenic temperatures [1, 2]. However, the generation of high specific surface areas typically coincides with lower densities of the porous structures, considerably reducing the volumetric capacity (H_2 capacity per unit volume) [3]

Recently, the gravimetric and volumetric uptake was correlated to the surface area for many MOFs, resulting in an average hydrogen surface density of $1.9{\cdot}10^{-2}$

mg/m^2 [3]. The surface density can be understood as the amount of H_2 molecules per unit of area and is equivalent to an intermolecular (H_2-H_2) distance of 4.74 Å, which is larger than the H_2-H_2 distance in solid (3.76 Å) and liquid (4.05 Å) states. Hence, the increase of the adsorbed layer density (or the reduction of the intermolecular distance H_2-H_2) is of enormous importance as it is directly related to the increase of both volumetric and gravimetric H_2 storage capacities of a porous material.

Already 60 years ago, there was experimental evidence that indicated a H_2 adsorbed layer with approximately 2 times higher density in graphite-like carbon at 20 K [4], which was observed in silicate in a further works in 1990 [5, 6] and in 1997 [11]. Although this significant increase in the adsorbed layer density (or the reduction of the intermolecular distance H_2-H_2) should be of great fundamental physical as well as technological importance for the storage capacity, the phenomenon has received little attention, has been controversially discussed and remained unanswered.

Another important aspect of the hydrogen interaction in porous materials is diffusion, characterized by the diffusion coefficient. The kinetics of adsorption of H_2 and D_2 is of great interest from a fundamental and technological point of view. It also plays a major role in the ability to use porous structures for isotopic separation based on quantum sieving. However, the experimental measurement of hydrogen kinetics at low temperatures, has been limited to the extremely sophisticated methods, such as quasi-elastic neutron scattering, and was previously not possible on a laboratory scale.

This work focuses on these two fundamental aspects of hydrogen physisorption at temperatures close the boiling point ($\sim$20 K): First, the density of a single layer of adsorbed hydrogen molecules is studied for different reference surfaces. Secondly and equally important, the diffusion of the hydrogen molecules through a porous framework is investigated by adsorption experiments.

Density of adsorbed hydrogen at low-temperature

The hydrogen molecule possesses a low molecular mass, and a weak intermolecular potential that result in fascinating properties of the liquid and solid phase only comparable with He. One particular characteristic of solid hydrogen is the high compressibility due to the absence of multiple electron shells. Applying a pressure of 100 bar to hydrogen in solid state results in the decrease of the volume of 5% [12], whereas other solids are barely compressible (*e.g* argon changes its volume only by 0.8%).
The adsorption of light gas molecules such as H_2 (or He) has been studied since the 1940s, with some reports revealing unusually high He and H_2 capacities in the first adsorbed layer (monolayer) [13, 14] in comparison to other gases such as Ar, N_2 or CO_2. In 1956, Steele [15] introduced a phenomenological model using the concept of a double layer adsorption (bilayer) in order to explain the high He monolayer capacities on carbon. Pace and Siebert [4] reported a large discrepancy between the monolayer capacities of nitrogen (77 K) and hydrogen (20 K) on carbon suggesting a short intermolecular H_2-H_2 distance (2.95 Å) that can be interpreted as hydrogen forming a high-density layer. Even some investigations have focused on the adsorption of H_2 and show similar high monolayer capacities [5, 16, 17], there exist still a debate between to two hypotheses claiming the formation of a bilayer of adsorbed hydrogen and the formation of an exotic high-density monolayer.

In this work, comprehensive and systematic studies have been done to investigate the density of the first adsorbed hydrogen layer at low temperatures ($\sim$20 K) on structures with different surface topologies, ranging from nearly flat surfaces to fragmented surfaces. Several samples of porous silica and carbon that possess large pore size (>10 nm, *i.e.* with curvatures larger than 0.1 nm^{-1}) were analyzed representing an example of a quasi-flat surface in comparison to the size of the H_2 (2.89 Å). As a prototype of fragmented surfaces, MOF-205 was chosen from the new class of MOFs possessing extremely high surface areas ($\sim$4000 m^2/g).

A high-resolution gas adsorption apparatus that is capable to measure pressures as low as 10^{-8} bar coupled to a closed-cycle cryocooler was used to characterize the surfaces at ultra-low pressures. The adsorption isotherms of four different gases were studied for each material in order to estimate the H_2 layer density. The high-flux neutron spalation source at Oak Ridge National Laboratory in combination with the state-of-the-art spectrometer VISION allow the study the formation of an adsorbed H_2 layer with an unprecedented resolution. *In situ* Inelastic Neutron Scattering (INS) provide direct information of the intermolecular interactions H_2-H_2 by following the rotation-vibration of H_2 molecule during the layer formation.

The combination of the adsorption isotherms with the INS spectra shows for the first time clear evidence of the formation of an unusual high-density 2D layer of hydrogen on flat surfaces. The corresponding density of the H_2 layer obtained in several silica and carbon surfaces is more than two times the bulk-solid density. INS spectra of silica show two energy transitions (11 and 14 meV) located close to the free-rotor energy of H_2 (14.5 meV) which is a transition only observable for solid hydrogen. First-principles calculations including nuclear quantum effects by the group of Thomas Heine were used to rationalize the high-density phase. The model explains the high-density layer by the low intermolecular interaction ($\sim$0.6 kJ/mol) that is significantly less than the interaction H_2-solid ($\sim$4 kJ/mol for silica surfaces).

Hydrogen isotope diffusion at low-temperature

Transport or diffusion is one of the processes governing the temporal character of adsorption in porous materials that takes place before adsorption equilibrium is reached. The kinetics of adsorption consist of the entrance of gas particles at the opening of the channels that later diffuse into the pore structure until reaching equilibrium.

The understanding of hydrogen diffusion in porous materials is crucial to improve the practical applications such as fast energy storage or effective gas separation.

The loading and unloading of a physisorption hydrogen tank is a key parameter in the development of such technology that directly depends on the kinetics of the hydrogen adsorption. Hydrogen diffusion in microporous materials can even be exploited to efficiently separate isotope mixtures by kinetic quantum sieving (KQS).
KQS was theoretically proposed by Beenaker *et al.* [18] in 1995 as a promising way to separate light isotopes using porous materials with reduced pore dimensions close to the molecular kinetic diameter ($d(H_2) = 2.89$ Å). In such confinement, the adsorption and diffusion of isotopes are mainly governed by the molecular mass. As a result, the separation factor, *i.e.* selectivity, of a given material depends directly on the diffusion rate of a given isotope.
In order to systematically study gas diffusion, a material with well-defined pore structure, *i.e.* pore size and aperture size, is required. MOFs are excellent candidates for the study of diffusion [19] due to their well-defined and tunable pore structures and the potential to introduce strong adsorption sites directly into the framework structure [20].

Microscopic techniques to study H_2/D_2 diffusion, such as quasi-elastic neutron scattering [21, 22] and pulsed-field gradient NMR, need to be coupled with low-temperature environments ($\sim$20 K) and gas loading devices; with only a few reports of direct measurements of the H_2/D_2 diffusion in micropores [23, 24]. Thermal desorption spectroscopy measures the desorption kinetics of different molecules species while rampling the temperature [20]. However, the simultaneos change of time and temperature makes an analysis of the diffusivity complex and model dependent [25]. On the other hand, H_2/D_2 diffusion can be evaluated analyzing the adsorption kinetics, which can be followed measuring the time-dependence of the pressure for each point of an adsorption experiment.

In the second part of this work, a method to study hydrogen isotope diffusion in porous materials is presented, which is based on the measurement of adsorption kinetics by a Sieverts' apparatus.

The metal-organic framework ZIF-8 (Zeolitic Imidazolate Framework 8) is a model material for the study of hydrogen storage and diffusion due to its pore aperture (3.4 Å) close to the kinetic diameter of the H_2 molecule (2.9 Å) and relatively large surface area ($\sim$1200 m^2/g). Two samples of ZIF-8 were synthesized as powder (60 - 70 nm) and monoliths ($\sim$3 mm) by the group of D. Fairen-Jimenez at Cambridge University, which allow the direct comparison of the adsorption kinetics of the same structure but different particle size.

A high-resolution adsorption apparatus, capable to measure pressures as low as $1 \cdot 10^{-8}$ bar, was used to collect H_2 and D_2 isotherms and the adsorption kinetics. The device was coupled with a closed-cycle cryocooler allowing the measurement of the adsorption kinetics at low temperatures ($\sim$20 K) with unprecedented temperature stability ($\pm$ 0.05 K). For each dose step of the isotherm, the time-dependence of the pressure was measured until equilibrium pressure was reached. A model based on Fick's second law was used to analyze the adsorption kinetics and thus calculate the diffusion coefficients.

The slow adsorption kinetics in the large particles of the monolith sample combined with the temperature stability of the measurements allowed for the first time the measurement of the hydrogen diffusivity by a commercial adsorption device at temperatures close to boiling temperature ($\sim$20 K). As proof-of-principle, the diffusivity of deuterium was compared to hydrogen; at boiling temperature, D_2 ($\sim 1 \cdot 10^{-8}$ m^2/s) has a diffusivity higher than H_2 ($\sim 1 \cdot 10^{-9}$ m^2/s) which can be explained by the small pore aperture of ZIF-8 acting as a quantum sieve.

Chapter 2

Theoretical and experimental basis

2.1 Gas adsorption on solids

Adsorption is the result of a solid phase in contact with a fluid (*i.e. gas or liquid*); defined as increase of density of the fluid at the interface of the two bulk phases. Under certain conditions, adsorption can be accompanied by absorption, i.e. the penetration of the fluid into the solid phase. The adsorption of a fluid by a solid phase is mediated by weak dispersive forces *i. e.* van der Waals forces (for H_2 typically 1-10 kJ/mol [10-100 meV or 100 - 1100 K]), because of this, it is also known as physical adsorption or *physisorption*; while absorption involves "strong" chemical bounding of the fluid with the solid (for hydrides $\sim$200 kJ/mol [2 eV - 23000 K], also know as *chemisorption* [26].
Gas adsorption in a solid material depends on the temperature T, pressure P, and the interaction potential E between the gas (adsorbate) and the solid surface (adsorbent) [27], which is usually measured by manometry or gravimetry techniques. The adsorbed amount scales with the size of the interfacial area. Most

Table 2.1 List of terms and properties related to adsorption [26].

Term	Definition
Adsorption	Enrichment of a fluid density at solid-fluid interface
Adsorbate	Substance in the adsorbed state
Adsorptive	Adsorbable substance in the fluid phase
Adsorbent	Solid material on which adsorption occurs
Monolayer capacity	Adsorbed amount required to cover with one layer the surface
Surface coverage	Ratio amount of adsorbed substance to monolayer capacity
Powder	Dry material composed of discrete particles ($\ll$ 1 mm)
Monolith	A continuous and unbroken particle ($\sim$1 mm), with no grain boundaries
Specif surface area	Extent of available surface as determined by a given method under stated conditions
Pore volume	Volume of pores determined by stated method
Pore size	Pore width (diameter or distance between opposite walls of slit)
Micropore	Pore of internal width less than 2 nm
Mesopore	Pore of internal width between 2 and 50 nm
Macropore	Pore of internal width greater than 50 nm
Absolute pressure	Pressure zero-referenced against perfect vacuum
Relative pressure (P/P_0)	Pressure normalized by the condensation pressure P_0

adsorbents possessing large specific surface areas are highly porous or composed of fine particles. Owing to their potential to store or separate fluid species, adsorbents can be used in applications such as gas storage, gas separation, purification and catalysis. On the other hand, gas adsorption plays an important role in the characterization of surface properties and texture of fine particles and porous materials [26]. Some of the principal terms and properties are listed in Table 2.1.

Quantitative adsorption

The total gas amount n in a solid-fluid interface can be divided in two parts, the amount adsorbed n_a and the amount remaining in gas phase n_g shown in Figure 2.1a and given by

$$n = n_a + n_g = n_a + \rho_g \cdot V_g \tag{2.1}$$

where ρ_g is the bulk gas denstiy. Consequently, the evaluation of n_a requires the knowledge of the volume occupied V_g or the local concentration of the adsorbed

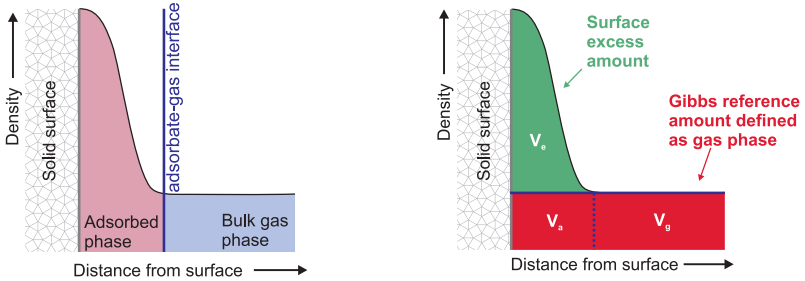

(a) *Adsorbed layer representation.* (b) *Gibbs surface excess amount.*

Figure 2.1 *Gibbs representation of the surface excess amount.* (a) The adsorbed layer is separated from the gas phase where both densities are equal by an imaginary surface parallel to the adsorbent surface (adsorbed-gas interface); (b) Gibbs excess surface amount corresponds to the adsorbed molecules additional to the amount of molecules that corresponds to gas density in absence of any interaction with the absorbent.

layer as function of the distance with the interface. Gibbs (1887) introduced the concept of surface excess to quantify the amount adsorbed [26].

Gibbs dividing surface The dividing surface proposed by Gibbs is shown in Figure 2.1b, which is defined as an imaginary surface parallel to the adsorbent surface. In this model, the red area (Fig. 2.1b) represents Gibbs reference volume $V_{g,o}$ of the system with a final equilibrium concentration ρ_g, *i.e.* the red area has the same density as the bulk gas, or represents the volume occupied by a gas in absence of any interaction with the absorbent. The *surface excess amount* n_σ of molecules is represented by green area (Fig. 2.1b) and given by the Equation 2.2.

$$n_\sigma = n - \rho_g \cdot V_{g,o} \tag{2.2}$$

where n is the total adsorptive amount, $V_{g,o}$ is the Gibbs reference volume with a bulk gas density ρ_g.

It is convenient to locate the Gibbs dividing surface, which is accessible to the adsorbed phase by dividing $V_{g,o}$ into two volumes

$$V_{g,o} = V_a + V_g \tag{2.3}$$

where V_a is the same volume occupied by the surface excess amount ($V_a = V_e$) (Fig. 2.1) and V_g is the volume occupied by the non-adsorbed gas.

Excess and absolute gas uptake Combining equations 2.1, 2.2 and 2.3, the adsorbed phase is defined as the absolute adsorbed amount, given by

$$n_a = n_\sigma + \rho_g \cdot V_a = n_\sigma + n_G \tag{2.4}$$

where n_a is defined as the *absolute adsorbed amount* given by the green area and the red area marked as V_a in Figure 2.1; and n_G is defined as $n_G = \rho_g \cdot V_a$. If $\rho_g \ll 1$ then Equation 2.4 yields $n_a \approx n_\sigma$ [26], which indicates that for low concentrations of the adsorbate (e.g. low pressure), the absolute uptake and excess uptake approximate each other.

The absolute adsorption amount is calculated from Equation 2.4 under the assumptions: (*i*) The density of the surface excess amount n_σ is equal to the bulk liquid density of the adsorbate; (*ii*) The volume of the excess surface is given by

$$V_e = V_a = \frac{n_\sigma}{\rho_{liq}} \tag{2.5}$$

The absolute adsorbed amount n_a is obtained combining Equation 2.5 and 2.4 into

$$n_a = n_\sigma + n_G = n_\sigma \left(1 + \frac{\rho_g}{\rho_{liq}}\right) \tag{2.6}$$

where ρ_g and ρ_{liq} are the bulk gas and liquid density[1], respectively.

[1] The bulk liquid hydrogen density is ρ_{liq} = 70.8 kg/m^3; bulk gas hydrogen density ρ_g used in this work was obtained by the state equation of NIST [28–30].

Gas adsorption manometry Sieverts' technique is a common tool to study gas adsortion measuring the excess adsorbed amount; it is based on the change of pressure (manometric) in a constant, calibrated system volume [31]. In this method, gas is introduced to an accurately calibrated reference volume (manifold) at a given pressure. A pressure change due to the volume change and hydrogen absorption / desorption of the sample will be measured when a valve located between the reference volume and sample cell is opened at a given temperature [26]. The excess adsorbed amount n_σ, at the equilibrium pressure and constant temperaure, is then calculated as the difference between the amount of gas admitted n_{adm} and the amount of gas required to fill the adsorbent and sample cell volume ($n_G + \rho_g \cdot V_g + n_{cell}$). An adsorption isotherm is constructed point-by-point by the successive loanding of gas to the sample cell [32].

Gas adsorption gravimetry This method is based on the measurement of the sample weight by a microbalance. The microbalance provides a direct and continuous measurement of the excess adsorbed amount of the adsorbent while the pressure is changed in steps [31], which offers some potential advantages over the Sieverts' technique, especifically, to study the adsorption kinetics [33]. A sample is typically contained in a bucket which is suspended from one side of a balance arm by a hang-down wire with a tare mass hang-down in the other side. The entire balance mechanism is pressurised and the tare weight is thus surrounded by the same pressure of gas as the sample [32]. An exact knowledge of the sample volume is necessary to correct the bouyancy in a given atmosphere, given usually by a He test. Because of the free hanging of the sample, the control and exact measurement of the temperature is challenging [33].

Isosteric heat of adsorption Adsorption is an exothermic process, since heat is liberated when a molecule is weakly bond to the surface. Simultaneously, the entropy of the system is decreased due to the loss of at least one degree of translation freedom of the adsorbed molecules. The temperature dependence

of the adsorption/desorption equilibrium vapor pressure is governed by the Clausius-Clapeyron (Eq. 2.7).

$$\frac{\Delta H_{ad}}{R} = \left(\frac{\partial lnP}{\partial \frac{1}{T}} \right)_{n_a} \tag{2.7}$$

where R is the gas constant, P is the equilibrium gas pressure, ΔH is the adsorption enthalpy change, and T is temperature for a given n_a absolute adsorbed amount. By integrating the Clausius-Clapeyron equation (Eq. 2.7) between the limits of equilibrium pressures and temperatures p_1, p_2 and T_1, T_2 combined with the so-called van't Hoff equation [34], it is possible to calculate the isosteric heat of adsorption Q_{ad} for a given surface coverage by

$$\frac{\Delta Q_{ad}}{R} = \left(\frac{ln\left(\frac{P_1}{P_2}\right)}{\left(\frac{1}{T_1} - \frac{1}{T_2}\right)} \right)_{n_a} \tag{2.8}$$

The isosteres, required to evaluate the isosteric heat of adsorption, are the pressure points at constant absolute adsorbed amounts for different temperatures ($P = f(n^a)_T$) [35]. This method of calculation based on the Clausius-Clapeyron is called *Isosteric method* [26].

Physisorption isotherms

Gas adsorption is usually described through an isotherm curve that represents the amount of adsorbate on the adsorbent as a function of its pressure at constant temperature. A recent report by the IUPAC[2] clasified the majority of physisorption isotherms into eight different groups (Fig. 2.2), with a six sub-types related to the histeresis loop [36]. In most cases, at sufficiently low surface coverages,

[2] International union of pure and applied chemestry

the isotherm reduces to a linear form which is often referred to as the Henry's Law ($n_a \propto P$).

Type I isotherms are given by microporous solids having relatively small external surfaces. The isotherm is concave to the P/P_0 axis and the amount adsorbed approaches a limiting value that corresponds to the saturation of the surface with gas molecules. *Type I(a)* isotherms are characteristic for microporous materials having mainly narrow micropores (of width < 1 nm); *Type I(b)* isotherms are found for materials having pore size distributions over a broader (of width < 2.5 nm).

Type II isotherms are characteristic for most gases on nonporous or macroporous adsorbents. The shape is the result of unrestricted monolayer-multilayer adsorption up to high P/P_0. If the knee is sharp, Point B at the beginning of the middle almost linear section, usually corresponds to the completion of monolayer coverage.

Type III isotherms, show no Point B and no identifiable monolayer formation; the adsorbent-adsorbate interactions are relatively weak and the adsorbed molecules are clustered around the most favorable sites on the surface of a nonporous or macroporous solid.

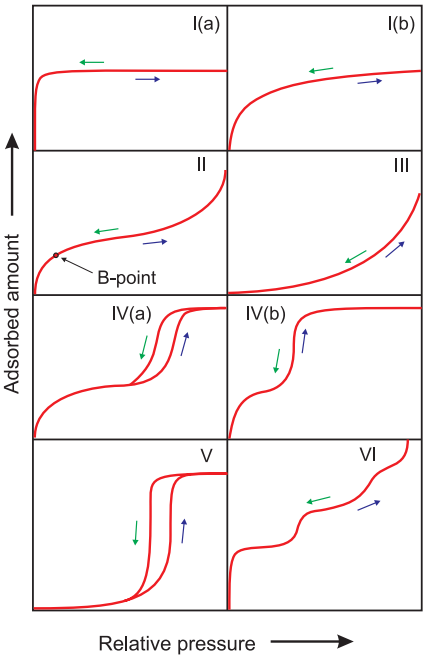

Figure 2.2 *IUPAC adsorption isotherms classification*. Each isotherm is described in the main text [36].

Type IV isotherms are characteristic for mesoporous (of width, 2 < d < 20 nm) adsorbents. The monolayer-multilayer adsorption on the mesopore walls, corresponding to the first part of a Type II isotherm, which is followed by pore condensation. A typical feature of Type IV isotherms is a final saturation plateau. *Type IV(a)* isotherm, capillary condensation is accompanied

by a hysteresis. *Type IV(b)* isotherms are completely reversible, and observed for adsorbents having mesopores of smaller width.
Type V isotherm shape is very similar to that of Type III and this can be attributed to relatively weak adsorbent–adsorbate interactions. At higher P/P_0, molecular clustering is followed by pore filling.
Type VI isotherm is representative of layer-by-layer adsorption on a highly uniform nonporous surface. The step-height now represents the capacity for each adsorbed layer, while the sharpness of the step is dependent on the system and temperature [27, 36, 37].

Hysteresis and capillary condensation The hysteresis loops observed for isotherms type IV(a) and V are related to the capillarity condensation that occurs when the pores are filled with a condensed liquid of the adsorbate. The adsorbed liquid phase is condensate below the condensation pressure, P_0, due to the overlapping of van der Waals potential in a narrow pore and the confinement of the adsorbate molecules inside the capillary. Once condensation occurs, a meniscus is formed at the liquid-gas interface, which depends of the surface tension of the liquid and the shape of the pore, allowing the equilibrium of the liquid phase below the condensation pressure.

BET theory

In 1938, Brunaer, Emmet and Teller (BET) [38] proposed an extension model to the Langmuir kinetic treatment of monolayer adsorption [39]. The BET theory assumes that the molecules in the uppermost adsorbed layer are in equilibrium with the adsorbate gas, additionaly, the model assumes a multilayer with infinite thickness at $P/P_0 = 1$ [27]. The BET equation developed using kinetic theory can be found somewhere else [26, 27], which is usually expressed as

$$n = n_m \left(\frac{C \cdot P}{(P_0 - P)\left[1 + (C-1)\left(\frac{P}{P_0}\right)\right]} \right) \tag{2.9}$$

where n_m is the monolayer capacity and C is an empirical constant related to the interaction of the gas with the solid surface.
The success of the BET theory (Eq. 2.9), lies in its ability to describe and explain the three distinctive regions in the pressure domain using a minimal number of parameters. After an almost vertical increase at low pressures, related to the monolayer formation; the isotherm converges to a plateau with a much smaller positive slope, forming of the second and higher order layers; to then finally diverge asymptotically at P/P_0 =1 due to the unlimited adsorption at saturation pressure [40]. Furthermore, the BET theory enables an experimental determination of the number of molecules required to form a monolayer [27, 36].

BET area The "BET area" is calculated from monolayer capacity n_m [39] obtained from the isotherm fit with Equation 2.9 and requires, as prerequisite the knowledge of the molecular cross-section area of the adsorbate. Typically, two main assumptions are necessary to calculate the cross-sectional area; (i) the density of the adsorbed layer is close to the bulk-liquid density of the adsorbate; (ii) the adsorbed molecules form a hexagonal-close-packed layer [26, 27]. Equation 2.10 which relates the molecular cross-sectional area σ and the volumetric density ρ of the bulk adsorbate, assuming that the adsorbed molecules form a hexagonal close-packed layer.

$$\sigma = f(m/\rho N_A)^{2/3} \tag{2.10}$$

where f = 1.091 is the hexagonal close-packed factor, m is the molar mass and N_A is the Avogadro number [26, 27].
The monolayer capacity can be multiplied by the molecular cross-sectional area to calculate the BET area

$$SSA_{BET} = n_m \cdot \sigma \cdot N_A \tag{2.11}$$

where SSA_{BET} is the BET area in [m^2/g], n_m is monolayer capacity in [mol/g], and σ is the molecular cross-sectional area in [m^2]. The requisite of the *prior* knowledge of the molecular cross-sectional area is usually surpassed by assuming a density in the monolayer equal to the bulk liquid and a hexagonal close-packing arrangement. Additionally, the fitting procedure is sensitive to the relative pressure range used in the calculations; an commonly used range is (0.05 - 0.3 P/P_0) [40].

BET in microporous materials The application of the BET method on materials with micropores is not straightforward because the monolayer–multilayer adsorption and micropore filling processes may occur at the same relative pressures [39, 41]. This limits the number of materials for which the BET area can be regarded as the physical area to non-porous, macroporous, or mesoporous solids (i.e. materials which give rise to a type II or a type IV isotherm of the IUPAC (Fig. 2.2 [36]). A useful procedure was introduced by Rouquerol *et al.* [42] using two simple criteria: no negative value of C; and the term $n_a(P_0 - P)$ should continuously increase. Following this two criteria, the linear BET range can be determined and the BET areas of different microporous materials can be compared [41]; the BET area in this case has no physical meaning and it is necessarily not equal to the specific surface area.
Argon (87K) is preferably use as probe to measure surface areas because it possesses a spherical symmetry and no quadrupole moment [41, 43]. The cross-sectional area of argon at 87 K is 14.2 $Å^2$; calculated assuming a bulk-liquid density of the adsorbed phase and a hexagonal close-packing distribution [26].

Pore volume: Gurvich rule The pore volume V_{pore} can be derived from the adsorbed amount at a relative pressure close to unity using the Gurvich rule. This simple method assume pores are completely filled with liquid adsorbate at pressures close to condensation, and it given by

$$V_{pore} = n_{fill}/\rho_{liq} \tag{2.12}$$

where V_{pore} is the specific pore volume, n_{fill} is the adsorbed amount of gas at the relative pressure P/P_0 close to 1 (e.g. $P/P_0 = 0.95$), and ρ_{liq} is the liquid density of the adsorbate [41]. If a mesoporous adsorbent contains macropores, the isotherm is no longer horizontal near $P/P_0 = 1$ and the total pore volume cannot be evaluated [36].

Density functional theory: Pore size distribution Density functional theory (DFT) is a computational modelling method used in physics, chemistry and materials science to investigate the structure of many-body systems, in particular atoms, molecules, and the condensed phases. Using this theory, the properties of a many body systems can be determined by using functionals, i.e. functions of another function, which in this case depend on the molecular density. In particular, density functional theory (DFT) can be used to study adsorbed fluids using the grand potential (Landau free energy) $\Omega(\rho)$ which is the characteristic state function for the grand canonical ensemble. It is constructed with the Helmholtz free energy $F(\rho)$ expressed as function of the density distribution of the system, the chemical potential μ and the density distribution of particles in the system $\rho(\vec{r})$.

$$\Omega(\rho) = F(\rho) - \mu \int d\vec{r}\rho(\vec{r}) \tag{2.13}$$

$F(\rho)$ includes fluid-fluid interaction (attractive and repulsive) and the solid-fluid interaction potential. The density distribution $\rho(\vec{r})$ is calculated for all locations in the pore by minimizing a the grand potential $\Omega(\rho)$ in equilibrium with a bulk phase with respect to functional variations in $\rho(\vec{r})$ using the condition

$$\left[\frac{\delta\Omega}{\delta\rho(\vec{r})}\right]_{\mu,T} = 0 \tag{2.14}$$

that yields a non-linear integral equation solved by iterative methods [44].
DFT provides a qualitatively reasonable description of adsorption in pores, however, it is quantitatively inaccurate especially in the range of micropores

where the density changes abruptly. A significant improvement in accuracy was obtained with the non-local density functional theory (NLDFT) [41].
NLDFT is used to describe the local fluid structure near curved solid walls based on the intermolecular potentials of the fluid-fluid and solid-fluid interactions. The method calculates the equilibration density distribution $\rho(\vec{r})$ of a fluid adsorbed on surfaces and in pores from which properties such as the adsorption/desorption isotherm, heat of adsorption, and transport properties for model systems can be derived.
A set of adsorption isotherms ($N(P/P_0,W)$) corresponding to model pores, *e.g cilindrical, spherical pores*, with different pore sizes (W) are then determined from the density profiles which constitute the kernel of the model that depend on the adsorbate (gas), temperature, adsorbent (material) and pore geometry. The relation between kernel isotherms and the experimental isotherm on a porous solid can be interpreted in terms of a generalized adsorption isotherm equation:

$$N(P/P_0) = \int_{W_{min}}^{W_{max}} N(P/P_0,W) f(W) dW \tag{2.15}$$

where $N(P/P_0)$ are experimental adsorption isotherm data, W is the pore width, $N(P/P_0,W)$ is a set of isotherms (kernel) with a pore of width W, $f(W)$ is the pore size distribution function. The model assumes that the total isotherm $N(P/P_0)$ consists of a number of individual "single pore" isotherms multiplied by their relative distribution, $f(W)$, over a range of pore sizes. The set of $N(P/P_0,W)$ isotherms (kernel) for a given system (adsorbate/adsorbent) can be obtained, as indicated above by density functional theory computer simulation. The pore size distribution $f(W)$ is then derived by solving the equation 2.15 numerically [45].
A further improvement was realized by quantitatively allowing for variations in surface heterogeneity through a "quenched solid" (QSDFT) approach. The QSDFT approach allows both the fluid and solid density profiles to vary in order to correlate the molecular level geometric heterogeneity of real pore walls to the solid density profiles [46].

The pore size distribution was calculated using the kernel of the software ASiQwin v3.0 that uses the isotherm of the material (N_2 or Ar) as input data, the temperature, and requires an assumption of the pore geometry (slit pores, cilindrical, spherical).

2.2 Molecular hydrogen storage on porous media

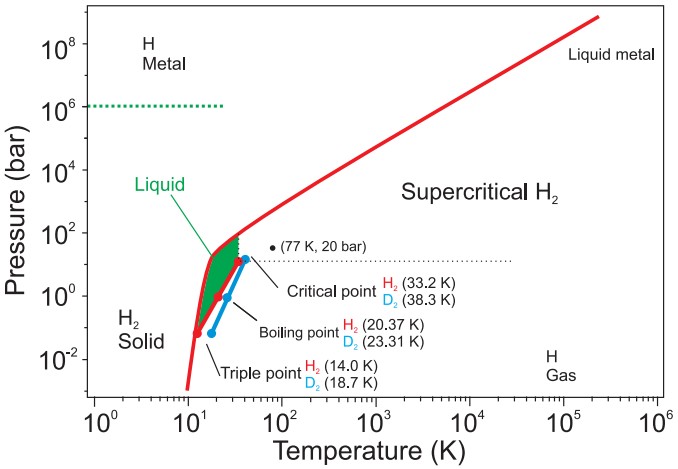

Figure 2.3 *H_2 phase diagram.* H_2 (red) and D_2 (blue) triple, boiling and critical points are indicated at the respective temperature. The typical conditision employed to measure H_2 capacity (77K, 20 bar) (black point). Figure adapted from [47].

Molecular hydrogen has a low polarizability, a boiling point of 20.37 K, and a critical point of 33.2 K, that yield a relatively low interaction when is adsorbed in a surface. Figure 2.3 shows the phase (P-T) diagram of H_2 indicating that liquid H_2 can only exist in a small region of temperature, 14.0 - 33.2 K, or for the case of D_2 18.7 - 38.3 K. Consequently, a sub-critical experiment with hydrogen requires temperatures below 33.2 K, *e.g.* BET surface area or pore condensation determination.

Due to the weak interaction between the hydrogen molecule and a solid surface (1-10 kJ/mol), a significant amount of adsorbed hydrogen is only observed at cryogenic temperatures [47–49]. Hence, the hydrogen storage capacity of porous materials is typically measured with an adsorption experiment at 25 bar (2.5 MPa) and 77 K (∼6 meV), *i.e.* super-critical temperature. Additionally, the specific surface area is obtained by the BET method from an independent adsorption experiment with nitrogen (77 K). Recently, Argon (87 K) has been proposed as the optimum gas to measure the specific surface area due to its spherical symmetry and lack of quadruple moment [36].
The units of hydrogen adsorbed amount or uptake n can be given in STP volume per gram [cc/g] or in units molecules of H_2 per gram [mg/g] or [mol/g]. However, most of the reports use [wt%] which is defined as the percentage hydrogen adsorbed amount $n_{H_2}[g]$ compared to the mass of the system (sample + adsorbed phase)

$$n[wt\%] = \frac{n_{H_2}}{m_{sample} + n_{H_2}} \tag{2.16}$$

Chaine´s rule A linear correlation between the hydrogen uptake at 77 K and the BET area was proposed by R. Chahine for porous carbons [1, 8]. Chahine's rule relates the gravimetric absolute hydrogen uptake of porous materials to the specific surface area using a linear relation given by

$$n = \kappa \cdot SSA_{BET} \tag{2.17}$$

where n is the absolute adsorbed amount per unit of mass, κ ($1.9{\cdot}10^{-2}$ mg/m^2 from [3]) is the hydrogen surface density and SSA_{BET} is the BET area. Such linear relation states that for every 500 m^2/g of surface area, the material will have a 1 wt% of hydrogen uptake. Figure 2.4 show the experimentally determined H_2 absolute uptake vs the BET area of different MOFs and porous carbon (AX-21) studied at 25 bar (2.5 MPa) and 77 K [3].

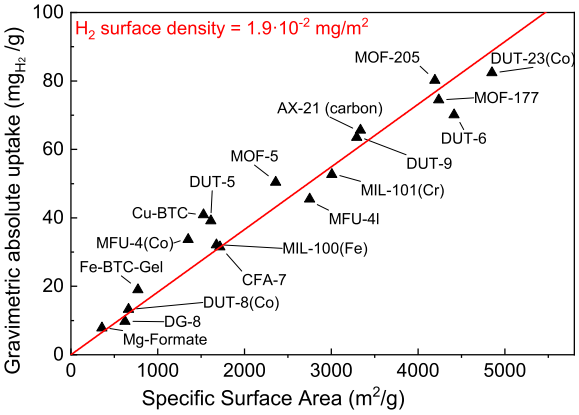

Figure 2.4 *Chahine's rule: Gravimetric hydrogen capacity vs specific surface area of MOFs at 2 MPa and 77 K.* The slope of the so-called Chahine's rule is the surface density of hydrogen molecules per square meter obtained for many MOFs in addition to the porous carbon AX-21.

The average H_2 surface density at 77 K ($1.9{\cdot}10^{-2}$ mg/m^2 [3]) can be converted to a molecular cross-sectional area yielding 17.6 Å^2. Assuming a 3D hexagonal close packing distribution (Eq. 2.10), the H_2 surface density can be converted to a corresponding volumetric density (51.6 kg/m^3), which is near below to the bulk-liquid density at 20.37 K (ρ_{lq} = 70.9 kg/m^3). Consequently, the corresponding volumetric density of hydrogen adsorbed on MOFs (at 77 K, 3.5 MPa) is around 35% lower than the bulk-liquid density.

2.3 Gas diffusion on porous media

Gas diffusion is the process by which particles are transported from an area of high concentration to one of low concentration as a result of random motions, thereby approaching a uniform equilibrium state [50, 51]. The rate of this

movement (diffusion coefficient) is a function of temperature, viscosity of the medium, and the size and mass of the particles.
Graham's law of diffusion states that the mixture of two gases is, for each gas, inversely proportional to the square root of its molecular weight. A. Fick (1885) recognized the observation of Graham as analogy with the heat conduction, which is also due to random molecular motions, and described using the same form of Fourier's law of heat conduction. The first law of Fick defines the diffusivity or diffusion coefficient D in units of [m^2/s]:

$$J = -D\frac{\partial C}{\partial x} \tag{2.18}$$

where J is the flux of particles per unit of area [mol/m^{-2}·s^{-1}] and C is the concentration of the diffusion substance in the x direction of the particle transport [mol/m^{-3}]. Fick´s second law is given by Equation 2.19, which describes the concentration change as function of time, which is derived from Fick's first law and the mass conservation equation $\left(\frac{\partial C}{\partial t} + \nabla J = 0\right)$.

$$\frac{\partial C}{\partial t} = \nabla \cdot (D\,\nabla C) \tag{2.19}$$

If the diffusion is restricted to a radial symmetry, the diffusion equation for a constant diffusion coefficient takes the form:

$$\frac{\partial C}{\partial t} = \frac{\partial^2 C}{\partial r^2} + \frac{2}{r}\frac{\partial C}{\partial r} \tag{2.20}$$

with the solution given by

$$\frac{M_t}{M_\infty} = 1 - \sum_{n=1}^{\infty} \frac{1}{n^2} \exp\left(-\frac{D\pi^2 n^2 t}{a^2}\right) \tag{2.21}$$

assuming an infinite amount of gas surrounding the spherical particle.
Assuming that the porous media (spherical particle of radius a) is submerged in a container of finite volume V, which implies a decrease of the density of the gas when part of it is adsorbed in the porous particle. The total amount concentration

inside the spherical particles, assuming a finite volume of the gas container and a uniform gas concentration, is given by the solution:

$$\frac{M_t}{M_\infty} = 1 - \sum_{n=1}^{\infty} \frac{6\alpha(\alpha+1)}{9+9\alpha+\alpha^2 q_n^2} \exp\left(-\frac{Dq_n^2 t}{a^2}\right) \tag{2.22}$$

where q_n is given by equations the: $\tan q_n = \frac{q_n}{3+\alpha q_n^2}$ and $\alpha = \frac{V_{reservoir}}{v_{particle}}$.

2.4 Inelastic neutron scattering

Neutrons are nuclear particles that have no electrical charge, no electrical dipole momentum, and mainly interact with the atoms nuclei (by strong interaction) or with the local magnetic field created atoms and ions (by magnetic interaction due its magnetic moment).

Neutrons scattering types *i.e.* elastic and inelastic scattering are determined by the speed of the neutrons (energy), and by the neutron cross section. The cross-sections is characteristic of each nuclei isotope (or by the atomic magnetic moment) and is independent of the chemical enviroment. Elastic scattering involves no change in energy of the neutron and results in diffraction providing atomic and/or magnetic structural information, similar to X-ray diffraction with the difference that neutrons interact with the atomic nuclei or magnetic moment [21].

In an inelastic neutron scattering (INS) process, part of the energy of the neutron is transferred to the atom and a INS spectra is measured as a change of kinetic energy of a neutron upon collision with a sample. INS is used in the investigation condensed matter to study molecular motion as well as magnetic and crystal field excitations (phonons and magnons). If the energy of the scattered neutron is negligible compared to the incident energy, then quasielastic scattering occurs that can be used to study dynamical process such as diffusion [52].

Spallation sources produce high-flux neutron beams that have recently replaced the nuclear reactors as modern neutron sources, where the neutrons are produced

by nuclear fission. In a spallation source, a proton or electron high-energy beam (>100 MeV) hit a target of liquid mercury (or other metal).
The high energy proton beam hit the target atoms creating a large number of neutrons ($\sim$20 neutrons per proton) in a cascade process. First, some of this protons and neutron leave the target nucleus with energies up to the original energy of the colliding proton in a process that take around 10^{-22} s. The residual nucleus remains in a excited state that decays emitting isotropically neutrons, protons and α-particles with energies up to 10 MeV in a process that takes around 10^{-16} s.
After their generation, the highly energetic neutrons ($\sim$10MeV) are brought to usable energies by thermalization in a hydrogenous material (*e.g.* water [300 K $\sim$ 25 meV]) or liquid hydrogen [20 K $\sim$ 1.7 meV]) called moderator. The neutron beam is passed by a chopper monochromator and then guided to the experimental devices outside the neutron source shielding [53].

Neutron vibrational spectroscopy

Neutron inelastic scattering (INS) as a method of measuring the neutron vibrational spectrum gives information about the molecular structure, chemical bonding, and intermolecular interactions of a sample.
Since neutrons have a mass approximately equal to that of the hydrogen atom, an inelastic collision results in a significant transfer of momentum, as well as energy, to the molecule. The cross-section for hydrogen is 80 barns while that for virtually all other elements is less than 5 barns that makes it ten times more visible than any other atom. Therefore, the modes that involve significant hydrogen displacement will dominate the spectrum. The cross-section is strongly isotope dependent (*e.g.* deuterium cross-section is 5 barns). Consequently, isotopic substitution by D in the target material can be used to 'remove' H parts of the molecule from the spectrum.
Similar information can be obtained by optical vibrational spectroscopies such as infrared absorption or Raman, which are widely used examples that directly measures the energies of the molecular vibrational transitions. Raman spectroscopy

Table 2.2 Comparison between neutron (INS) and optical(Raman/Infrared) vibrational spectroscopy [54].

INS	Raman/Infrared
Measures dynamics of nuclei (direct)	Measures response of electrons (indirect)
No selection rules	Selection rules apply
Great sensitivity to H	Cannot always see H
High penetration (bulk probe)	Low penetration
Easy access to low energy range (librational and translational modes) applies	Low energy cutoff (on the order of 12 meV)
Easy to simulate/calculate	Difficult to simulate/calculate
Weighted by neutron scattering cross section	Weighted by change in polarizability or dipole moment
No energy deposition in sample	Heating and photochemistry

is an example of inelastic scattering that obtains a vibrational spectrum by measuring the energy difference (gain or loss) between the incident radiation and the small fraction of the radiation that is inelastically scattered [52, 55].
Neutron vibration spectra possess several advantages compared to other radiations (see Table 2.2). Firstly, whether a mode is infrared or Raman active (or is inactive in both) is determined by the symmetry of the molecule. In contrast, there are no selection rules for INS spectroscopy and as a result all modes are allowed with several strong bands that do not have counterparts in the infrared and Raman spectra.
Secondly, in INS spectra, the frequencies are determined by the normal modes of vibration, but the intensities are dependent only on the scattering cross-section and the amplitude of vibration, in contrast to optical spectroscopies, where the intensities are determined by changes in the electronic properties of the molecule (the dipole moment and the polarizability for infrared and Raman spectroscopy, respectively).

Vibrational neutron spectroscopy of solid and liquid hydrogen

This work uses INS as an ideal vibration spectroscopy to study the adsorption of hydrogen. The INS spectra of H_2 in solid and liquid state possesses a remarkable

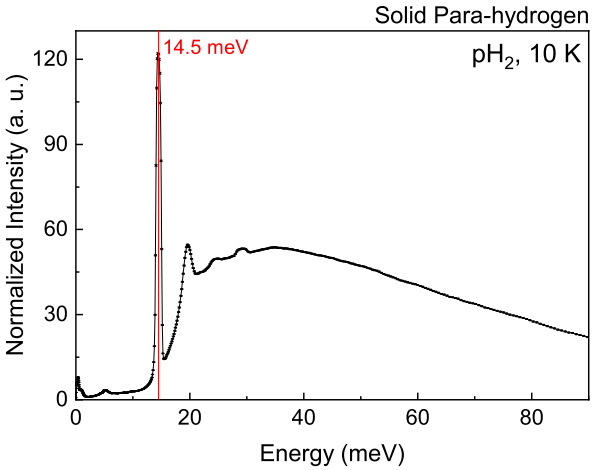

Figure 2.5 *INS spectrum of solid* pH_2 *at 5 K.* The INS spectrum shows a sharp peak at exactly 14.5 meV associated to the free-rotor transition of the hydrogen molecule.

difference; in solid-state, the hydrogen molecules behave as a free rotor with energy states associated with the rotational motion of a completely isolated molecule. Because hydrogen molecules in solid-state are all almost unperturbed by any interaction between the neighboring hydrogen molecules, they can show a rotational transition at 14.5 meV; as solid hydrogen is warmed the effects of the recoil become more marked.

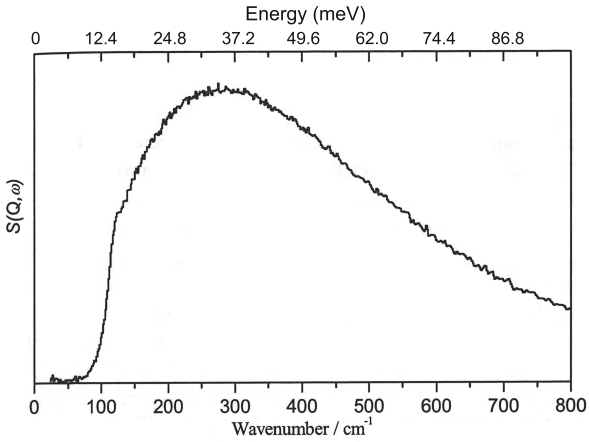

Figure 2.6 *INS spectrum of liquid hydrogen at 14.1 K.* The INS spectrum shows a broad maximum centered at 32 meV that is associated to translation recoil. Reproduced from [56].

Figure 2.5 shows an INS spectrum of solid para-hydrogen at 10 K. The broad peak centered at 34 meV is related to the translational recoil of the hydrogen molecule which has been investigated elsewhere [56]. The peak centered at 14.5 meV is directly related to a free-rotational transition J:1→0. Close to 20 meV a small peak also is visible that has been previously discussed as a product of the rotational transition displaced by the translational recoil with an energy given by E= 34 - 14.5 ≈ 20 meV [56].

Figure 2.6 shows the INS spectra of H_2 in liquid state. The sharp peak at 14.5 meV observed for solid disappears in liquid state and only a broad maximum centered at 32 meV is observed, which associated to transnational recoil.
The rotational transition is given by the symmetry of the total wavefunction which implies that para-hydrogen (proton spins anti-parallel) can only exist in even J states while ortho-hydrogen (proton spins parallel) only exists for odd J. In the absence of significant external interactions, the rotational energy levels of hydrogen are given by Equation 2.23; for which the lowest energy level transition between two states is J:1→0 (ortho → para), with an energy of 14.5 meV [57, 58].

$$E_J = B_J \cdot J(J+1) \tag{2.23}$$

where J is the rotational quantum number and the rotational constant B_J is given by

$$B_J = \frac{\hbar^2}{2I_{HH}} = 7.357\ meV \tag{2.24}$$

where I_{HH} is the moment of inertia of the solid hydrogen molecule given by $I_{HH} = \mu r_{HH}^2$, μ is the reduced mass, and $r_{HH} \approx 7.4$ Å is the proton-proton distance calculated by Silvera [59].
The rotational constant B_J =7.25 meV was experimentally obtained using the mean energy of rotational transition obtained for solid para-hydrogen (Fig. 2.5) and Equation 2.23. Using the rotational constant B_J and the reduced mass μ of the hydrogen molecule, the length of the hydrogen molecule was calculated to be 0.756 Å, which is close to the value reported by Silvera (0.74 Å) [59].

2.5 Kinetic quantum sieving

In 1995, Beenaker *et al.* [18] theoritically proposed a way to separate light gaseous isotopes using porous materials on the basis of kinetic quantum sieving (KQS). Such effect was further discussed by K. Johnson et al. [60, 61] and later

experimentally confirmed by K. Kaneko et al. [62] for carbon with pores in the subnanometer region.

KQS depends on the difference in zero point energy (ZPE) levels emerging from a different mass of the isotopic species when they are adsorbed by porous material with a pore size similar to the molecular kinetic diameter [20, 63, 64]. The kinetic diameter of a gas molecule expresses the likelihood that a molecule in a gas will collide to another molecule, and is defined as $d^2 = \frac{1}{\pi l n}$, where l is mean free path of a gas molecule and n is the number density of particles.

Beenaker's model of a quantum molecular sieve described a gas molecule in a cylindrical pore using a simple deep potential well. KQS is observed when the difference in the pore size, d, and molecule kinetic diameter, σ, is in the order of the de Broglie wavelenght of the gas molecule ($d - \sigma \approx \lambda_B$). For such pore dimension, the ZPE levels depend on the mass of the isotopic species given by

$$E_0 = \frac{2\gamma_0^2 \hbar^2}{(d-\sigma)^2 m} \tag{2.25}$$

where γ_0 is the zeros of the Bessel function.

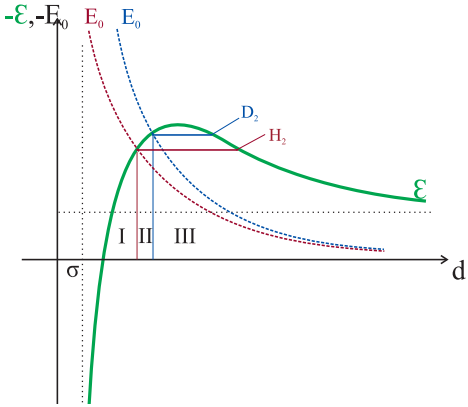

Figure 2.7 *Energy potential of a particle confined in a pore.* The particle is confined in a pore ($d - \sigma \approx \lambda$) with the zero-point energy levels depending on difference $d - \sigma$. The regions I, II and II are explained in text. Figure adapted from [18].

As a result, the ZPE can overcompensate the attraction of the walls resulting in a reduced transverse motion of molecules in the pore channel, and in an energy barrier for molecules entering the pores [18].

Consequently, the adsorption and diffusion in narrow pore channels of isotopes with the same kinetic diameter σ is mainly governed by the molecule mass. In particular for hydrogen isotopes (σ_{H_2/D_2} = 2.89 Å), the zero-point energy levels

of H_2 is half of the D_2 ($E_{0_{H_2}} = \frac{1}{2}E_{0_{D_2}}$), and it is responsible for the stronger adsorption and higher diffusion rate of deuterium. Figure 2.7 show a scheme of the ZPE differences between H_2 and D_2. For a pore diameter in the region I, for both molecules experience an energy barrier. The region II marks the optimal pore diameter where the ZPE of H_2 is higher, creating a barrier for H_2 and allowing the entering of D_2. The region III the pore diameter is large enough to allow both isotopes enter the pore.

According to kinetic theory, the molecular transport at low pressures in small pores is given by Molecular or Knudsen diffusion, which occurs when the length scale of a system is comparable to or smaller than the mean free path of the molecules involved. In this case, the diffusivity is inversely proportional to the molecule mass ($D \propto 1/\mathrm{m}$) and consequently the lighter particle has a higher diffusivity. In contrast, the zero-point energy difference between two particles of the same size but different with masses, described by the KQS effect, implicate a higher mobility the heavier particle (D_2), contrary to the kinetic theory.

Chapter 3

Experimental details

3.1 Low-pressure high-resolution adsorption experiments

Adsorption experiments with were collected for different gas adsorbates in a temperature range 20 - 300 K, using a fully-automated Sieverts' apparatus [65], *iQ*$_2$ *Autosorb* fabricated by *Quantachrome Instruments* (Fig. 3.2). The device is equiped with an ultra-low pressure transducer allowing the measurement of high-resolution isotherms at pressures as low as $1{\cdot}10^{-8}$ bar with an excellent temperature control.

The device is capable to measure adsorption isotherms and simultaneously record the pressure equilibration in time per pressure point with a maximum time resolution of 0.5 sec.

Figure 3.1 shows a schematic diagram; the inlet is connected to four different gas lines (H_2, D_2, Ar and N_2), a valve selects the gas and loads it into the manifold. The manifold has a precisely calibrated volume used to dose specified amounts of gas in a pressure range from $1{\cdot}10^{-8}$ to 1 bar, measured by three different pressure transducers ($1{\cdot}10^{-8}$-$1{\cdot}10^{-4}$, $1{\cdot}10^{-4}$-0.1, 0.1-1 bar). A glass or

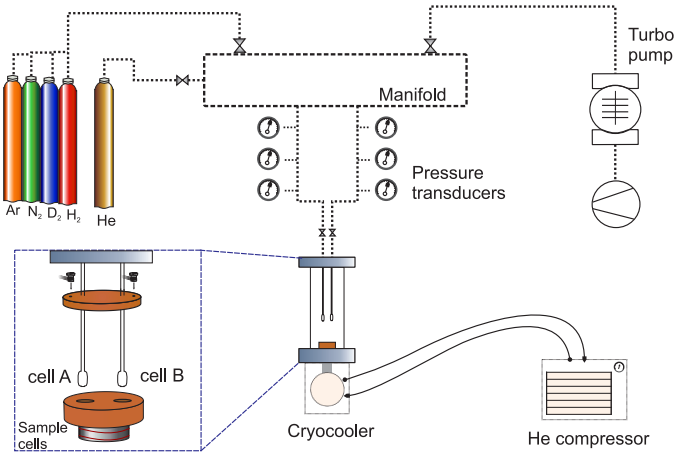

Figure 3.1 iQ$_2$ Autosorb *adsorption device diagram.* The *iQ$_2$ Autosorb* is a device based on the Sieverts' apparatus. The description of is presented in the main text.

copper sample cell is coupled to a cryocooler based on the *Gifford-McMahon* cycle, described elsewhere [66], to control the sample temperature between 19.5 and 300 K with a temperature stability of $\pm$ 0.05 K. A high-vacuum system is connected to the manifold to evacuate the sample or reduce the pressure. The device uses a volumetric measurement to determine the amount of adsorbed gas (see Chapter 2, [26]). A calibration curve is automatically subtracted from the data in order to subtract the non-adsorbed gas in the sample cell. Because of the accurate pressure measurement and temperature control, it is possible to utilize amounts of material as low as $\sim$10 mg with still a reasonable error or measure samples with a surface area of a few square meters per gram. The device is controlled by the software *ASiQwin v3.0.1* and the data analysis was made with the software *Originlab 2018*.

Figure 3.2 *Image of the* iQ$_2$ Autosorb *adsorption device.* The two independent stations give the capability to measure two samples at the same time using the same conditions; (a) two independent sample cells; (b) cryocooler isolation; (c) device front photo.

iQ$_2$ Autosorb calibration

All experiments were carried out using the automated operation mode NOVA (NO Void Analysis) based on a separate calibration of the sample cell prior to the analysis [26]. The gas dosing n_{dose} is done by a precisely calibrated volume (manifold); while the calibration curve n_{cal} is an individual (gas volume-vs-pressure) analysis of an empty sample cell for a given gas and temperature. Figure 3.4 shows as an example a hydrogen calibration curve of an empty cell at 20.37 K, where the volume of the gas in the empty cell is plotted versus the absolute pressure. The adsorbed amount n_{ads} is calculated for each data point of the isotherm by subtracting the calibration from the dosed gas amount (Eq. 3.1); given in volume units *cc* [STP - standard pressure temperature].

$$n_{ads} = n_{dose} - n_{cal} \tag{3.1}$$

Because the sample volume is nearly zero for the masses typically used (∼10 mg), it can be negleted. For larger amounts of material, the differences in the volume can be automatically corrected from the calibration accounting for the non-linearity of the adsorbate [67] and the sample volume, measured by an independent He expansion test [65].

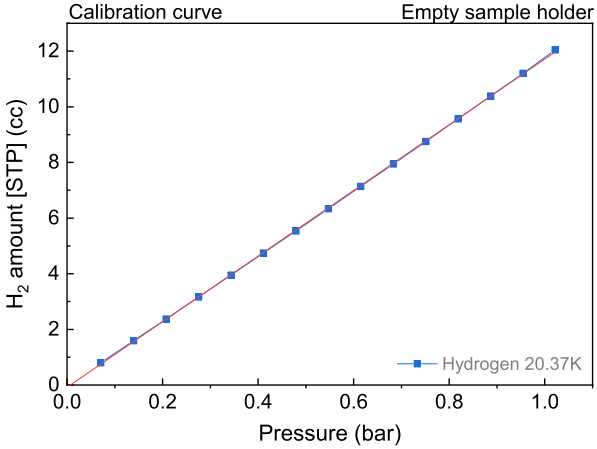

Figure 3.3 *Hydrogen calibration curve for the Cell A at 20.37 K.* The dosed volume shows a linear relation with the gas pressure.

The error associated to temperature fluctuations was calculated using a second empty cell experiment (increasing [0 to 1 bar]/ decreasing [1 to 0 bar] pressure). The calibration curve is automatically subtracted from the second empty cell experiment. Ideally, this subtraction yields to a zero absolute uptake in units of volume [cc] for every pressure point (0 - 1 bar) because the second experiment is done under the same conditions as the calibration. The small variations from the "ideal" zero amount (Fig. 3.4) are related to the thermal fluctuations in the sample cell and constitute the major source of experimental error.
The deviation of the amount of gas from the "ideal" zero is plotted as function of pressure to calculate the error (Fig. 3.4); a linear model is used in such a way

that a line, that represents the maximum deviation of the points, is always above the absolute value of the all data points.
The linear model represent the maximum dispersion (positive or negative) of the gas amount at a given pressure in units [±cc]. The maximum dispersion is divided by the sample mass to calculate the error of the adsorbed gas on the sample per unit of mass [±cc/g]. This procedure only accounts for the error related to temperature fluctuations and gives only an approximation of the total error of the measurement.

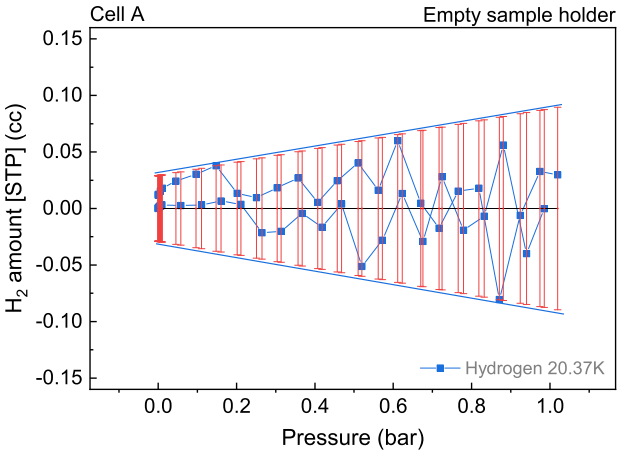

Figure 3.4 *Second empty cell test for Cell A using H_2 at 20.37 K.* The calibration volume is automatically substrated from the experiment and a total volume adsorbed is close to zero. The dispersion of the data points from the zero are related to small temperature fluctuations.

The temperature of condensation T_{CellA} of the sample cell (*Cell A*) is measured by two different thermocouples located in the cryocooler cooper block. Additionally, the vapor pressure[1] P_0 can be monitored by an independent pressure transducer.

[1] The vapor pressure or equilibrium vapor pressure is defined as the pressure exerted by a vapor in thermodynamic equilibrium with its condensed phases (liquid or solid).

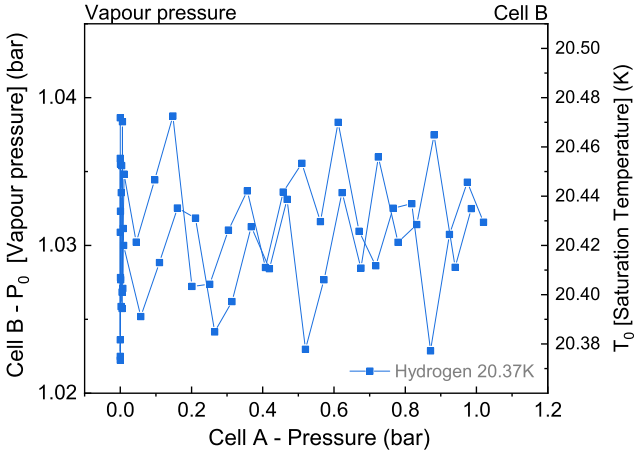

Figure 3.5 *Hydrogen vapor pressure as function of the pressure points in the empty cell test for the Cell B at 20.37 K.* The saturation temperature was calculated from the vapor pressure using the state equation by NIST [28–30].

The machine uses an vapor pressure station connected to a second cell (*Cell B*) that is filled with a large amount of gas. Both cells (*Cell A and B*) are in close contact with the cooper block and it is assume that both are in thermal equilibrium ($T_{CellA} = T_{CellB}$).

A large amount of the adsorbate gas is introduced into the second cell (*Cell B*) which condensates after some minutes. The liquid phase inside the second cell (*Cell B*) ($T \approx T_0$) is in equilibrium with the gas ($P \approx P_0$), and therefore the pressure reading is the pressure of condensation (vapor pressure) of the adsorbate at the temperature of both cells ($T_{CellA} = T_{CellB}$). This allows an independent measurement of the temperature inside the cells comparing the vapor pressure to the respective temperature of condensation. The vapor pressure is related to the temperature of condensation by the state equation of the respective gas $P_0 = P(V, T_0)$, obtained from the NIST web page [28–30].

The vapor pressure P_0 was recorded while an empty cell experiment was conducted in cell A. Figure 3.5 (left axis) shows an example using hydrogen (20.37 K) of the vapor pressure P_0 in second cell (*Cell B*) as function of the sample cell pressure (*Cell A*). The vapor pressure in the second cell (*Cell B*) has small variations (from 1 bar) during the empty cell experiment in the sample cell (*Cell A*).
Figure 3.5 (right axis) shows the corresponding temperature of condensation T_0 of hydrogen given by the hydrogen state equation, for a target temperature of 20.37 K measured by the thermocouples. This example shows that there is a small difference in the reading between the thermocouples and the pressure of condensation that correspond to an average temperature of 20.42 inside *Cell B*. The dispersion in the temperature of saturation is related to the error in the temperature control which is determined to be ± 0.05 K, as the manufactured specified.

3.2 Pressure-composition-temperature (PCT) adsorption experiments

An automated Sieverts' apparatus *PCTPro-2000* equipped with a so-called micro-doser, fabricated by *Setaram-HyEnergy*, was used to accurately measure high-pressure hydrogen isotherms for small amounts of sample ($\sim$100 mg) with a maximum pressure of 25 bar. A schematic illustration of the device is shown in Figure 3.6. H_2 is dosed by a manifold with a volume of 0.51 ml using the micro-doser; a variable valve in the inlet line regulates the gas pressure; the manifold is connected to an external high-vacuum system to reduce the pressure and evacuate the sample.
An in-house made cooling-heating device is used to regulated the temperature in a range of 77 to 130 K; the temperatures 77 and 87 K are achieved submerging the sample holder in a dewar filled with liquid N_2 or Ar, respectively (Fig. 3.6 *Dewar*). For temperatures above 87 K, the sample holder is enclosed by a

copper block (orange) with a cooling finger submerged in liquid nitrogen (Fig. 3.6 *Heater*). The liquid nitrogen level is controlled within ± 0.2 cm height by an automatic liquid N_2 refilling system. The copper block includes a K-type thermocouple and a heater connected to a Proportional-Integral-Derivative (PID) controller that is capable to maintain a constant temperature within ± 1 K over the temperature range 87 - 130 K.

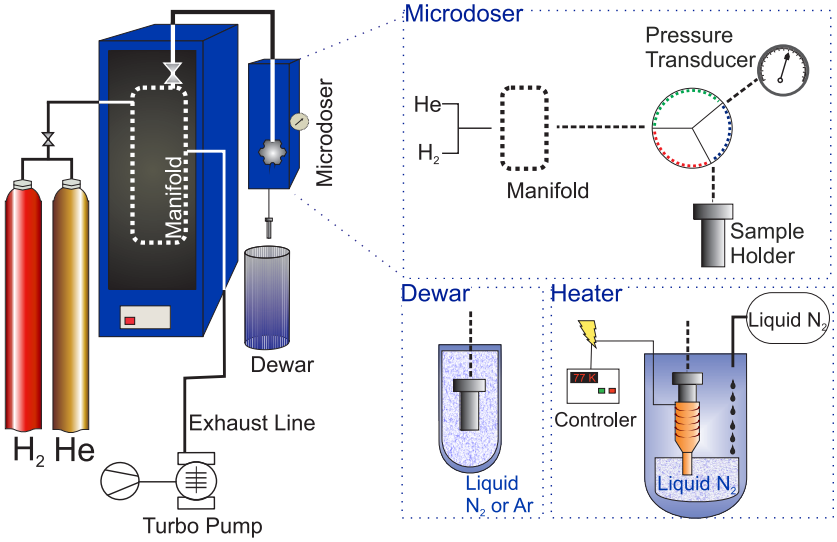

Figure 3.6 *Pressure composition temperature* PCTPro-2000 *device diagram.* A manifold is directly connected to a micro-doser designated to dose small amounts of H_2. *Dewar*: Dipping method with a cryostat for cooling at liquid nitrogen (77 K) and liquid argon (87 K) temperature. *Heater*: Cooling system for temperatures above 87 K where the sample container is enclosed by a copper block (orange) and partially sank in the liquid nitrogen. The liquid nitrogen level is constantly controlled by automatic liquid N_2 refilling system.

Volume calibration

The temperature gradient between sample and manifold is corrected by hydrogen expansion, using a non-adsorbing material (sea sand), measured at different tem-

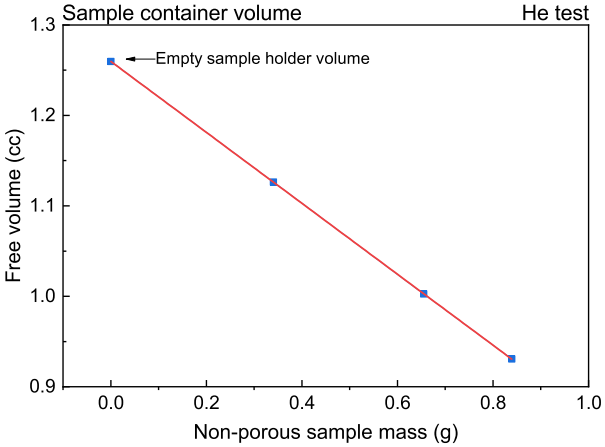

Figure 3.7 *Non porous reference volume measured by He test.* Different amounts of see sand were used and the volume was measured for each mass by a He test.

peratures and pressure for various volumes of material. This yields the amount of non-adsorbed gas considering all temperatures and temperature gradients. The measurements of an adsorbing material are corrected with these values of non-adsorbing material of the same volume *i. e.* the calibration accounts for the H_2 amount present in the "free volume"[2] in the sample holder, with the prerequisite of knowing the skeleton volume V_{ske} of a given sample. The empty sample holder volume V_{holder} is calibrated by several tests with helium (He test[3]) yielded a volume of 1.27 ± 0.02 ml. The volume of the non-adsorbing material is obtained by He test varying the amount of *see sand*. Figure 3.7 show the He test results where the volume of the sample container V_{free} is presented as a function of the *sea sand* mass.

[2]The free volume is accessible volume to helium, and accounts for the free space in the sample holder and the pore volume of the sample

[3]The helium expansion test consists in the measure of the pressure change when a known volume of helium given by manifold volume is let to expand into the sample container. This method make the assumption that the He has a no interaction with any surface at room temperature, such assumption can be unrealistic, especially for microporous materials.

For each sample investigated, the "free volume" in the sample holder V_{free} is measured ten times by He test. The skeleton volume of the sample V_{ske} is obtained subtracting the free volume V_{free} from the sample holder volume V_{holder}

$$V_{ske} = V_{holder} - V_{free} \tag{3.2}$$

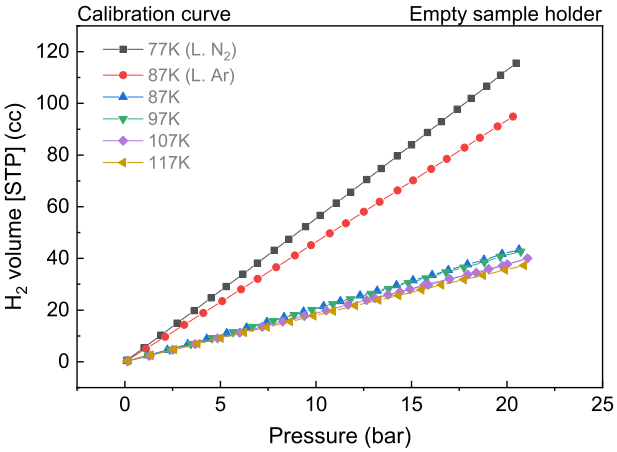

Figure 3.8 *PCT calibration curve for the temperatures 77, 87, 97, 107 and 117 K.* The calibration curve has a linear relation with the pressure as the non-linear effects related to the H_2 compressibility are not noticeable in this pressure range.

Figure 3.8 shows an example of H_2 capacity for the first calibration volume used (empty sample cell, mass(sea sand) = 0), varying the temperature between 77 - 117 K. A linear relation is observed between the amount of hydrogen and the pressure. The slope of the calibration curves (Fig. 3.8) is the amount the non-adsorbed hydrogen contained in the free volume of sample holder V_{free} per unit of pressure. Figure 3.9 shows a plot of the slopes as function of *see sand* mass, for every temperature used. The x-axis below shows the *see sand* which is correlated to the free volume V_{free} (upper x-axis) given by Figure 3.7.

Using a linear interpolation, the amount of H_2 non-adsorbed can be calculated as a function of the sample skeleton volume V_{ske}. The excess hydrogen adsorbed amount n_σ is then given by

$$n_\sigma(P,T) = n_{dosed}(P,T) - n_{free}(P,T) \tag{3.3}$$

where $n_{dosed}(P,T)$ is the dosed hydrogen that counts for total amount of hydrogen present in the sample container (adsorbed on the sample and non-adsorbed), $n_{free}(P,T)$ is the non-adsorbed gas for a given V_{ske}, P and T.

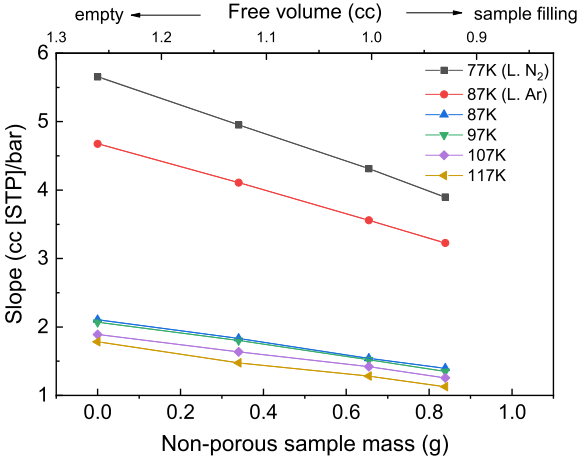

Figure 3.9 *Calibration slopes as function of free volume for different temperatures.* The calibration slope is calculated using the free volume obtained from the He expansion test for each sample.

Packing volume determination

The packing volume of the sample was determined by geometrically measuring the fill height of the sample cell using a glass rod with exactly the same diameter as the inner diameter of the sample cell. After the sample filling the glass rod

is introduced and the volume of the sample is calculated based on the depth of penetration of the glass rod. After removing the glass rod the weight is re-measure to check any loss of sample material due to the measurement. The packing density was determined with the packing volume and dry mass of the sample [68] .

3.3 High-pressure gravimetric adsorption experiments

High-pressure adsorption experiments were collected using a *XEMIS* device fabricated by *Hiden Isochema*. The *XEMIS* is a gravimetric device which uses a microbalance to measure the change in weight in a sample controlling the pressure from 0 to 200 bar and temperature between 77 and 800 K. The pressure is measured by three different pressure transducers with the ranges 0.001-1 $\pm$0.0005, 0-20 $\pm$0.01 and 0 to 200 $\pm$0.1 bar. The pressure control operates using two needle valves driven by stepper motors. One valve is connected to the inlet line and the second is connected to an exhaust line with a high-vacuum system. By continuously closing and opening the inlet and exhaust valves the machine can ramp and continuously control the pressure inside the microbalance chamber.

Figure 3.10 shows a schematic representation of the *XEMIS* device. A microbalance is inside of a chamber is connected to two detachable reactors. Two thin tungsten wires hang from both arms of the microbalance and holding the sample and counterweight. A gas inlet tube connects the pressure system to the microbalance chamber and reactors. The sample is usually in a thin grid sample holder made of steel and the counterweight is a steel wire with a measured density of 7.886 g/cc. The temperature in the sample can be controlled externally submerging the reactor in a Dewar with liquid N_2 or Ar, or by a cryofurnace. The cryofurnance is a heating system that incorporates a liquid N_2 heat exchanger to enable sub-ambient temperature control by a flow of a cryogen and an internal

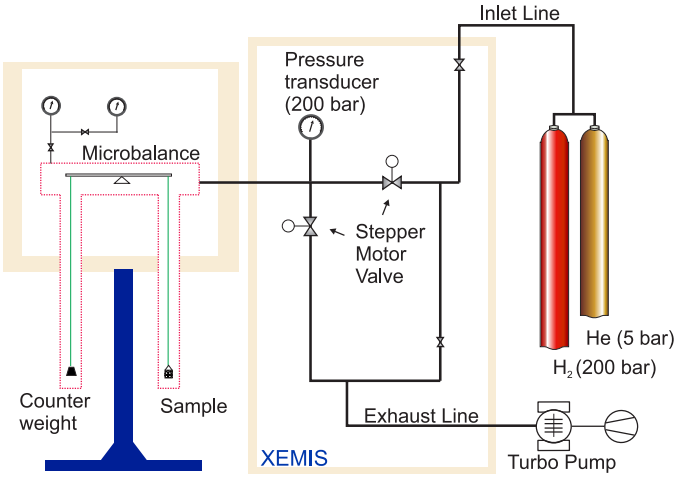

Figure 3.10 *XEMIS device diagram.* The XEMIS is based in a gravimetric measurement using a microbalance and three different pressure transducers. Two valves electronically controlled are connected to the inlet and exhaust lines to continuously control the pressure in the microbalance chamber.

resistance which is connected to PID unit to control the temperature with an error of ± 0.1 K.

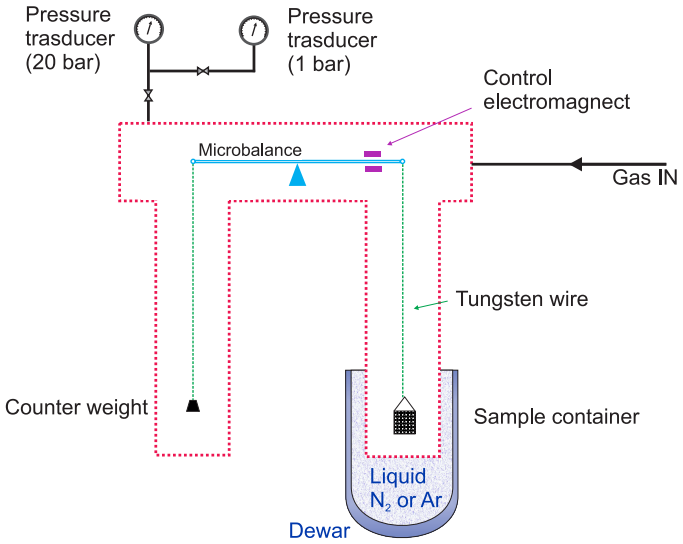

Figure 3.11 *Microbalance diagram of the XEMIS machine.* The microbalance uses a electromagnet connected to a control unit to equilibrate the balance, the mass of the sample is proportional to the current applied to the electromagnet.

The balance is keep in equilibrium by two electromagnets, a control loop adjust a electrical current in the electromagnets (Fig. 3.11) that counteract the weight of the sample. The microbalance can measure the masses with an error of ± 0.1 μg by measuring the electrical current circulating in the electromagnets, which is proportional to the sample mass. The pressure transducers are separated from the chamber by two different valves that are open at different pressure, 0 - 1 and 1 - 20 bar.

Buoyancy

Figure 3.12 shows a diagram of the forces in the action in the sample; the gravitational force F_g or weight is proportional to the sample mass and pulls down the sample with a magnitude $F_g = mg$ where g is the gravitational acceleration and m is the mass. A buoyancy force F_b pulls the sample up and it is proportional to the skeleton volume of the sample V_{ske} and to the density of the surrounding fluid ρ, and it is equivalent to the weight of the fluid that would otherwise occupy the volume of the sample $F_b = -V_{ske}\rho g$. The adsorption of a fluid on the sample surface modifies the overall mass of the sample which increases the weight $\delta m_{ads} \cdot g$. A higher gas pressure increases the density of the fluid where the sample is immersed, as the density increases the buoyancy force is also higher. The Equation 3.4 gives the sum of all forces that the balance records as the total weight: the sample weight $m_{sample} \cdot g$, the buoyancy $V_{ske} \cdot \rho \cdot g$, and the weight change related to the gas adsorption $\delta \cdot m_{ads} \cdot g$.

$$\Sigma F = m_{sample} \cdot g + \delta m_{ads} \cdot g - V_{ske} \cdot \rho \cdot g \tag{3.4}$$

The correction of the buoyancy force is made using an individual He test to measure the skeleton volume of each sample. The He test is made at room temperature under the assumption that He does not interact with the surface of the sample at this temperature. This means that any amount of He adsorbed on the sample surface will lead to some error in the subsequent assessment of adsorbed gas. The He test records the negative change in weight ΣF as function of the He pressure (Sample bouyancy). Using the state equation for He [30] and measured temperature, the He density is calculated. Figure 3.13 shows as an example a typical He test result for the sample MOF-205.
The skeleton volume V_{ske} of the sample corresponds to the negative slope of a linear fitting applied to the He plot (Sample buoyancy vs He density) given by the Equation 3.5, which assumes no He adsorption.

$$S_B = \frac{\Sigma F}{g} = m_{sample} - V_{ske} \cdot \rho_{He} \tag{3.5}$$

where S_B is the apparent mass recorded by the balance or sample buoyancy, ΣF is the the sum of the forces acting on the balance, ρ_{He} is the He density and m_{sample} is the y-intercept and correspond to the sample mass. The skeleton volume V_{ske} correspond to the slope of a linear relation between the S_B and ρ. The adsorbate gas equation, in our case H_2 obtained from NIST web page [30], is used to calculate the density of the gas adsorbate for a given pressure and temperature. This density is used together with the calculated V_{ske} (Eq. 3.4) to correct the buoyancy of the sample.

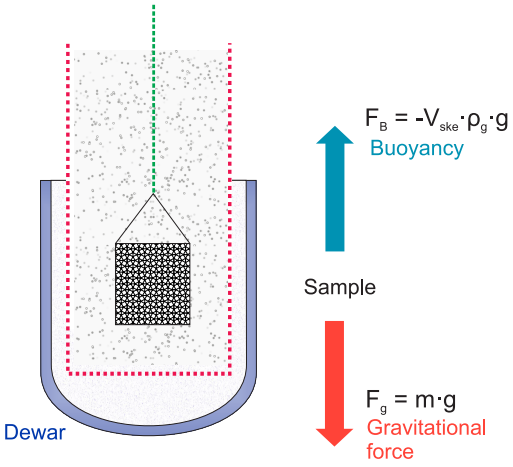

Figure 3.12 *Force diagram of the sample in the XEMIS microbalance.* The sample weight measurement must be corrected for the buoyancy of the sample volume in a fluid.

3.4 Neutron vibrational spectroscopy

Inelastic neutron scattering experiments were conducted using the vibrational spectroscopy endstation VISION at the Spallation Neutron Source (SNS), Oak Ridge National Laboratory (Fig. 3.15). VISION is a neutron indirect geometry instrument, which bases on the calculation of energy change of each neutron

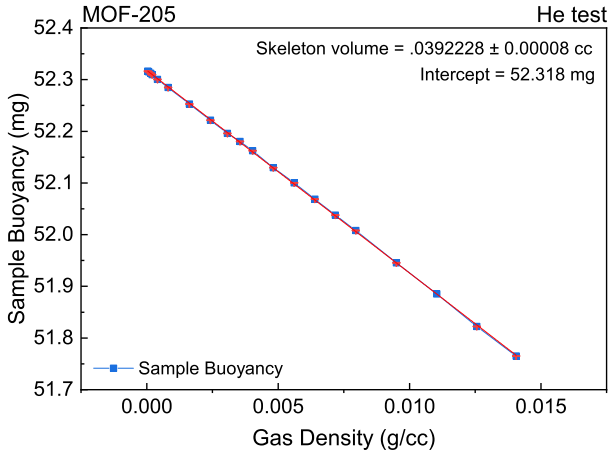

Figure 3.13 *MOF-205 skeleton volume by He test.* MOF-205 He test calibration as an example to obtain the skeleton volume to correct the buoyancy of the sample, where the skeleton volume of the sample is the slope of the linear fitting to the bouyency vs the gas density.

on measurement of the time-of-flight. It is optimized to characterize molecular vibrations in a wide energy range (-2 - 1000 meV) and with an energy resolution $< 1.5\%\ \Delta E/E$. This instrument offers enhanced performance by coupling a white beam of incident neutrons and selects neutrons (after scattering by the sample) with very well defined final energy ($\sim$3.5 meV) using two banks of seven analyzer modules. They are equipped with analyzer arrays (1 cm^2) made of pyrolytic graphite arranged on a curved surface that focus neutrons on a series of small ^{3}He detectors (Fig. 3.14).
This configuration, together with the high intensity flux of neutron from SNS, allows VISION to collect neutron data within minutes for the case of experiments with H_2 and leads to an improved signal-to-noise ratio [69].

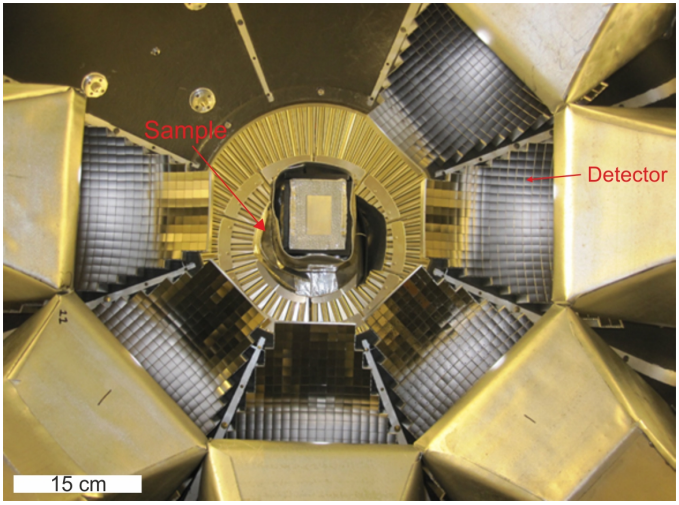

Figure 3.14 *Photography of the neutron detectors of VISION taken from the neutrom beam axis.* Courtesy of Oak Ridge National Laboratory, U.S. Dept. of Energy [69].

Sample environment VISION working principle is depicted in Figure 3.15, the neutron beam guided to the sample located in the central part of the spectro-

menter. Two banks of detectors (Fig. 3.14) are located in front of the sample and behind the sample. The sample stage is equipped with a cryocooler fabricated by *Janis Research Company* operating between 5 and 500 K. The sample is introduced to the sample stage using a sample holder sealed with indium wire and attached to the end of a stick inserted in the top of the cryocooler. The sample holder is connected with a capillary line to a gas dosing device to control of the sample atmosphere in a pressure range of 0-100 bar.

Ultrahigh purity hydrogen was used for all measurements. Normal hydrogen was obtained directly from the gas cylinder. Para-hydrogen was prepared by liquefying normal hydrogen over Oxisorb (CrO nanoparticles deposited over silica) at 17 K and bleeding the vapor off this system at 22 K.

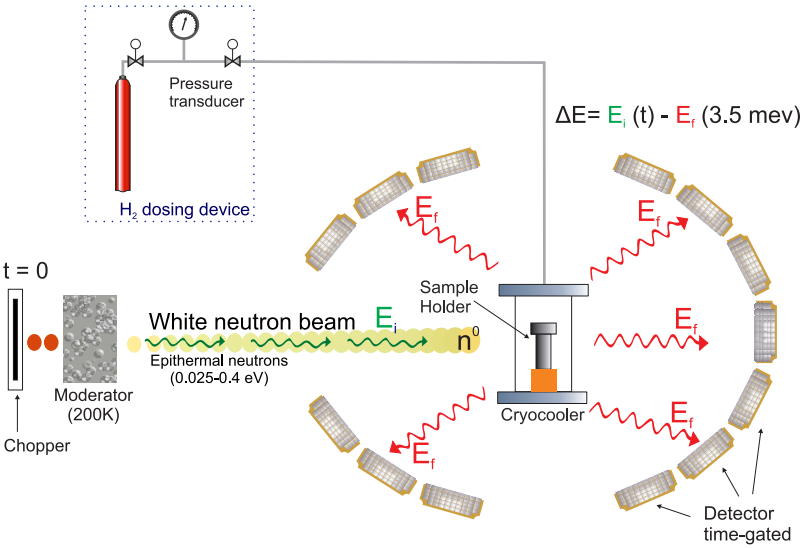

Figure 3.15 *Inelastic neutron scattering: VISION spectrometer.* The energy sensitive detectors measures the change in energy of the neutrons scattered by sample. The sample is situated in front of the incoming neutron beam in a aluminum sample holder. The sample atmosphere can be controlled by an independent manually operated Sieverts' apparatus.

INS spectra of the sample holder and sample (background spectrum) were collected at different temperatures, with a previous activation of the sample for several hours at high temperature and high-vacuum. The background spectra were subtracted from all experiments using the software *Mandid v3.6.0*.

Chapter 4

High-density adsorbed hydrogen

The density or H_2-H_2 intermolecular distance of an adsorbed hydrogen layer on the surface of an adsorbent determines directly the storage properties of porous materials. Light gases such as H_2 (and He) possess low molecular weight and low boiling point that result in unique properties such as high-compressibility of the solid phase [17, 62]. He adsorption has been extensively studied due to its quantum properties at low-temperature such as superfluidity [14, 70, 71]. On the other hand, for H_2 adsorption at its boiling temperature (20.37 K) only a few reports exits, whereas most of the current research is focused on the adsorption at 77 K. The first reports of adsorbed hydrogen (and helium) at boiling temperature [4, 14], respectively, show first layer capacities (monolayer) as high as two times the capacity obtained for other gases Ar or N_2 [4, 6].

So far, two main explanations have been proposed for the high monolayer capacity of H_2; the first suggests the simultaneous formation of two adsorbed layers or a bilayer that would imply that the monolayer capacity counts exactly two layers of adsorbed molecules. Another possible explanation is the formation

of a monolayer with a high-density. However, there is still the need for the experimental proof of either of these hypotheses.

In this chapter, the adsorption of H_2 on the surface of porous materials at temperatures close the boiling point ($\sim$20 K) is thoroughly studied for materials with different pore topologies and different surface chemistry; silica and carbon surfaces, which possess large pore sizes (>10 nm) that makes them relatively flat surfaces compared to the size of the hydrogen molecules (2.89 Å); and metal-organic frameworks (MOFs), composed by metal-oxide clusters connected by organic linkers that create a discontinuous surface (fragmented surface).
The density of the first layer of adsorbed hydrogen is studied by comparing high-resolution cryadsorption experiments for four different gases (Ar, N_2, H_2 and D_2) at their condensation temperature, respectively. Additionally, *in situ* inelastic neutron scattering experiments were used to follow the rotational transition of H_2 molecule for different dosings to study the formation of the first adsorbed layer.

4.1 Adsorption on flat surfaces

The first observation of a high monolayer capacity for light adsorbed gases (i.e. helium or hydrogen) was made in 1949 by Schaeffer *et al.* [13] who reported an abnormally high helium monolayer capacity at 4K, on carbon with pores 2.9 and 1.9 Å. Shortly after, Meyer [72] reported similar observations for He adsorbed on a homogenous surface of a gold foil. In 1956, Steele [15] proposed an explanation for the high He monolayer capacities, introducing a phenomenological model using the concept of a bilayer to explain the observed high capacities. Pace and Siebert [4] reported in a short letter the large discrepancy of the surface area of non-porous graphitized carbon determined by nitrogen (77 K) and hydrogen (20 K) adsorption experiments; suggesting an inter-molecular distance between hydrogen molecules of 2.95 Å that implies a high-density layer of H_2.

Table 4.1 Reported values of the monolayer capacity of H_2 adsorbed at low-temperature compared to N_2 or Ar monolayer values.

Author	Sample (material)	BET normal gas (N_2 [77K])		BET light gas (H_2 or D_2)		Ratio
		Monolayer capacity (mmol/g)	Specific surface area[†] (m^2/g)	Monolayer Capacity (mmol/g)	BET area[†] (m^2/g)	Monolayer ratio[◇] $(n_m(H_2)/n_m(N_2,Ar))$
Pace and Siebert (1959) [4]	Graphon (graphitized carbon)	0.9 [‡]	85.9	2.0 [‡] 2.2 [‡,*]	169 174[*]	2.2 2.4[*]
Huber and Huber (1990) [6, 73]	Vycor glass (silica)	1.4	136	2.6	–	1.7
Edler *et al.* (1997) [11]	MCM-41 (silica)	10.0	980	15.8	–	1.6
Tanaka *et al.* (2004) [17]	SWCH (carbon nanohorns)	9.6	938	15.7	1353	1.6
Prisk et al. (2014) [74]	MCM-41 (silica)	10.0	979	15.7	–	1.6
This work	KIT-6 (mesoporous silica)	4.2[§]	359[§]	8.4 8.6[*]	719 664[*]	2.0 2.0[*]

[†]Surface areas estimated using the cross-sectional areas, which were calculated from the respective bulk liquid density and hexagonal close-packing N_2 (16.2 Å^2), Ar (14.2 Å^2), H_2 (14.2 Å^2) and D_2 (12.9 Å^2); [‡]Calculated based on the reported surface areas by Pace and Siebert [4]; [§]Values obtained using Ar at 87.3 K; [*]Values obtained using D_2 at 23 K; [◇]Calculated for this work under the assumption that both molecules see the same surface area, the monolayer capacity ratio indicates how many more molecules (H_2 or D_2) cover the surface compared to Ar or N_2.

Table 4.1 shows the reported values of the monolayer capacity of H_2 adsorbed at low-temperature compared to N_2 or Ar monolayer values. The reported values of H_2 are compared to He in Appendix A (Table A.1). The ratio between monolayer capacities of the light gases (H_2, D_2 or He) and N_2 or Ar was calculated for all reported values. With the experimental verified assumption that the light gases see the same surface area that N_2 or Ar, the monolayer ratio indicates that a light gas (H_2, D_2 or He) can cover the same surface with at least 1.5 times more molecules/atoms than N_2 or Ar.

Several samples of silica and carbon were used to study H_2 adsorption, with a porosity mainly composed by pores with diameters of a few nanometers (mesopores $2 < d < 20$ nm) or larger (macroporous $d > 20$ nm). The dimensions of the pores are two orders of magnitude higher compared to the kinetic diameter of H_2 (2.89 Å), which makes the surface curvature sufficiently large, *i.e.* quasi flat surface (Fig. 4.3).

Mesoporous silica The mesoporous silica KIT-6 was chosen as model material. This system possesses a well-defined pore size of 10 nm and no microporosity which makes it an ideal material to apply the BET method [75] (see Chapter 2). Furthermore, the KIT-6 structure [77] has been extensively characterized showing a homogeneous and stable mesoporous structure that can be synthesized in large quantities [78, 79].

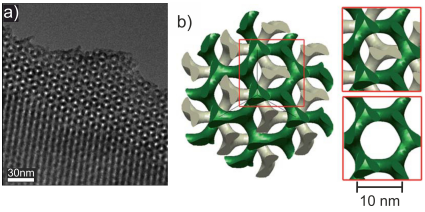

Figure 4.1 *KIT-6 mesoporous silica structure.* KIT-6 consists of two sets of interpenetrating mesoporous channels. (a) Reproduced with permission of John Wiley and Sons, from Vinu *et al.*[75], Copyright 2008; (b) Republished with permission of Royal Society of Chemistry, from Almar *et al.* [76], Copyright 2013; permission conveyed through Copyright Clearance Center, Inc.

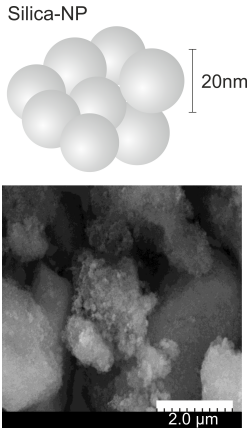

Figure 4.2 *Silica-NP.* The non-porous silica nanoparticles are nearly spherical with a uniform diameter close to 20 nm (electron microscopy). SEM micrograph shows that the particles are agglomerated into large units. SEM image by A. Ramirez-Cuesta group, ORNL.

Porous and non-porous silica The gas adsorption can be strongly altered by the morphology (pore shape and size) [41]. Two samples of silica with different porosities were examined: i) Non-porous silica nanoparticles (Silica-NP) with a fairly uniform diameter (of the order of 20 nm), which provide a relatively large specific surface area with constant curvature, and therefore, avoid any confinement effects. ii) Porous silica nanoparticles (Silica-P) with an inner porosity composed of micro and mesopores. Both silica nanoparticles have been synthesized with a variation of the method proposed by Stöber [80], in the group of Anibal (Timmy) J. Ramirez-Cuesta at Oak Ridge National Laboratory.

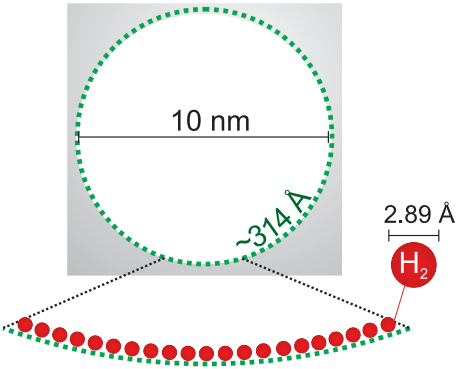

Figure 4.3 *Pore diameter comparison to the H_2 kinetic diameter.* The surface of a pore with a diameter of 10 nm is relatively flat compared to the kinetic diameter of H_2 (2.89 Å). The pore diameter correspond to a circumference of 314 Å where ∼100 molecules can be placed.

Porous carbon Several carbon porous samples were studied under similar conditions as silica. The carbons typically show much simpler surface chemistry compared to oxides and can be synthesized with morphologies similar to porous silica [82]. Three carbon samples with different morphologies were studied: i) The graphitized carbon Carbopack-B, that has the advantage to possess a homogeneous surface without the presence of any functional groups; unlike silica that usually possesses hydroxyl groups on the surface. ii) The mesoporous carbon CMK-3 was chosen as a comparison to the mesoporous silica KIT-6. This structure is synthesized using the silica SBA-15 as template [81]. However, previous reports showed small amounts of additional microporosity [83, 84]. iii) The macroporous carbon SRB-8F, due to its large pore size (>50nm), provides a model surface without confinement effects and a reasonably large specific surface area.

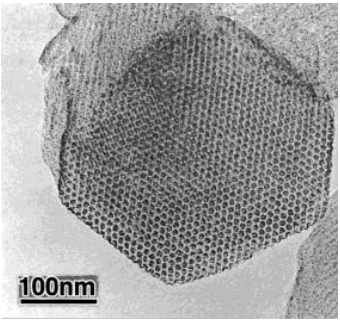

Figure 4.4 *CMK-3 TEM image.* The mesoporous carbon structure of CMK-3 is observed. Reprinted (adapted) with permission from S. Jun *et al.* [81]. Copyright 2000 American Chemical Society.

4.1.1 Adsorption experiments and BET analysis

Mesoporous silica KIT-6

The adsorption properties of the silica KIT-6 were studied using high-resolution cryoadsorption experiments for four different gas probes (H_2, D_2, N_2 and Ar) at their condensation temperature, respectively. Figure 4.5 shows the KIT-6 adsorption isotherms as a function of the relative pressure P/P_0 where P_0 is the pressure of condensation (1 bar). The shape of all isotherms can be classified by a type IV isotherm (see Chapter 2, Fig. 2.2), which is characteristic for the presence of mesopores with diameter in the range 2 - 20 nm [36].
The steep increase at low relative pressures ($P/P_0 < 0.1$) characterizes typically the monolayer formation of adsorbed molecules. At low-pressure ($P/P_0 < 0.6$),

the isotherms of H_2 and D_2 show two times higher uptake close to ∼9 mmol/g compared to Ar and N_2 that show adsorbed amounts close to ∼4 mmol/g. As a result, the monolayer capacities for H_2 and D_2 are approximately twice as high compared to Ar and N_2 isotherms. These are marked in Figure 4.5 by the respective B-points which are defined as the beginning of the middle, nearly linear, region of an adsorption isotherm indicating the monolayer completion [26, 36, 85]. In the pressure range $0.1 < P/P_0 < 0.7$ (Fig. 4.5), the isotherms grow linearly with pressure which corresponds to the formation of subsequent layers (multilayers) on top of the first (monolayer). For all gases, a hysteresis loop is formed between relative pressures 0.7 and 0.9, which is typically associated with capillary condensation in cylindrical-like pore channels. Close to the condensation pressure $P/P_0 \lesssim 1$, the pores are completely filled with a bulk liquid (see Chapter 2).

Figure 4.6a shows two different KIT-6 hydrogen adsorption isotherms collected at 20.37 K with a different number of points and different equilibration times (3 and 60 min). Both isotherms show an identical uptake, which indicates an adequate thermal and sorption equilibrium at each isotherm point.

Figure 4.6b shows a comparison of the KIT-6 hydrogen adsorption isotherms collected using different sample masses. There is no difference in the adsorbed amount at low relative pressures ($P/P_0 < 0.1$) where typically the monolayer completion (B-point) takes place, and only a small variation is observed at high relative pressures ($P/P_0 > 0.9$), related to uncertainty of the measurement (see Chapter 3).

The KIT-6 isotherms were analyzed using the BET method (see Chapter 2). The monolayer capacity, specific surface area, and pore volume were calculated from the isotherms of the four gases (summarized at the end of the chapter in Table 4.2). The BET analysis on the KIT-6 argon isotherm (Fig.4.7a) yields an Ar monolayer capacity of 4.2 mmol/g, an interaction constant of $C = 29.75$, and a specific surface area of 359 m^2/g determined using the relative pressure range (0.05 - 0.3), using the cross-sectional area for the argon atom of 14.2 $Å^2$. The

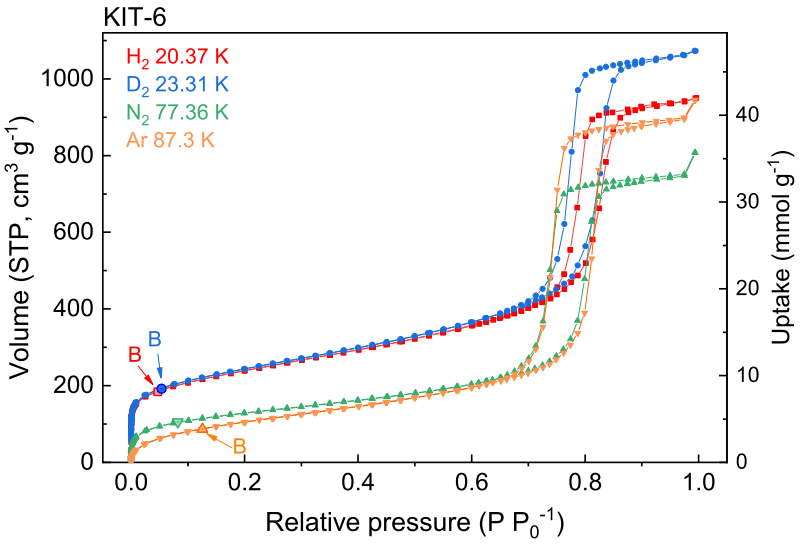

Figure 4.5 *Adsorption isotherms of the mesoporous silica KIT-6.* All isotherms can be classified as type IV. The low-pressure range for H_2 and D_2 isotherms show a higher amount of adsorbed gas related to a higher monolayer capacity.

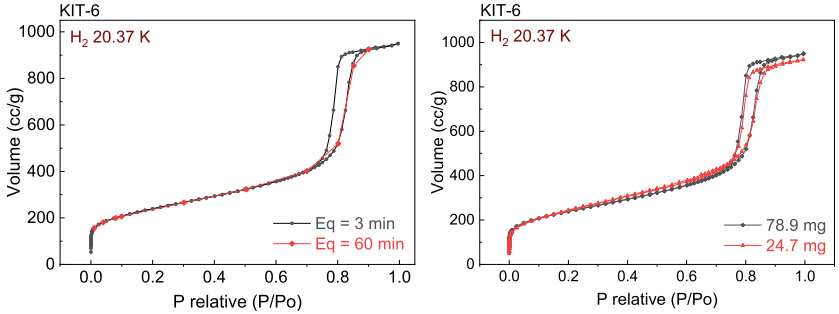

(a) *Equilibrium time.* (b) *Mass sample.*

Figure 4.6 *KIT-6 hydrogen adsorption isotherms varying the sample mass and equilibrium time.* (a) No effect related to the equilibrium time is observed. (b) No effect related to the mass sample is observed.

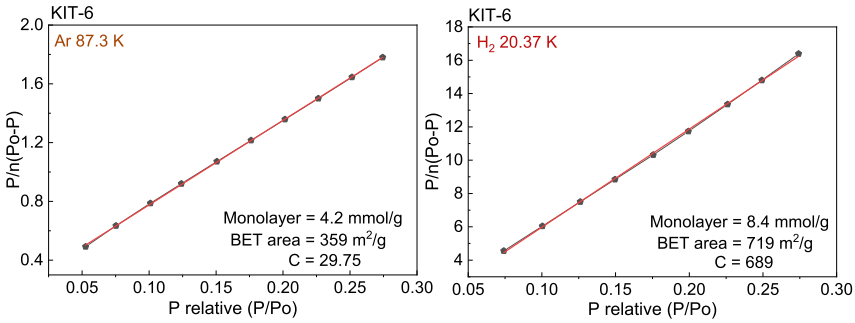

(a) *Argon BET plot.* (b) *Hydrogen BET plot.*

Figure 4.7 *Mesoporous silica KIT-6 BET plots.* (a) The BET plot for argon at 87.36 K leads to a monolayer capacity of 4.2 mmol/g and a $C = 29.75$. (b) The BET plot for hydrogen at 20.37 K leads to a monolayer capacity of 8.4 mmol/g, which is exactly two times higher that Ar. The interaction constant $C = 689$ indicates an interaction higher than for the case of argon.

argon cross-sectional area was calculated using the assumption of a bulk-liquid density in the adsorbed phase and a hexagonal close-packed (*hcp*) 2D layer [26]. The BET analysis of the H_2 and D_2 adsorption experiments yields a monolayer capacity (1ML) of 8.4 and 8.6 mmol/g, respectively. This result indicates that if H_2 and D_2 see the same surface, it will be covered with exactly two times more hydrogen molecules compare to argon atoms (4.2 mmol/g). On the other hand, assuming a hexagonal close-packed 2D layer with a bulk liquid density, *i.e.* H_2 and D_2 cross-sectional area of 14.2 and 12.9 $Å^2$, the monolayer capacities yield BET areas of 719 m^2/g and 664 m^2/g, respectively, which are almost twice the BET area determined by Ar.

The KIT-6 pore size distributions were calculated from Ar and N_2 isotherms by non-local density functional theory (NLDFT) using the kernels contained in the software ASiWwin v3.0 by Quantachrome (N_2-silica equilibrium 77K) and (Ar - zeolite/silica 87 K) assuming cylindrical pores (see Chapter 2). Both analyses show almost identical distributions with one defined peak centered at 10 nm and no microporosity which is consistent with previous pore sizes obtained by TEM

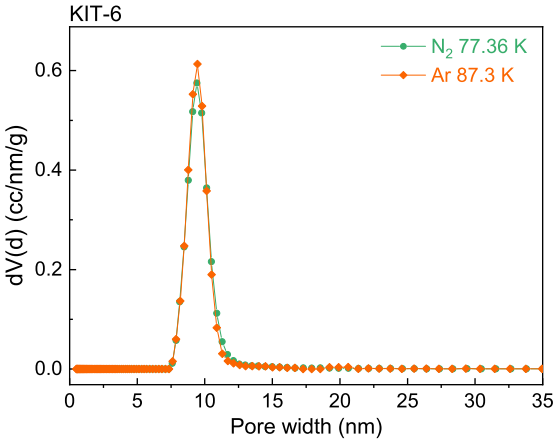

Figure 4.8 *KIT-6 pore size distribution.* Pore size distribution calculated using NLDFT and the N_2 and Ar adsorption isotherms at the condensation temperature, respectively.

for the KIT-6 structure [75, 79]. Furthermore, the KIT-6 pore volume for each isotherm was calculated using the Gurvich's rule [86] at a relative pressure of 0.975 to be: Ar (1.137 cm^3/g), N_2 (1.153 cm^3/g), H_2 (1.189 cm^3/g), D_2 (1.161 cm^3/g).

Non-porous silica nanoparticles Silica-NP

Figure 4.9 shows the isotherms of the non-porous silica nanoparticles (Silica-NP) collected under conditions identical to those used for the silica KIT-6. The isotherm shape for all gases corresponds to type II which is characteristic for monolayer-multilayer adsorption (see Chapter 2, Fig. 2.2). Close to the condensation pressure ($P/P_0 \lesssim 1$) a high amount of gas is adsorbed due to inter-particle condensation. Similar to KIT-6, the H_2 and D_2 isotherms show high capacities at low pressures ($P/P_0 < 0.1$) compared to N_2 and Ar, indicating also a nearly twice as high monolayer capacity for H_2 and D_2.

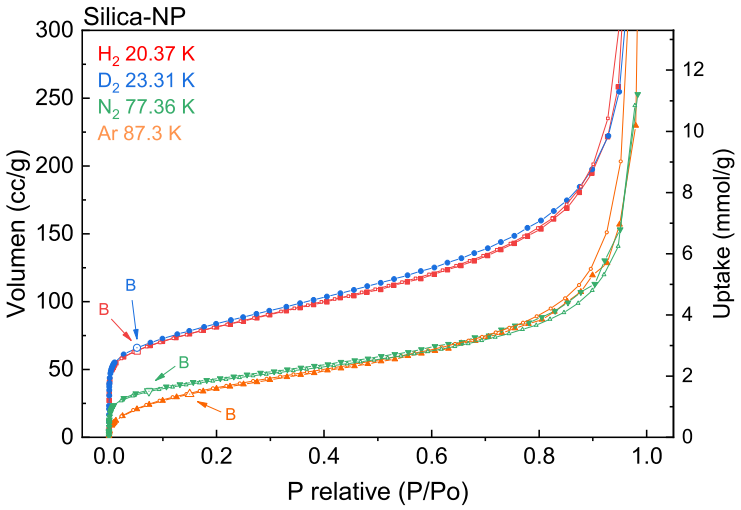

Figure 4.9 *Non-porous silica nanoparticles adsorption isotherms.* H_2, D_2, Ar, N_2 isotherms collected at the condensation temperature, respectively. The H_2 and D_2 isotherms show a high uptake at low relative pressures ($P/P_0 < 0.1$).

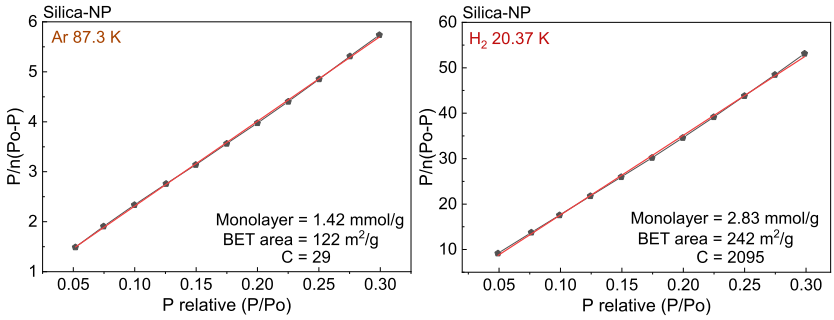

(a) *Argon BET plot.* (b) *Hydrogen BET plot.*

Figure 4.10 *Non-porous silica BET plots.* The H_2 monolayer capacity is almost two times higher than the capacity measured with Argon as in the case of the sample KIT-6 (a) Silica-NP BET plot for argon at 87.36 K. (b) Silica-NP BET plot for hydrogen at 20.37 K.

Figure 4.10 shows the BET analysis of the Silica-NP isotherms using the relative pressure range (0.05 - 0.3) (results are summarized in Table 4.2). The BET plot of the Ar BET analysis (Fig. 4.10a) yields an Ar monolayer capacity of 1.42 mmol/g with an interaction constant C = 29, and a specific surface area of 122 m^2/g. For hydrogen, the BET analysis (Fig. 4.10b) yields a monolayer capacity of 2.83 mmol/g, C = 2095, and a BET area of 242 m^2/g. The H_2 monolayer capacity reveals the double amount of H_2 molecules adsorbed compared to Ar atoms. Under the assumption of a 2D layer with bulk-liquid density the H_2, BET area is approximately twice as large as for Ar.

Porous silica nanoparticles Silica-P

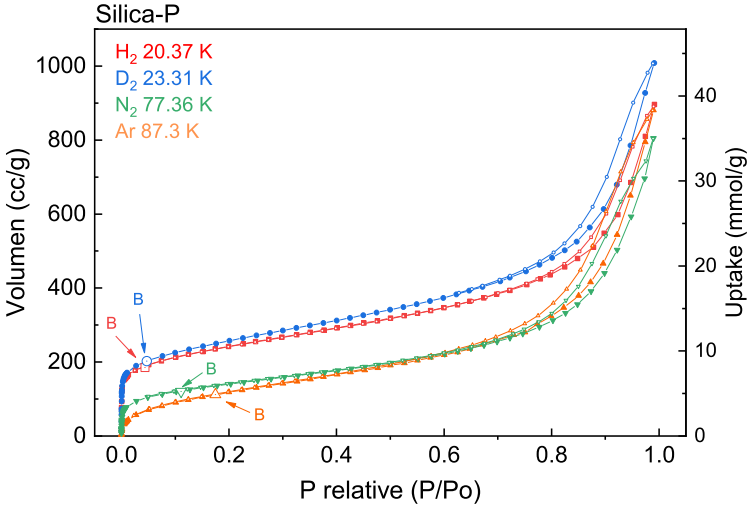

Figure 4.11 *Porous silica nanoparticles adsorption isotherms.* H_2, D_2, Ar, N_2 isotherms collected at the condensation temperature, respectively. The H_2 and D_2 isotherms show a high uptake at low relative pressures ($P/P_0 < 0.1$).

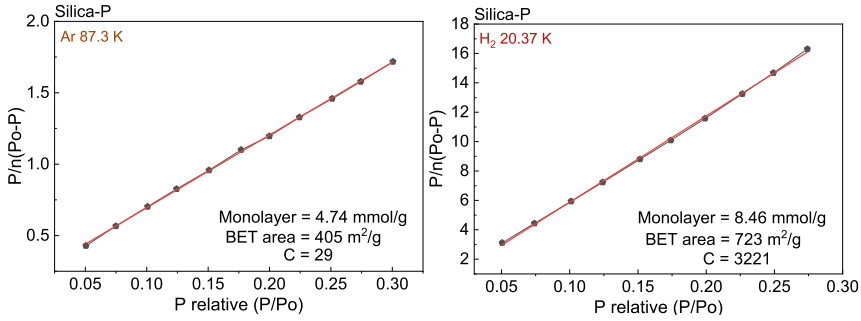

(a) *Argon BET plot.* (b) *Hydrogen BET plot.*

Figure 4.12 *Porous silica particles BET plots.* The H_2 monolayer capacity is almost two times higher than the capacity measured with Argon as the case of the samples KIT-6 and Silica-NP. (a) Silica-P BET plot for Argon at 87.36 K. (b) Silica-P BET plot for Hydrogen at 20.37 K.

Figure 4.11 shows the adsorption isotherms of the porous silica nanoparticles (Silica-P) collected under conditions identical to those used in the silica KIT-6. The isotherms show a very small hysteresis loop formed between the relative pressures 0.8 and 1 which is related to capillary condensation in mesopores (2nm < pore diameter < 20nm). The shape corresponds to a type IV isotherm (see Chapter 2, Fig. 2.2) and the NLDFT analysis indicates the presence of micropores, mesopores, and macropores. Similar to KIT-6, for Silica-P the H_2 and D_2 isotherms exhibit a higher uptake at low relative pressures ($P/P_0 < 0.1$), indicating a higher monolayer capacity of H_2 and D_2.
Figure 4.12 shows the Silica-P BET analysis, and the results are summarized in Table 4.2. The argon BET analysis yields a monolayer capacity of 4.74 mmol/g and a $C = 29$ corresponding to a specific surface area of 405 m^2/g. The hydrogen BET analysis yields a monolayer capacity of 8.46 mmol/g with a $C = 3221$, and a BET area of the 723 m^2/g. Again, the H_2 monolayer is almost twice than for Ar, and the H_2 BET is about the double assuming a 2D layer with a bulk-liquid density.

Mesoporous carbon CMK-3

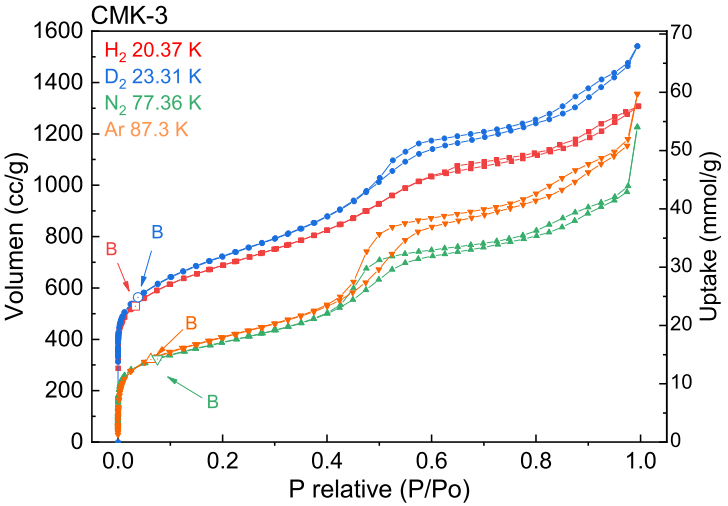

Figure 4.13 *CMK-3 adsorption isotherms.* H_2, D_2, Ar, N_2 isotherms collected at the condensation temperature, respectively. The H_2 and D_2 isotherms show a high uptake at low relative pressures ($P/P_0 < 0.1$) related to a high monolayer capacity.

In order to compare the results of silica to other flat surfaces with different surface chemistry, the adsorption of hydrogen at low-temperature was studied on the mesoporous carbon CMK-3. Figure 4.13 shows the CMK-3 isotherms for all gases at their condensation temperature, respectively. All isotherms show a type IV shape (see Chapter 2, Fig. 2.2) with a hysteresis loop formed between the relative pressures 0.4 and 0.99. The H_2 and D_2 isotherms show a high uptake at low relative pressures ($P/P_0 < 0.1$) similar to the different silicas (see Figs. 4.5, 4.9 and 4.11), and indicating a high H_2 and D_2 monolayer capacity.
The pore size distribution was calculated by quenched solid density functional theory (QSDFT) applied to the CMK-3 Ar and N_2 isotherms using the kernel of the software ASiQwin v3.0 (N_2 - carbon 77.4K) for slit pores. Figure 4.14

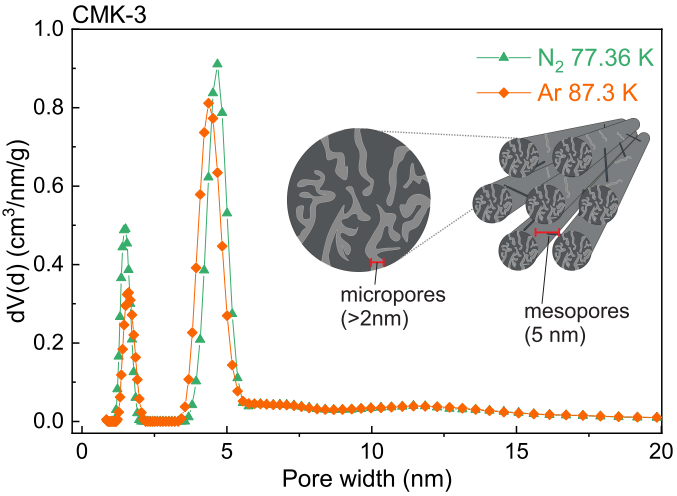

Figure 4.14 *CMK-3 pore size distribution.* Pore size distribution calculated using QSDFT for the N_2 and Ar isotherms at the condensation temperature, respectively. Two peaks located at 5 and 2 nm show the presence of mesoporous and micropores, respectively.

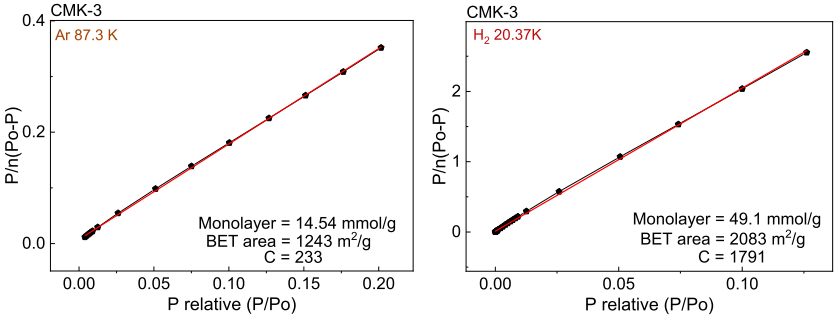

(a) *Argon BET plot.* (b) *Hydrogen BET plot.*

Figure 4.15 *CMK-3 mesoporous carbon BET plots.* The H_2 monolayer capacity is almost two times higher than the capacity measured with Ar very similar to all silica samples. (a) CMK-3 BET plot for Argon at 87.36 K. (b) CMK-3 BET plot for Hydrogen at 20.37 K.

shows the pore size distribution composed by two peaks around 2 and 5 nm, indicating that the porosity is mainly composed by mesopores close to 5 nm and also proving the presence of microporosity (< 2nm), in agreement with previous reports [83, 84]. The CMK-3 pore volume was calculated using the Gurvich's rule for each gas at relative pressure of 0.925 to be: Ar (1.242 cm^3/g), N_2 (1.196 cm^3/g), H_2 (1.414 cm^3/g), D_2 (1.361 cm^3/g).

The BET model is only valid for non-microporous materials because in a micropore, the monolayer–multilayer adsorption and micropore filling processes occur at the same relative pressure (see Chapter 2). According to Rouquerol *et al.* [42] recommendations, the pressure range ($1{\cdot}10^5$ - 0.12) was used. Figure 4.15 shows the BET analysis yielding a monolayer capacity of 14.54 mmol/g with C = 233, and 24.4 mmol/g with C = 1791, for Ar and H_2, respectively. Again, the H_2 monolayer capacity is almost two times larger than for argon. A BET analysis under the assumption of 2D layer with bulk-liquid density yields 1243 for the Ar and almost the double (2083 m^2/g) for H_2.

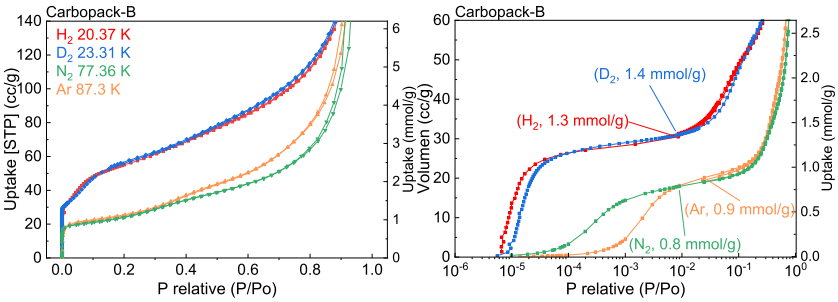

(a) *Linear plot.* (b) *Semi-log plot.*

Figure 4.16 *Carbopack-B adsorption isotherms.* H_2, D_2, Ar, N_2 isotherms collected at the condensation temperature, respectively. (a) The H_2 and D_2 isotherms show a high uptake at low relative pressures ($P/P_0 < 0.1$) compared to N_2 and Ar. (b) At very low pressures $P/P_0 < 0.01$, all the isotherms show a layering transition step where the plateau of each isotherm represents the completion of a monolayer.

Graphitized carbon Carbopack-B

Figure 4.16 shows adsorption isotherms of Carbopack-B for H_2, D_2, Ar and N_2, collected at their condensation temperature, respectively with a first step at very low relative pressures ($P/P_0 < 0.01$). The H_2 and D_2 isotherms increase linearly in the relative pressure range ($0.01 < P/P_0 < 0.1$), whereas the N_2 and Ar remains nearly constant. The gas uptake at $P/P_0 = 0.1$ is almost twice for H_2 and D_2 compared to N_2 and Ar. All isotherms show a small hysteresis loop close to saturation pressure ($P/P_0 > 0.9$), which indicates the presence of macropores that have been previously observed for this structure [87].

For a better analysis of the low-pressure region, Figure 4.16b shows the adsorption isotherms in semi-log scale. At very low pressures, the adsorption rises in a step to a plateau. The plateau defines the completion of a monolayer, called layering transition in the literature [88, 89]. The N_2 isotherm shows a layering transition with a step from $3{\cdot}10^{-5}$ to 0.005 and a plateau at 0.8 mmol/g between $0.005 < P/P_0 < 0.05$. Similarly, Ar shows a layering transition with a step from $1{\cdot}10^{-4}$ to 0.01 and a plateau at 0.9 mmol/g between $0.01 < P/P_0 < 0.1$. In H_2

and D_2, the layering transition occurs in a narrower relative pressure range from $6{\cdot}10^{-6}$ to $5{\cdot}10^{-5}$ with a plateau close to 1.3 mmol/g between $1{\cdot}10^{-4} < P/P_0 < 0.01$.

The amount of gas uptake at the layering transition yields directly the monolayer capacity without any further analysis. The monolayer capacity was determined at the relative pressure 0.01, where the plateau is fully reached for all gases (Fig. 4.16b). This analysis yields an Ar and H_2 monolayer capacity of 0.9 and 1.3 mmol/g, respectively, and clearly shows higher H_2 and D_2 monolayer capacities; which for the same surface means that it is covered with 1.6 times more hydrogen molecules than argon atoms.

The specific surface areas calculated from the monolayer capacities are 76 and 123 m^2/g for Ar and H_2, respectively, under the assumption of a 2D layer with bulk-liquid density for both gases. The huge discrepancy may indicate that this assumption is not valid for H_2.

Macroporous carbon SRB-8F

The macroporous carbon SRB-8F was additionally studied using adsorption isotherms (Fig. 4.17). The BET monolayer capacities yield 0.36 and 0.65 mmol/g for argon and hydrogen, respectively (see Table 4.2). Again, the higher monolayer capacity for H_2 results, under the assumption of a 2D layer with bulk-liquid density, in a higher BET area of 56 m^2/g for H_2 compared to 30 m^2/g for Ar.

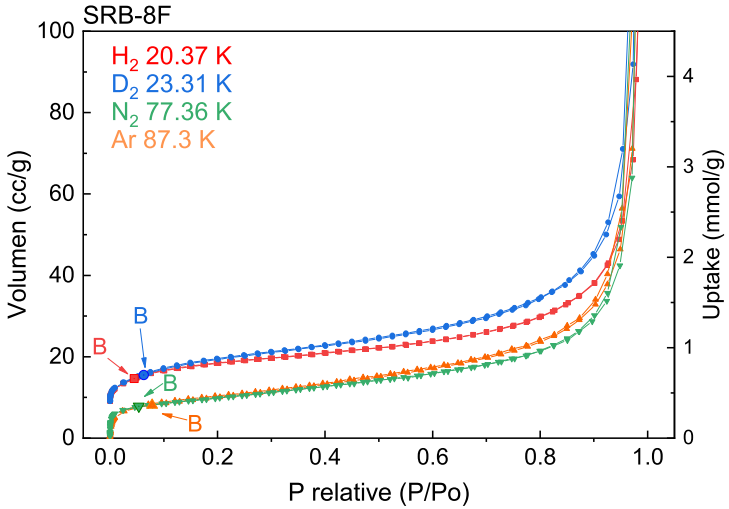

Figure 4.17 *SRB-8F adsorption isotherms.* H_2, D_2, Ar, N_2 isotherms collected at the condensation temperature, respectively. The H_2 and D_2 isotherms show a high uptake at low relative pressures ($P/P_0 < 0.1$) related to a high monolayer capacity.

Table 4.2 Results for silica samples: monolayer capacity, pore volume, surface area, cross-sectional area, and monolayer density.

			BET				Gurvich	
	Gas	T	Monolayer capacity	Specific surface area	Cross-sectional area	Monolayer density	Pore volume	Monolayer ratio*
		(K)	(mmol/g)	(m^2/g)	(Å^2)	(kg/m^3)	(cm^3/g)	($n_m(H_2)/n_m(Ar)$)
KIT-6	Ar	87.3	4.2	359	14.2	–	1.13	
	N_2	77.36	4.6	450	16.2	–	1.11	
	H_2	20.37	8.4	719†	7.10‡	202$^\odot$	1.19	2.0
	D_2	23.31	8.6	664†	6.96‡	413$^\odot$	1.15	2.0
Silica-P	Ar	87.3	4.7	405	14.2	–	–	
	N_2	77.36	5.0	488	16.2	–	–	
	H_2	20.37	8.5	723†	7.96‡	170$^\odot$	–	1.8
	D_2	23.31	9.0	770†	7.47‡	373$^\odot$	–	1.9
Silica-NP	Ar	87.3	1.4	122	14.2	–	–	
	N_2	77.36	1.5	149	16.2	–	–	
	H_2	20.37	2.8	242†	7.14‡	200$^\odot$	–	2.0
	D_2	23.31	2.9	250†	6.90‡	421$^\odot$	–	2.0
CMK-3	Ar	87.3	14.5	1243	14.2	–	1.24	
	N_2	77.36	13.5	1321	16.2	–	1.20	
	H_2	20.37	24.4	2083†	8.47‡	155$^\odot$	1.41	1.7
	D_2	23.31	25.6	1987†	8.07‡	333$^\odot$	1.36	1.8
CarbopackB	Ar	87.3	0.9$^\diamond$	75	14.2	–	–	
	N_2	77.36	0.8$^\diamond$	76	16.2	–	–	
	H_2	20.37	1.3$^\diamond$	123†	8.99‡	141$^\odot$	–	1.6
	D_2	23.31	1.4$^\diamond$	121†	9.14‡	276$^\odot$	–	1.6
SRB-8F	Ar	87.3	0.36	30	14.2	–	–	
	N_2	77.36	0.34	34	16.2	–	–	
	H_2	20.37	0.65	56†	7.88‡	173$^\odot$	–	1.8
	D_2	23.31	0.68	53†	7.58‡	365$^\odot$	–	1.9

† The specific surface area was calculated using the cross-sectional area 14.2 and 12.9 Å^2 calculated using *hcp* the liquid density of the hydrogen and deuterium, respectively; ‡ The cross-sectional area was calculated comparing the monolayer capacity for H_2 and D_2 and the surface area determined by Ar (87 K) adsorption experiments; $^\diamond$ Values obtained at the plateau of layering transition; *Calculated under the assumption that H_2 and Ar see the same surface area, the monolayer capacity ratio indicates how many more molecules (H_2 or D_2) cover the surface compared to Ar; $^\odot$ The equivalent volumetric density of the monolayer is calculated by extending the intermolecular distance (cross-sectional area) in all 3 dimensions forming a hexagonal close-packing lattice.

Discussion

A summary of the adsorption characterization is offered in Table 4.2 for all silica and carbon samples. The monolayer capacity and surface area are given for each gas adsorbate at the respective condensation temperature. In all cases, the hydrogen monolayer capacity is almost two times higher than for argon or nitrogen.
A difference in accessible surface area where the gas atom or molecule probes see different surfaces due to the difference in size (kinetic diameter) is discarded. This interpretation will require a material with a pore structure consisting of micropores that can be only penetrated by hydrogen (2.89 Å) but not by argon (3.5 Å). Furthermore, a large number of micropores will be required to explain the double monolayer capacity for H_2. Such a high number of micropores would also lead to a large difference in pore volume probed by the different molecules/atoms. The pore volume is calculated at pressures close to saturation pressure ($P/P_0 = 1$), filling completely the pores with the adsorbate in liquid phase. Therefore, the nearly identical pore volume obtained by four different gas probes indicates that the same pore structure is seen by the four gases. A detailed analysis of the data will rule out this simple explanation of different accessible porosity.

The most representative sample for a flat surface, low surface defects, regular morphology, and well-defined 3D network of solely mesopores is the silica KIT-6. The pore size distribution of KIT-6 (Fig. 4.8), calculated by NLDFT using the Ar and N_2 isotherms, shows narrow distribution around 10 nm and no microporosity, which is consistent with previous reports in the literature that used adsorption experiments and TEM to study the pore size of KIT-6 [77, 79, 90]. The pore volume determined close to saturation pressure for all gases is similar. This is a clear indication that all probes see the same pore structure, and no "hidden" microporosity exists for KIT-6.

Furthermore, the adsorption experiments of both silica nanoparticles with (Silica-P, Fig.4.11) and without (Silica-NP, Fig. 4.9) porosity show again approximately a twice as high H_2 monolayer capacity compared to Ar or N_2. Similar high monolayer capacities are observed for all silica samples, non-porous, purely mesoporous and meso/micro porous, which rules out the influence of confinement effects on the thermodynamics of the adsorption process.
Additionally to the silica samples, different carbon samples: mesoporous, macroporous and graphitized have been studied. In all carbon samples, a high H_2 monolayer capacity was found compared to Ar; indicating that the surface chemistry between silica and carbon neither have a strong influence on H_2 monolayer capacity.
In general, all the investigated samples with a flat surface compared to the size of the H_2 molecule show up to two times higher monolayer capacity compared to argon.

H_2 adsorbed layer density

The evaluation of the specific surface area using the BET method (see Chapter 2) requires the estimation of the amount of gas adsorbed in the first adsorbed layer or monolayer capacity (ML). Additionally, it requires prior knowledge of the average area occupied by each molecule in a completed monolayer *i.e* the molecular cross-sectional area [91]. Typically, two main assumptions are necessary to calculate the cross-sectional area; (i) the density of the adsorbed layer is close to the bulk-liquid density of the adsorbate; (ii) the adsorbed molecules form a hexagonal-close-packed layer [26, 27]. These assumptions are successfully applied for the characterization of pore structure and surface using common gases *e.g.* Ar, N_2 or CO_2 [36, 38].

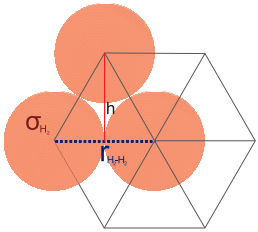

Figure 4.18 *Scheme of the H_2 cross-sectional area and intermolecular distance.* The cross-sectional area (red) is equivalent to the intermolecular distance H_2-H_2 (blue).

Alternatively, the hydrogen cross-sectional area can be experimentally obtained comparing the H_2 monolayer capacity to the specific surface area measured by argon at 87.3 K [1]. The Equation 4.1 relates the specific surface area to the cross-sectional area and monolayer capacity.

$$SSA = n_m \cdot \sigma \cdot N_A \tag{4.1}$$

where SSA is specific surface area; n_m is monolayer capacity in moles per gram; σ is the H_2 cross-sectional area; and N_A is the Avogadro number. In the case of the KIT-6, the cross-sectional area yields σ_{H_2} = 7.10 Å^2, well bellow the cross-sectional area assuming a liquid density (14.2 Å^2). All the cross-sectional areas for H_2 and D_2 are summarized in Table 4.2.

The cross-sectional area is also connected to the intermolecular distance, that represents the distance center-center of two adsorbed molecules H_2-H_2 (Fig. 4.18). Considering that the hydrogen molecules form a 2D layer with a hexagonal distribution (Fig. 4.21), the intermolecular distance of the hydrogen molecules given by Equation 4.2 that assumes seven spherical molecules of radius, $r/2$, placed in the center and the corners of a hexagon. The hexagon contains the equivalent to 3 molecules of hydrogen (6/3 + 1 = 3), and it is formed by 6 equilateral triangles with an area $A = r \cdot h/2 = \frac{\sqrt{3}}{4} r^2$.

$$\sigma = \frac{\sqrt{3}}{2} \cdot r^2 \tag{4.2}$$

where σ is the H_2 cross-sectional area and r is intermolecular separation H_2-H_2. In the case of KIT-6, the H_2 cross-sectional area (σ_{H_2} = 7.10 Å^2) corresponds to an intermolecular distance of 2.9 Å.
Assuming this 2D intermolecular distance is extended in all 3 dimensions forming a hexagonal close-packing lattice; a volumetric density can be calculated using the Equation 4.3, which relates the cross-sectional area σ of the H_2 mole-

[1] The best possible candidate to measure surface areas is argon at 87.3K due to the lack of quadruple moment and its spherical symmetry [36].

cule and a density ρ .

$$\sigma = f(m/\rho N_A)^{2/3} \tag{4.3}$$

where f = 1.091 is the hexagonal close-packed factor, m is the molar mass, N_A is the Avogadro number, and ρ is a volumetric density that would correspond to a bulk-phase of hydrogen with a given cross-sectional area [26, 27] (see Chapter 2).

The analysis of the KIT-6 adsorption results yields a monolayer density of 201.8 kg/cm^3, this density exceeds significantly the bulk-liquid density of hydrogen, ρ_{lq} = 70.9 kg/m^3 which is a common assumption for the density of an adsorbed phase. Moreover, the H_2 monolayer density is more than two times higher than the hydrogen bulk-solid density ρ_{solid} = 80.0 kg/m^3. Despite this density is remarkably high, this analysis is based on the assumption that 2D layer of H_2 molecules is formed on the solid surface, and the volumetric density is only given as a comparison and represents the density that a 3D bulk phase would have for an intermolecular distance of 2.9 Å.

The density of the H_2 and D_2 monolayer for all silica and carbon samples are listed in Table 4.2, all densities are almost two times the bulk-solid density. The high-density layer is a consequence of the high H_2 monolayer capacities obtained for all silica and carbon samples, which shows that the high densities obtained are not dependent on the sample morphology or surface chemistry.

Ab initio calculations

The H_2 cross-sectional areas obtained for all carbon and silica samples analyzed here, implies short intermolecular distances, which are even shorter than those in solid H_2 (3.79 Å), at zero pressure [59]) and that ultimately means monolayer densities higher than the H_2 bulk-solid density (see Table 4.2).

A thorough theoretical analysis motivated by this results was made by the group of Prof. Thomas Heine from Dresden University, that explains the high-density layer in terms of the strong compressibility of the H_2 monolayer together with

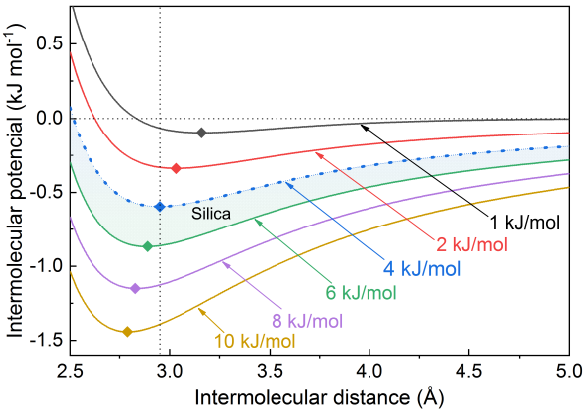

Figure 4.19 *Molecular energy of interaction H_2-H_2.* The plot shows the interaction potential between the molecules that has a minimum energy between 2.8 and 3.2 Å for different surface potentials ($0 < V < 10$ kJ/mol). *The analysis was made by Prof. Thomas Heine, Dresden University.*

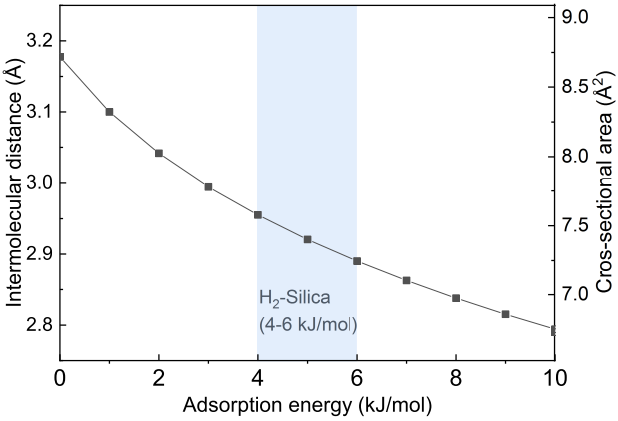

Figure 4.20 *Molecular energy of interaction H_2-H_2.* The intermolecular distance H_2-H_2 is plotted as a function of the adsorption energy. For a interaction H_2-Silica (∼4 kJ/mol), the H_2-H_2 distance is close to 2.9 Å. *The analysis was made by Prof. Thomas Heine, Dresden University.*

the H_2-surface interactions that strongly exceed the intermolecular repulsion H_2-H_2.

The analysis is based on first-principles that express the averaged surface attraction by a Morse potential varying the depth from 1 to 10 kJ/mol. The intermolecular interactions H_2-H_2 in a 2D layer of hydrogen were calculated using coupled-cluster method (CCSD(T)/cc-pVQZ) extrapolated towards basis set and correlation completeness. Combining these two potential contributions gives the Born-Oppenheimer potential model of the adsorbed H_2 layer, for which the Schrödinger equation is solved under the following assumptions; (i) Each H_2 molecule binds with the same adsorption energy to the surface (0-10 kJ/mol); (ii) The H_2 molecules are frozen (that is, the intramolecular bond length is fixed); (iii) Quantum effects were included and the zero-point energy levels were calculated for each considered energy of adsorption. The intermolecular separation H_2-H_2 is given by the minimum in the intermolecular potential.

Figure 4.19 shows the calculated H_2-H_2 interaction potential as function of the intermolecular separation for different adsorption energies (0-10 kJ/mol). The potential decreases with the adsorption energy while its minimum shifts to lower intermolecular distances. Figure 4.20 shows the intermolecular separation as function of the adsorption energy, that is equivalent to the cross-sectional area of a single molecule (Fig. 4.20 - right axis).

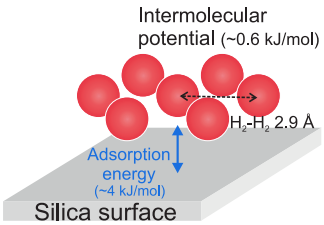

Figure 4.21 *High-dense 2D hydrogen layer. Ab initio* calculations by Thomas Heine shows a intermolecular separation H_2-H_2 of 2.9 Å for an adsorption potential of (4 - 6 kJ/mol), which correspond to a high-density layer assuming a hexagonal close-packed distribution.

The intermolecular separation H_2-H_2 can be used to calculate the molecular cross-sectional area (Eq. 4.2). The corresponding volumetric density is calculated using the Equation 4.3, assuming a hexagonal close-packed arrangement (Fig.

4.21). Table 4.3 shows the intermolecular distance, cross-sectional area and the corresponding volumetric density for different adsorption energies.
For the range of adsorption energies typical for silica (4 - 6 kJ/mol), the layer densities and cross-sectional areas are in the same order of magnitude compared to the densities obtained by adsorption experiments (see Table 4.2). The porous carbon has typical adsorption energies 2 - 6 kJ/mol, that strongly depend on the pore size. The cross-sectional areas obtained for the porous carbon CMK-3 and SRB-8F are close to 8 $Å^2$ that is in well agreement with the theoretical results. The layering transition analysis of Carbopack-B yields a larger cross-sectional area 9 $Å^2$, this can result from the different adsorption potential characteristic of a graphitized surface. An adsorption interaction of 4 kJ/mol, the minimum of the intermolecular H_2-H_2 interaction potential corresponds to 0.6 kJ/mol, which is significantly less than 4 kJ/mol (a value typical for silica surfaces[2]).

Due to the absence of core electrons, it is much easier to compress H_2 (and also its isotopologues as well as He) compared to heavier elements due to the significantly weaker Pauli repulsion of the electron clouds when overlapping upon compression. Because the adsorption energy at the surface exceeds significantly the intermolecular interaction, the adsorbed layer at the surface is highly compressed to a value accounting for about twice the amount expected for uncompressed adsorbates at the hydrogen bulk density.
The adsorption results show a high hydrogen monolayer capacity compared to Ar or N_2 independently of the pore size and morphology. Silica and carbon surfaces have been investigated showing for all samples analyzed here the anomalous[3] hydrogen monolayer capacity that is associated with a high-density 2D layer. Previous reports have observed similar high monolayer capacities at low temperatures on graphitized carbon [4], porous Vycor glass [6] and single-wall carbon nanohorns [17]. In addition, high monolayer capacities have been also observed

[2] In the case of the mesoporous silica KIT-6, the hydrogen isosteric heat of adsorption is 4.0 kJ/mol which was calculated using H_2 isotherms collected at 40, 50, 60 and 77 K.

[3] The high monolayer capacity is referred as anomalous monolayer by Singh and Band in a report of a similar problem with helium [14].

Table 4.3 Parameters obtained using the Heine theory of hydrogen first layer compression mechanism.

Adsorption energy (kJ/mol)	Intermolecular distance (Å)	Cross-sectional area ($Å^2$)	Monolayer density Kg/m^3
0	3.18	8.74	148
-1	3.01	8.32	159
-2	3.04	8.01	168
-3	2.99	7.77	176
-4	2.96	7.56	183
-5	2.92	7.39	190
-6	2.89	7.23	196
-7	2.86	7.10	202
-8	2.84	6.98	207
-9	2.82	6.86	212
-10	2.79	6.76	217

for helium at low-temperature on different surfaces such as carbon [13], gold [72], porous Vycor glass [92] and solid argon [93]. The high-density 2D layer can be explained by the high compressibility of hydrogen, *ab initio* calculations show a low Bohr-Oppenheimer intermolecular potential ($\sim$0.6 kJ/mol) that can be easily overcome by the interaction with a solid surface (typically 4 - 5 kJ/mol for silica).

4.1.2 Inelastic neutron scattering: H_2 layer formation

The highly dense hydrogen monolayer observed at low-temperature was further investigated by *in situ* inelastic neutron scattering (INS) using the vibrational spectroscopy endstation VISION at SNS, ORNL (Spallation Neutron Source, Oak Ridge National Laboratory). The formation of the monolayer was observed by a step-wise dosing of different amounts of para-hydrogen (pH_2) using a manual Sieverts' apparatus. The amount of H_2 was chosen according to the fractions of a monolayer. Furthermore, INS spectra were collected at different temperatures for each dosing point.

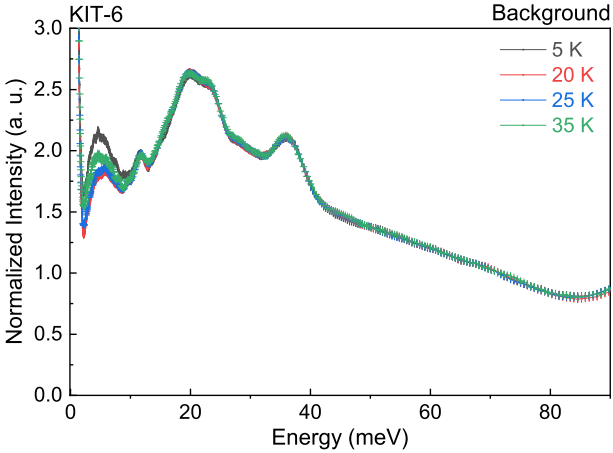

Figure 4.22 *KIT-6 background INS spectra for different temperatures.* The INS spectra are related to the scattering of the sample.

INS mesoporous silica KIT-6

The KIT-6 mesoporous silica (1.213 g) was activated overnight in high-vacuum at 150 °C. Figure 4.22 shows the INS spectrum of the sample holder and sample that was subtracted from all experiments at the corresponding temperature. Different

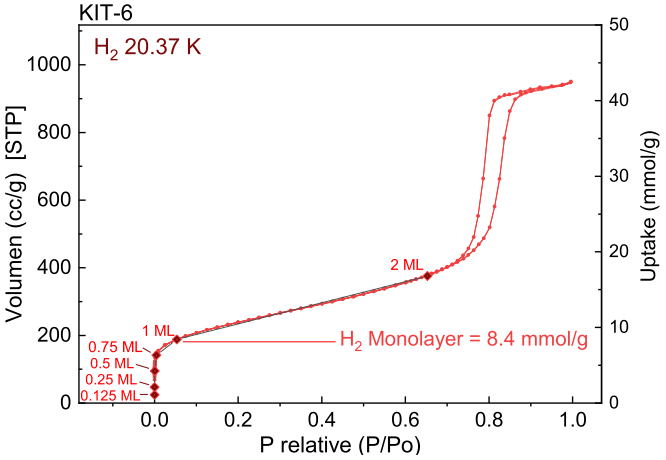

Figure 4.23 *Hydrogen adsorption isotherm for KIT-6 with the dosing points used in the INS experiments.* The loading points of $p\mathrm{H}_2$ are compared with the hydrogen isotherm as fractions of the monolayer capacity.

amounts of hydrogen were dosed corresponding to a fraction (0.125, 0.25, 0.5, 0.75, 1.0ML) of the monolayer (1ML = 8.4 mmol/g). For better comparison to the hydrogen adsorption experiments, the dosing points have been marked in the isotherm (Fig. 4.23). Figure 4.24 shows the KIT-6 INS spectra collected at 20.37 K, for different amounts of para-hydrogen. The spectra show two peaks centered at energies close to 11 and 14 meV which are overlapping with a broad maximum centered at 32 meV. The intensity of these peaks increases for higher amounts of adsorbed para-hydrogen.

The INS spectra can be fitted using seven Gaussian distributions, one for each the peaks at 11 and 14 meV, and five to describe the broad maximum at 32 meV (Fig. 4.25). For each dosing step, the intensity of the peaks *i.e.* the area under the Gaussian, and the mean energy can be evaluated. Figure 4.26 shows the ratio of the areas for the peaks centered at 11 and 14 meV, A_{11meV}/A_{14meV}. The ratio is close to $\sim$5 with relatively small changes for different $p\mathrm{H}_2$ amounts, indicating

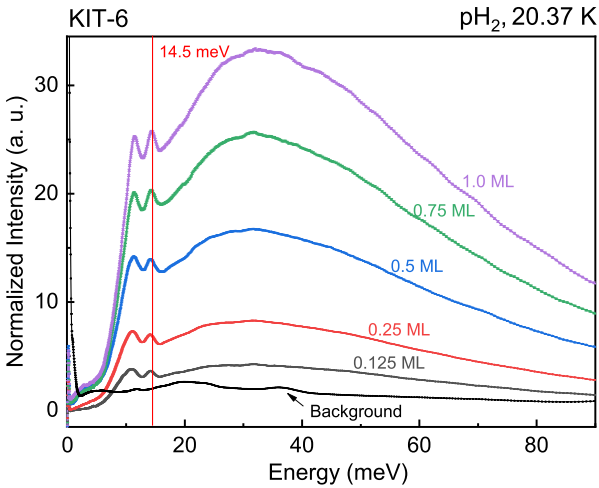

Figure 4.24 *KIT-6 for different* pH_2 *dosing points at 20.37 K.* All spectra show two peaks centered at 11 and 14 meV plus a broad maximum at 32 meV. The intensity increases for higher pH$_2$ amounts.

that both peaks (11 and 14 meV) grow simultaneously with increasing adsorbed H_2. Additionally, Figure 4.27 shows that the mean energy of the peaks at 11 and 14 meV has a small shift to higher energies with increasing adsorbed H_2. The peaks at 11 and 14 meV are associated with the adsorbed state in the first layer since both of them appear for the first hydrogen monolayer fraction used (0.125ML).

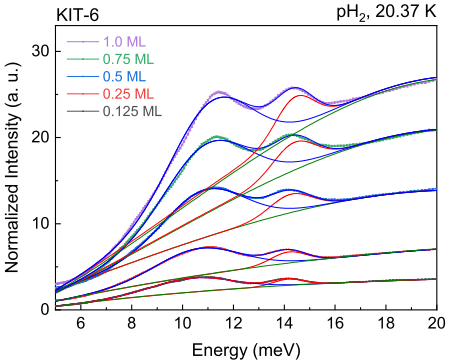

Figure 4.25 *Gaussian fits of 11 and 14 meV peaks for KIT-6*+pH_2. The INS spectra of KIT-6 for different *p*H_2 adsorbed amount and the corresponding fit to a Gaussian for the peaks at 11 and 14 meV.

Figure 4.28 shows the temperature dependence of the INS spectra of the mesoporous silica KIT-6 for different H_2 dosing points. For the lowest amount (0.125ML = 1.05 mmol/g), the INS spectra are nearly identical for all temperatures between 5 to 35 K. With increasing loading, first the spectrum taken at 35 K gets lower while for lower temperatures, the spectra remain nearly constant (Fig. 4.28-0.125ML). At the highest loading (1.0ML = 8.4 mmol/g), the spectra between 5 and 20 K remains similar while for 25 and 35 K the intensity is clearly reduced (Fig. 4.28-1.0ML).

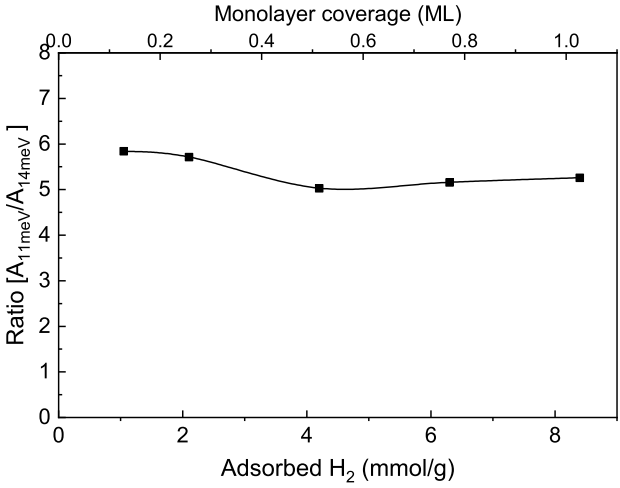

Figure 4.26 *Ratio of the peaks intensities centered at 11 and 14 meV at 20.37 K.* The ratio A_{11meV}/A_{14meV} remains constant close to 5 for different adsorbed $p\mathrm{H}_2$.

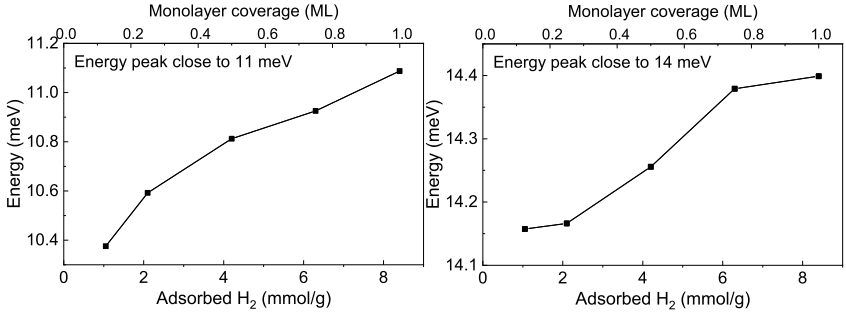

(a) *Energy of the 11meV peak.* (b) *Energy of the 14meV peak.*

Figure 4.27 *Mean energy of rotational hydrogen peaks as function of* pH_2 *amount at 20.37 K.* The mean energy is close to 11 and 14 meV and is increased for higher $p\mathrm{H}_2$ dosing.

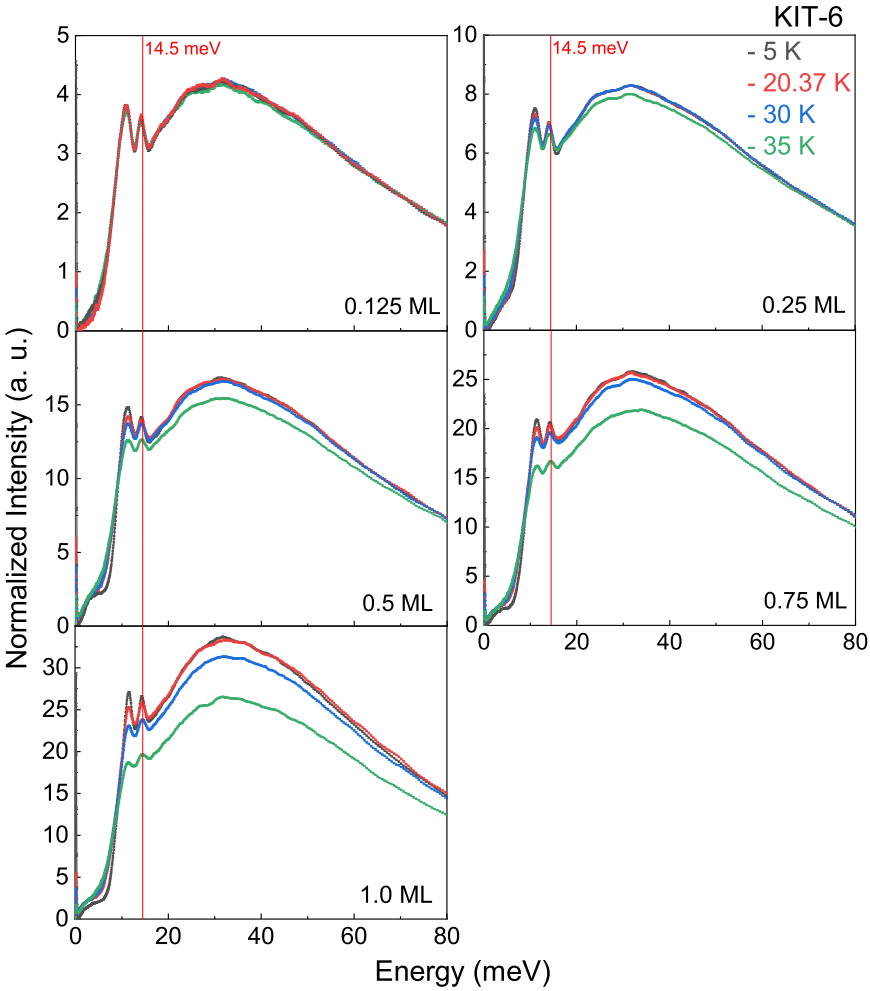

Figure 4.28 *KIT-6 INS spectra for different dosing points collected at 5, 20, 25 and 35 K.* The spectra remain nearly identical at 5 and 20 K for all dosing points.

INS silica nanoparticles

INS experiments on porous (Silica-P) and non-porous (Silica-NP) silica nanoparticles were performed after prior activation of the samples in high-vacuum at 120 °C overnight. A separate background experiment was measured for each sample to collect the signal associated with the sample holder and the sample itself. The corresponding background signal was subtracted from all spectra.

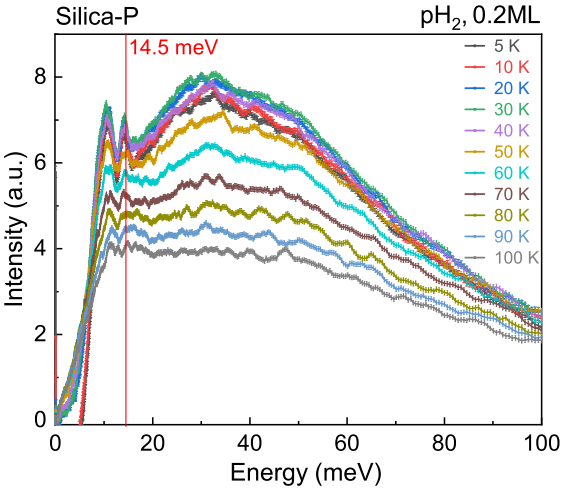

Figure 4.29 *Silica-P INS spectra of* pH_2 *at different temperatures.* The INS spectra show a decreasing intensity with increasing temperature (5 - 100 K) with the amount of pH_2 for the peaks at 11, 14 and 32 meV.

Figure 4.29 shows the INS of Silica-P collected at different temperatures from 5 to 100 K for the lowest dosing point (0.2ML). Similar to the mesoporous silica KIT-6, the spectra show two peaks located at 11 and 14 meV and a broad maximum at 32 meV. The intensity of the peaks centered at 11 and 14 meV remains constant at low temperatures (5 - 30 K) and then decreases for higher temperatures (T $\geq$ 40 K); and finally, at 100 K, the two peaks completely vanish. The intensity of the maximum at 32 meV is nearly constant up to 30 K and then

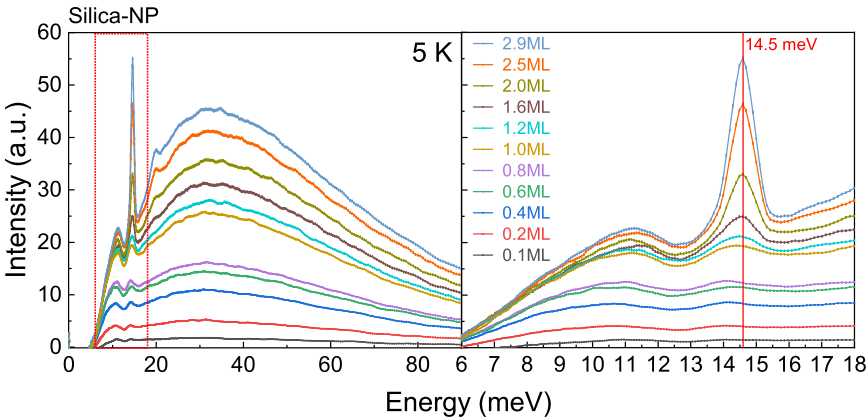

Figure 4.30 *Silica-NP INS spectra for different* pH_2 *dosing points at 5 K.* The INS spectra show an increasing intensity with increasing amount of pH$_2$ for the peaks at 11, 14 and 32 meV. For dosings higher than 1.0ML, the peak centered at 14.5 meV grows suddenly, whereas the 11 meV peak remains nearly constant.

decreases.

Figure 4.30 shows INS spectra collected at 5 K for different dosing points of pH$_2$ (0.1, 0.2, 0.4, 0.6, 0.8, 1.0, 1.2, 1.6, 2.0, 2.5, 2.9 ML) corresponding to fractions of the monolayer coverage (1.0ML = 2.8 mmol/g). Similar to KIT-6, the spectra for all pH$_2$ dosing show a broad maximum at 32 meV, associated to the recoil process, and two peaks at the energies 11 and 14 meV, which are visible for the lowest dosing (0.1ML = 0.28 mmol/g).
For pH$_2$ dosing points above 1.0ML coverage (Fig. 4.30), the peak close to 14 meV grows suddenly in intensity and its energy is shifted to 14.5 meV, whereas the 11 meV peak remains nearly constant.

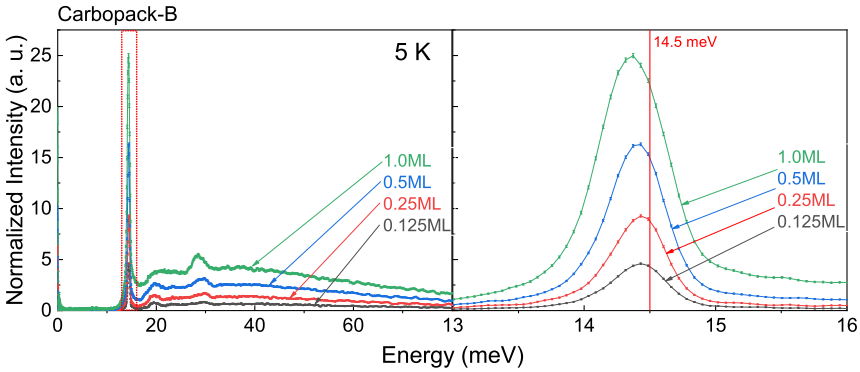

Figure 4.31 *Carbopack-B INS spectra for different* pH_2 *dosing points at 5 K.* The INS spectra show only one peak at 14 meV with an increasing intensity with increasing amount of pH$_2$.

INS carbon surfaces

INS spectra for the graphitized carbon Carbopack-B were collected for different fractions of a monolayer using para-hydrogen. This experiment series allows comparing the results on silica with a carbon surface free of functional groups. Figure 4.31 shows the INS spectra of the graphitized carbon (Carbopack-B) for different dosing points of pH$_2$ (0.125, 0.25, 0.5, 1.0ML) corresponding to a fraction of the monolayer coverage (1.0ML = 1.4 mmol/g) collected at 5 K. In this case, the INS signal shows for the all used coverages (0.125 to 1.0 ML) a peak centered close to 14.5 meV and a small broad maximum at 32 meV.

Discussion

INS spectra of adsorbed hydrogen

The INS spectra of the silica samples KIT-6, Silica-P and Silica-NP show two energy transitions close to 11 and 14 meV, plus a broad maximum at 32 meV. As discused in Chapter 2, the broad maximum centered at 32 meV can be related to the translational recoil of the hydrogen molecule, which is a result of the transfer of momentum to the H_2 molecules without altering the non-translational degrees of freedom of the molecule. Translational recoil of hydrogen molecule appears for both solid as well as for liquid state (see Figs. 2.5 and 2.6 [56]).
The INS spectra of KIT-6 (Fig. 4.24) show the two peaks already at 0.125ML that grow together with increasing dosing. Porous and non-porous silica INS spectra (Figs. 4.30 and 4.29) show again the peaks at 11 and 14 meV and the broad maximum at 32 meV (recoil). The peaks appear simultaneously at the lowest dosing point (0.1ML), indicating that both transitions are associated with the first adsorbed 2D layer studied by adsorption experiments at 20.37 K. For dosings close to one monolayer (1.0ML), the energy of the peak close to 14 meV is shifted to 14.5 meV, which is exactly the free-rotor transition of solid hydrogen.
Because both transitions (11 and 14 meV) grow simultaneously with increasing dosing and have energies close to the free-rotor energy (14.5 meV), they are associated a rotational mode, only observed for solid hydrogen. The transitions then indicate that high-density 2D layer at 20.37 K, studied by adsorption experiments, possesses properties similar to the bulk-solid state (solid-like[4]).
For adsorbed amounts higher than one monolayer (n > 1.0ML) at 20.37 K, these rotational peaks are surpassed by the broad recoil maximum (32 meV) which indicates that the hydrogen molecules adsorbed in upper layers are in a phase similar to the liquid (liquid-like).

[4] *Solid-like* makes reference to the similarity of the INS spectra and the rotational transitions observed, usually associated to bulk-solid hydrogen.

The upper adsorbed layers (Fig. 4.30), located on the top of the first one (1.2, 1.6, 2.0, 2.5, 2.9ML) were studied by INS at 5 K that is below the melting point of hydrogen (14.05 K). The INS spectra for low-coverage (n < 1.0ML) show the two peaks at 11 and 14 meV observed also for KIT-6 and Silica-P. However, for coverages higher than 1.0ML, the peak close to 14 meV grows suddenly in intensity and its energy is shifted to 14.5 meV, whereas the 11 meV peak remains nearly constant.

The increase of intensity and shift in the energy of the peak at 14 meV at higher coverages (n > 1.0ML) resembles the spectrum of the bulk-solid H_2 (see Fig. 2.5) and is associated to additional solid frozen layers of H_2. In this case, the INS spectra were collected at 5 K resulting in upper layers (2nd, 3rd,..) of adsorbed H_2 completely frozen with a state similar to the bulk-solid. Furthermore, the two peaks at 11 and 14 meV grow together up to 1.0ML and they are assigned to the first layer (monolayer) of H_2 molecules.

The final INS spectrum (n > 1.0ML) is the sum of the contribution of the first adsorbed layer (two peaks at 11 and 14 meV, associated to the high-density 2D layer of H_2) and the additional solid layers (one peak at 14.5 meV, free-rotor). Furthermore, this is direct evidence that the first layer (2D layer) of adsorbed hydrogen possesses a high-density because precisely at the coverage 1.0ML, additional solid frozen layers (free-rotor 14.5 meV) start to appear, which marks the completion of one monolayer. This coverage 1.0ML = 2.8 mmol/g is the H_2 monolayer capacity obtained from the isotherm experiments that correspond to twice the monolayer capacity obtained using Ar, implying a molecular cross-sectional area of 7.14 $Å^2$ or more than two times the bulk-liquid density of hydrogen.

Temperature dependence of the INS spectra

The INS spectra of KIT-6 (Fig. 4.28-0.125ML) for the lowest amount of adsorbed hydrogen (0.125ML = 1.05 mmol/g) show no change with increasing temperature (5 - 35 K) and the intensity remaining constant for both peaks at 11 and 14 meV.

This indicates that adsorbed hydrogen at low coverage has rotor transitions (solid-like) up to 35 K.
For higher amounts of adsorbed hydrogen (Fig. 4.28) the intensity of spectra decreases with increasing temperature; especially the intensity of the rotor peaks at 11 and 14 meV. When the surface of KIT-6 is completely covered with one layer (1.0ML = 8.4 mmol/g), the spectra (Fig. 4.28-1.0ML) remain identical at the temperatures 5 and 20.37 K but decrease for higher temperatures (25 and 35 K). Hence, the state of the first adsorbed layer at 5 K (assuming that below the melting temperature, the adsorbed phase is completely frozen) remains the same at 20.37 K (boiling temperature), which also indicates that 2D layer is in a solid-like state at 20.37 K.

The temperature dependence of the H_2 adsorbed phase was further investigated for sample Silica-P. The intensity of the spectra is clearly reduced from 5 to 100 K (Fig. 4.29). The scattering intensity is proportional to the number of H_2 molecules adsorbed on the surface of the sample. As the temperature increases, the weak interaction (van der Waals, H_2-Surface) is overcome by the thermal fluctuations, and the H_2 molecules are desorbed from the surface which then reduces the intensity of the scattered signal.
At higher temperatures ($T > 40$ K), the rotational peaks at 11 and 14 meV almost disappear yielding an INS spectrum composed only of the broad recoil maximum (32 meV).
The INS spectra of liquid hydrogen (Fig. 2.6 [56]) shows a spectrum with a broad maximum centered close to 32 meV. Hence, the adsorbed hydrogen is closer to a liquid phase and the solid-like 2D layer is no longer present for higher temperatures ($T \geq 40$ K). In contrast, below 30 K, the rotational peaks are clearly defined indicating that solid-like 2D layer can be observed only at low-temperature close to liquefaction (20.37 K).

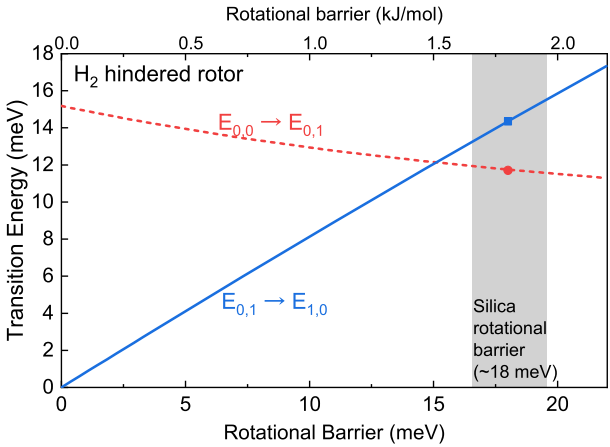

Figure 4.32 *Energy transitions of H_2 molecule for a hindered rotor (Evett model).* The rotational barrier of 18 meV, typical value for polar surfaces, yields energies for the transitions E[0,0→0,1] and E[0,1→1,0] of 11.7 and 14.6 meV, respectively.

Vibrational-rotational transitions of adsorbed hydrogen

For all experiments on silica samples (KIT-6, Silica-NP, and Silica-P), the INS spectra show two peaks even at the first loading point (0.125ML) indicating that the hydrogen molecules in the first adsorbed layer can be excited with two different energies close to 11 and 14 meV, which is very close to the free-rotor energy transition (14.5 meV) observed for bulk-solid hydrogen (see Fig. 2.5). To explain the additional peak at 11 meV , the presence of hydroxyl groups on the silica surface has been taken into account.

The silica surface is usually covered with silanol groups Si-O-H (hydroxyl groups), the concentration depends on sample treatment, but most oxide surfaces are hydroxylated to some extent. L. Zhuravlev [94] found that even prolonged calcination at elevated temperature and high vacuum cannot remove hydroxyl groups completely. All the studied silica samples were dried under vacuum at 150 °C, and no further treatment was used to remove the hydroxyl groups

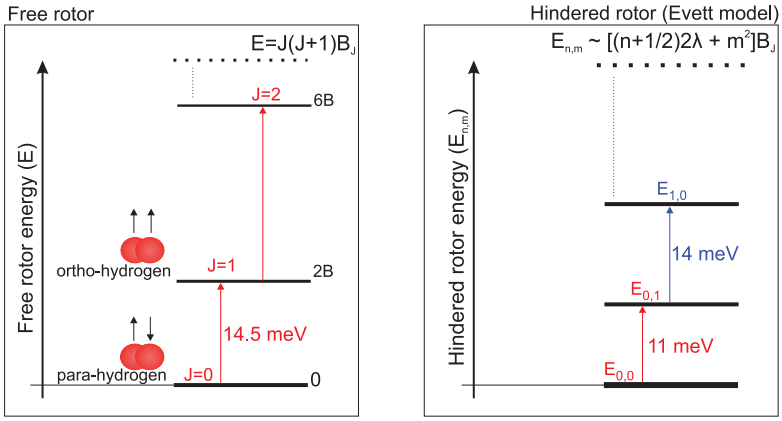

(a) *Free rotor energy transitions.* (b) *Evett hindered rotor energy transitions.*

Figure 4.33 *Free rotor and hindered rotor energy levels.* (a) Energy transition of the free-rotor (14.5 meV) observed for solid hydrogen (Fig.2.5). (b) Hindered rotor energy transitions (11 and 14 meV) of adsorbed hydrogen on silica for a rotational barrier of 18 meV (Figs. 4.24, 4.30 and 4.29).

from the surface. Previous reports by Huber *et al.* [5, 73] using vibrational spectroscopy showed that hydroxyl groups act as adsorption sites for small molecules on the silica surface.

The splitting into two peaks or degeneracy of the free-rotor may be due to an additional potential caused by the hydroxyl groups on the silica surface. These hydroxyl groups create a chemically inhomogeneous surface for the H_2 molecule that introduces an extra potential acting as a rotational barrier. This rotational barrier can modify the quantum rotational states (free-rotor) yielding hindered rotational transitions.

To prove these arguments, a numerical analysis was made by the group of Prof. Thomas Heine at Dresden University. The analysis is based on the model proposed by A. Evett [95] to calculate the energy of the vibrational-rotational transitions (hindered rotor, Fig. 4.33) when the hydrogen molecule is placed in a

rotational barrier [96] given by

$$E_{[n,m]} = \left[\left(n+\frac{1}{2}\right)2\lambda + m^2\right]h^2/8\pi^2 I \qquad \begin{matrix} n = 0,1,2,... \\ m = 0,1,2,... \end{matrix} \tag{4.4}$$

where n is a quantum number associated to the vibration of the H_2 molecule respect to the surface, m is quantum number associated to the rotation of the molecule, I is the moment of inertia and λ^2 is the height of the rotational barrier divided by $B_J = h^2/8\pi^2 I$. Figure 4.32 shows the energies $E_{n,m}$ of the rotational-vibrational transitions E[0,0→0,1] (red dotted line) and E[0,1→1,0] (blue line) as function of the rotational barrier potential.

For a rotational barrier of 18 meV (1.8 kJ/mol), a typical value for polar surfaces, the energy transitions yield E[0,0→0,1] = 11.7 meV and E[0,1→1,0] = 14.6 meV, which is in full agreement with the INS spectra observed for the silica surfaces. Hence, Evett model explains the two transitions of the INS spectrum of silica as two rotational-vibrational transitions of a hindered rotor.

Figure 4.34 shows a schematic representation of the hydrogen adsorption on silica at low temperatures (∼20 K). The first layer of adsorbed hydrogen is adsorbed forming a highly dense 2D layer with a state similar to solid (solid-like). On the top of the first layer, upper layers with a liquid-like phase can be adsorbed, with part of the hydrogen molecules not adsorbed remaining in gas phase. Additionally, the scheme shows some molecules on the first layer are tilted representing that the high-density 2D layer of hydrogen has two rotational-vibrational modes. If the temperature considered is below the melting point of hydrogen (5 K), the upper layers would be in a state similar to bulk solid instead of liquid.

The INS spectra collected at 5 K for graphitized carbon Carbopack-B (Fig. 4.31) show one rotational transition for all dosing points (0.125, 0.25, 0.5, 1.0ML), close to the hydrogen free-rotor transition line at 14.5 meV (Fig. 2.5). The

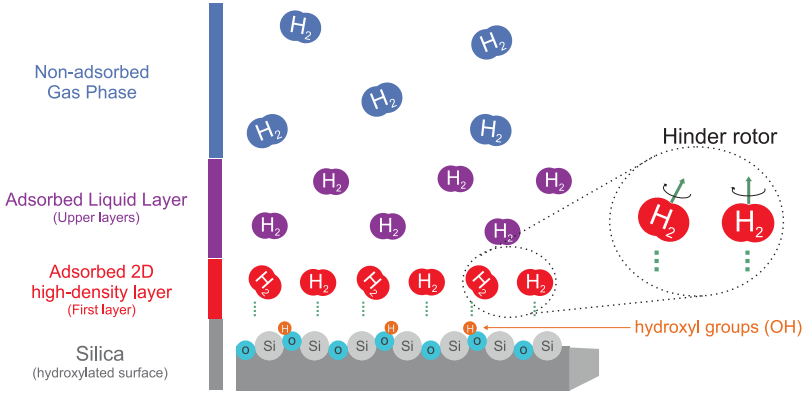

Figure 4.34 *Schematic illustration of the hydrogen layer formation on silica at 20.37 K.* The first adsorbed layer of hydrogen has a high-density. The additional layers are adsorbed on top with a density similar to a liquid. The tilted and non-tilted hydrogen molecules in the first layer represent two different rotational-vibrational modes induced by the presence of hydroxyl groups.

INS spectra show also broad peaks close to 20 and 28 meV which are probably related to higher rotational transitions of the hydrogen molecule.

The H_2 molecules located the first adsorbed layer (2D layer) on the graphitized surface have a state similar to bulk-solid (solid-like) but no hindered rotational modes are observed, because of the absence of functional groups that would generate a rotational barrier; contrary to the observations in silica surfaces (hydroxyl groups on the surface) that yield two rotational-vibrational states. Furthermore, the H_2 isotherm of Carbopack-B (Fig. 4.16) shows a layering transition for all gases analyzed. This is consistent with a surface free of functional groups because the layering transition can be observed, clearly, only for homogeneous flat surfaces (*e.g* graphitized surfaces) [88].

Comparison with literature

Only a few reports have focused on hydrogen adsorbed on porous materials at low-temperature using INS experiments, these reports have observed two transitions close to the free-rotor energy (14.5 meV) indicating rotational-vibrational energies of a hindered rotor.

Honeybone *et al.* [97] studied trapped molecular hydrogen in amorphous hydrogenated carbon. Figure 4.35 shows their INS spectrum with two broad peaks centered at 12.5 and 16.0 meV, which may be assigned to two different transitions of a hindered rotor. Moreover, Honeybone *et al.* [97] determined an average energy for both peaks and use it to calculate the length of the hydrogen molecule H-H (0.72 Å). They proposed that the bond length is lower that gaseous hydrogen (0.75 Å), similar to a high-pressure ($\sim$1 GPa) hydrogen environment.

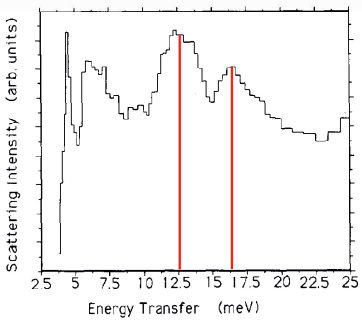

Figure 4.35 *INS of hydrogenated carbon (reproduction).* Reprinted from Honeybone *et al.* [97], Copyright 1991, with permission from Elsevier.

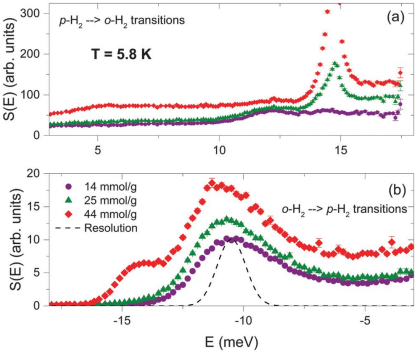

Figure 4.36 *INS of MCM-41 mesoporous silica (reproduction).* The INS spectra show two transitions at 11 and 15 meV. Republished with permission of Royal Society of Chemistry, from Prisk *et al.*[74], Copyright 2014; permission conveyed through Copyright Clearance Center, Inc.

Prisk *et al.*[74] used INS to study adsorbed hydrogen at 5.8 K on the mesoporous silica MCM-41 that has a pore size of 3.4 nm (see Table 4.1). Figure 4.36 shows the INS spectra with two peaks at 11 and 15 meV which are explained as a direct consequence of the surface heterogeneity of the MCM-41, which perturbs their rotational wavefunctions and shifts their energy levels from those of a free quantum rotor. Furthermore, Prisk *et al.* [74] also compared N_2 (77 K) and H_2 (19.6 K) isotherms and found a large H_2 monolayer capacity obtaining a cross-sectional area of 10.3 $Å^2$, but it was not futher discussed. According to the analysis used in the first section of this Chapter, the cross-sectional area would correspond to a H_2 density of 115 kg/m^3, higher than bulk-solid density. Consequently, the adsorption and INS results obtained by Prisk *et al.* [74] are in full agreement with the results and analysis presented here for all silica samples showing a high dense 2D layer of hydrogen adsorbed at low temperatures.

Olsen *et al.* [98] studied by INS adsorbed hydrogen at 23 K on several porous carbons with pore sizes close to 1.2 nm. Figure 4.37 shows their INS spectrum with two peaks close to 14.5 meV. The peaks are observed for several samples and are explained as vibrational-rotational transitions of a hindered ro-

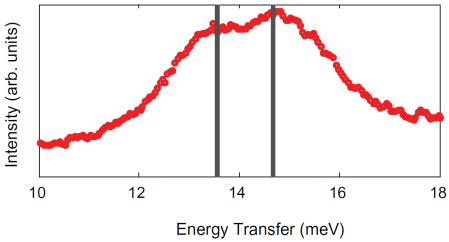

Figure 4.37 *INS of porous carbon (reproduction).* The spectra show two peaks centered at 13.5 and 14.7 meV reproduced from. Reprinted from R. Olsen *et al.* [98] Copyright 2013, with permission from Elsevier.

tor.

Another explanation for the two peaks in the INS spectra of silica is the existence of two different adsorption sites with different binding strength. The H_2 molecules are then adsorbed on different points on the surface yielding different elongations of the H-H molecular bond. The energy shift from the free-rotor energy to lower energies can be explained as a stretch of the hydrogen molecule due to the adsorption binding energy [58, 99, 100]. For KIT-6 at the lowest adsorbed amount (0.125ML) at 20 K, the energy of the first peak at 14 meV would mean a stretch of the hydrogen intermolecular bond to 0.7645 Å and for 11 meV up to 0.898 Å. Such bond length would indicate electron transfers to the adsorption site that would imply a stronger H_2-silica surface interaction; so far only observed for open-metal sites in MOFs [100]. Furthermore, the required elongation of the H_2 molecular bond maybe even larger than the maximum length where the hydrogen molecule splits in atomic hydrogen.

4.2 Adsorption on fragmented surfaces

The adsorption of hydrogen has been discussed for relatively flat surfaces compared to H_2 molecule such as mesoporous silica and carbon. As a comparison with flat surfaces, the adsorption of hydrogen at low temperatures was further investigated using a metal-organic framework (MOF-205). MOFs are composed of linkers and metal-oxide clusters (corners) that form a 3D structure. Hence, the extent of a continuous surface is restricted to the size of the organic linker or the size of the corners, these discontinuities create a fragmented surface. In addition, MOFs are chemically heterogeneous due to the different interaction strengths of the linker and metal corners. The framework MOF-205 was analyzed by cryadsorption experiments and the density of the H_2 BET monolayer was calculated. Additionally, *in situ* inelastic neutron scattering experiments were used to study the adsorbed state of H_2 molecules.

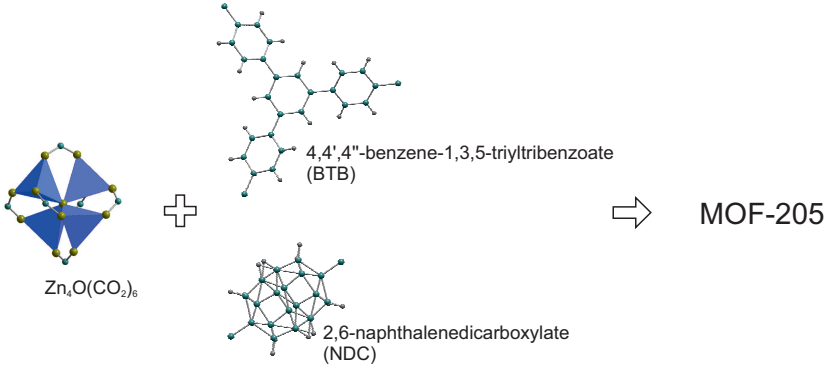

Figure 4.38 *MOF-205 building units.* MOF-205 is constructed by a metal-oxide cluster $Zn_4O(CO_2)_6$ and the linkers *BTB* and *NDC*.

MOF-205 (DUT-6) MOF-205 is constituted with a metal center octahedral unit $Zn_4O(CO_2)_6$ and two organic linkers *BTB* (4,4',4"-benzene-1,3,5-triyltribenzoate) and *NDC* (2,6-naphthalenedicarboxylate) shown in Figure 4.38. The structure was first reported and named by the group of Stefan Kaskel of Dresden University as DUT-6 (DUT = Dresden University of Technology) in the year 2009 [101]. In 2010, the group of Omar Yaghi [102] reported it as part of a series of structures (MOF-177, MOF-180, MOF-200, MOF-205, and MOF-210) with a BET area of 4460 m^2/g that is one of the highest BET areas among the currently available porous materials.

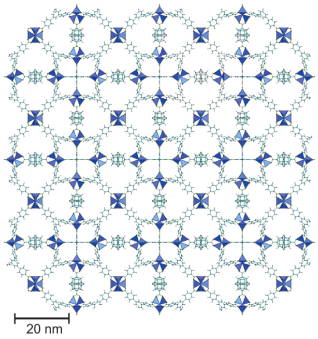

Figure 4.39 *MOF-205 framework structure.* MOF-205 shows a large pore structure with cavities with diameter of 30 Å.

The structure is cubic with a space group $Pm\bar{3}n$. Dodecahedral mesoporous cages with 25 - 30 Å diameter are formed by twelve $Zn_4O_6^+$ nodes, four *NDC* linkers, and eight *BTB* linkers [102]. A second type of pore (cubic shape) constructed from four $Zn_4O_6^+$ clusters, two *NDC* linkers, and four *BTB* linkers is also present in the structure. These smaller pores are arranged to connect the larger dodecahedral cages to form a periodic space-filling (inter-mesopore cages) with a pore volume of 25 $Å^3$. The reported nitrogen adsorption isotherm of MOF-205 at 77.3 K reaches saturation at 1380 cm^3/g, which yields 2.02 cm^3/g as total pore volume [101]. The sample analyzed in this investigation was synthesized by the group of Ulrich Müller from BASF SE, Germany.

4.2.1 Adsorption experiments and BET analysis

MOF-205 gas adsorption properties were studied using high-resolution cryo-adsorption experiments for four different gases (H_2, D_2, N_2 and Ar) at their condensation temperature, respectively. Figure 4.40 shows the MOF-205 adsorp-

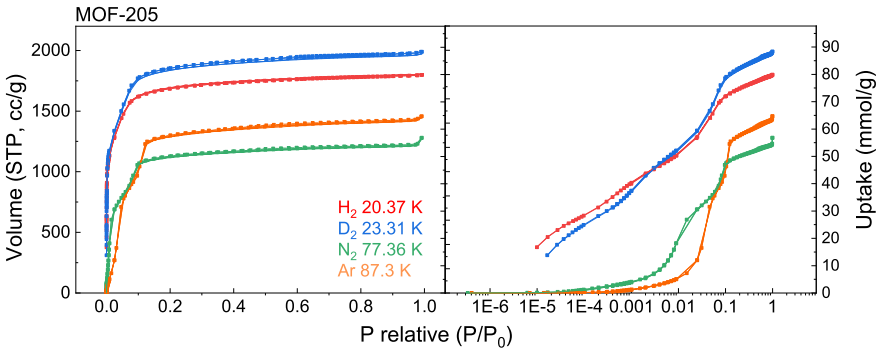

Figure 4.40 *MOF-205 adsorption isotherms.*The isotherm comparison plot shows a similar shape (type I) for all the adsorbates and different steps at low pressure ($P/P_0 < 0.1$). (left) Linear plot of the adsorption isotherms. (right) Logarithmic plot of the adsorption isotherms.

tion isotherms for all the used gases. The shape of all isotherms resemble a type I isotherm (see Chapter 2, Fig. 2.2) typically associated with the presence of micropores [37]. All isotherms show several steps at low relative pressures ($P/P_0 < 0.1$). Figure 4.40 (right) shows a semi-log plot of the adsorption isotherms where the low-pressure range is expanded. The first steps are located at 0.03 and 0.1 in the case of argon, and at 0.08 and 0.008 in the case of nitrogen. For H_2 and D_2, the isotherms have a higher uptake at low-pressure, with steps at $1x10^{-5}$, 0.001 and 0.05.

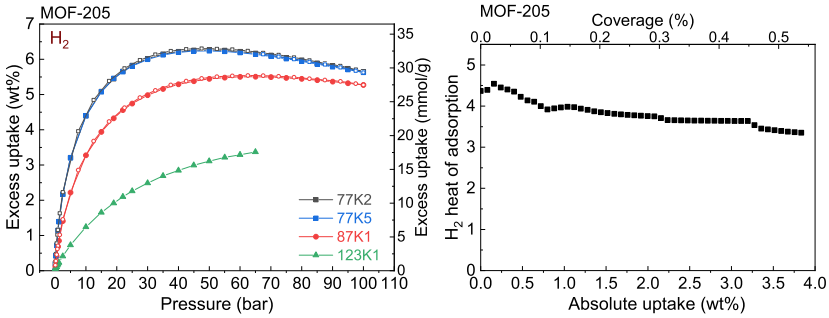

(a) *H_2 high-pressure isotherms.* (b) *Isosteric heat of adsorption..*

Figure 4.41 *MOF-205 high-pressure hydrogen adsorption.* (a) At 77 K, MOF-205 has an uptake of 6.2 wt%, and a saturation close to 50 bar. (b)The average heat of adsorption is 3.7 kJ/mol.

High-pressure isotherms

The interaction of hydrogen with the porous framework MOF-205 was further studied using high-pressure adsorption experiments. The skeleton volume of the sample was measured by He test at room temperature (Fig. 3.13) to be 0.0392 cm^3 (see Chapter 2). The skeleton density was calculated using the sample dry mass (0.05232 g), and yields 0.7492 cm^3/g. Figure 4.41a shows the high-pressure hydrogen isotherms collected for the temperatures 77, 87 and 123 K, up to a pressure of 100 bar. The excess hydrogen capacity was obtained after buoyancy correction using the skeleton density. The isotherm at 77 K shows the maximum excess uptake of 6.28 wt% (7.57 wt% absolute uptake) at 50 bar. The isosteric heat of adsorption was calculated using the Van Hoff equation (Eq. 2.8) from the isotherms collected at 77 and 87 K. Figure 4.41b shows the MOF-205 isosteric heat of adsorption that decreases from 4.5 kJ/mol at low uptakes down to 3.5 kJ/mol at the maximum uptake. The average heat of adsorption was calculated to be 3.7 kJ/mol.

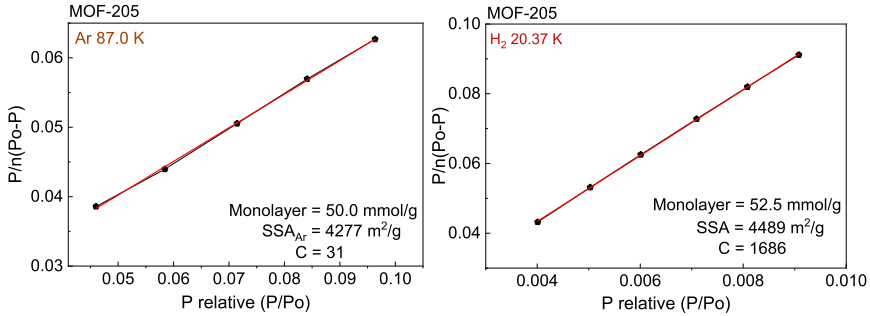

(a) *Argon BET plot.* (b) *Hydrogen BET plot.*

Figure 4.42 *MOF-205 BET plots.* Similar surface areas are obtained for argon at 87.36 K (a) and hydrogen at 20.37 K (b).

Surface area and density analysis

The MOF-205 isotherms of all gases, collected at condensation temperatures, were analyzed using the BET method (see Chapter 2) to calculate the monolayer capacity and BET area (Table 4.4). Figure 4.42 shows the BET plot for Ar and H_2. In both cases, the discontinuous filling of the different adsorption sites creates different slopes in the BET plot that makes the surface area analysis difficult. The analysis for argon yields a BET monolayer capacity (Fig. 4.42a) of 50.0 mmol/g and C = 31, using a relative pressure range P/P_0 = 0.004 - 0.1. The H_2 analysis (Fig. 4.42b) yields a BET monolayer capacity of 52.5 mmol/g and C = 1686 using a relative pressure range of P/P_0 = 0.004 - 0.01. The pressure range have been selected to fulfill both criteria according to Rouquerol *et al.* recommendations [42] (see Chapter 2).
The BET areas for Ar and H_2 yield 4277 m^2/g and 4489 m^2/g, respectively[5] (see Table 4.4), which is in agreement with previously reported values around 4400 m^2/g [101–103].

[5]The H_2 and Ar BET areas were calculated using the molecular cross-sectional areas assuming a bulk-liquid density in the adsorbed phase and a hexagonal close-packed (*hcp*) 2D layer [27].

Table 4.4 Results of MOF-205: BET monolayer capacity, BET area, and pore volume.

Sample	Gas	Temperature (K)	BET		Gurvich
			BET monolayer capacity (mmol/g)	BET area (m^2/g)	Pore volume (cm^3/g)
MOF-205	Argon	87.3	50.0	4277	1.80
	Nitrogen	77.36	42.1	4107	1.87
	Hydrogen	20.37	52.5	4489†	2.28
	Deuterium	23.31	53.8	4219†	2.14

† The BET areas were calculated using the cross-sectional areas Ar(14.2 Å^2), N_2(16.2 Å^2), H_2(14.2 Å^2) and D_2(12.9 Å^2) assuming *hcp* distribution and bulk-liquid density.

Taking the BET area measured by Ar and the H_2 BET monolayer capacity and using Equation 4.3 yields a H_2 monolayer density ($\sim$76 kg/m^3) very close to bulk-liquid ($\sim$70 kg/m^3). The pore volume was calculated at the relative pressure $P/P_0 = 0.95$ and yields Ar (1.804 cm^3/g), N_2 (1.873 cm^3/g), H_2 (2.277 cm^3/g) and D_2 (2.141 cm^3/g), which is also close to previous reports [101].

Adsorption at high-pressure

An additionally analysis from the high-pressure isotherm was made to calculated the specific surface area taking the maximum hydrogen uptake[6] and the hydrogen surface density at 77 K ($\rho_{77K} = 0.0183$ mg/m^2) experimentally obtained from many porous materials (see Chapter 2) [3]. The maximum absolute uptake of MOF-205 at 50 bar and 77 K is 7.57 wt% = 81.94 mg_{H_2}/g (Fig. 4.41a), and corresponds to a surface area of 4477 m^2/g; very close to the H_2 BET area (4489 m^2/g).

[6]The hydrogen uptake at high-pressure has a linear relation with the surface area given by Chahine's rule (see Chapter 2).

4.2.2 Vibration neutron spectroscopy

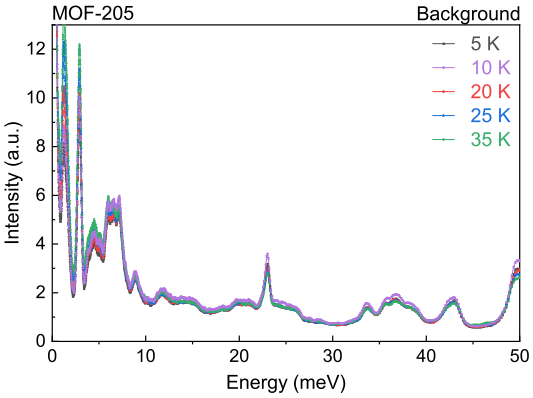

Figure 4.43 *MOF-205 INS background.* The spectra were collected in vacuum at 5, 10, 20, 25 and 35 K.

The hydrogen adsorption on MOF-205 was further investigated by *in situ* INS applying a step-wise dosing of different amounts of para-hydrogen (pH_2) using a manual Sieverts' apparatus. The amount of hydrogen was chosen according to fractions of the BET monolayer. Furthermore, INS spectra have been collected at different temperatures for each dosing point. Prior to the experiments, the sample (0.75 g) was activated at 150 °C in high-vacuum in order to remove any adsorbed molecule. Figure 4.43 shows the background signal (subtracted in all cases) associated with the sample holder and the sample itself.
Figure 4.44 shows the INS spectra of MOF-205 for different pH_2 dosing points (0.03, 0.06, 0.125, 0.25, 0.5, 0.75, 1.0ML) corresponding to fractions of a monolayer 1.0ML = 52.5 mmol/g. Five peaks centered at 11.5, 12.2, 13.0, 14.0, 15.3 and 15.5 meV appear at different pH_2 dosing points, *i.e.* the peaks grow successively with the amount of pH_2.
At the first dosing point (0.03ML), two peaks centered at 11.2 and 12.8 meV are observed. At 0.25ML, two new peaks appear centered at 12.2 and 13.8 meV.

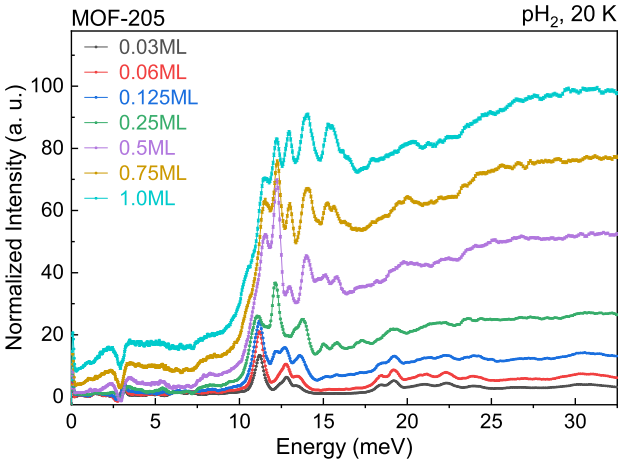

Figure 4.44 *MOF-205 INS spectra for different* pH_2 *dosing.* The spectra were collected for different dosing points equivalent to a fractions of a monolayer (1.0ML = 52.5 mmol/g).

For the next dosing point (0.5ML), a new peak appears at 11.5 meV and the peak at 11.2 is still visible as a shoulder; and three new additional peaks are observed at 13.0, 15.2 and 15.8 meV. The spectrum at the highest pH_2 amount (1.0ML) is composed of five peaks at 11.5, 12.2, 13.0, 14.0, 15.3 and 15.5 meV. In addition, a broad maximum centered at 32 meV is observed in all cases, which is associated with the translational recoil of the hydrogen molecule.

Figure 4.45 shows the temperature dependence (5, 20, 25 and 35 K) of the INS spectra for different dosings. The INS spectra for 0.03ML (Fig. 4.45-0.03ML) show for all temperatures two peaks centered at 11.1 and 12.9 meV and no change with temperature. At the highest adsorbed amount 1.0ML (Fig. 4.45-1.0ML), the spectra show five peaks at 11.5, 12.2, 13.0, 14.0, 15.3 and 15.5 meV that decrease with increasing temperature. For all dosing steps, the temperature dependence only widens the peaks and decreases the intensity, with all peaks are defined up to 35 K.

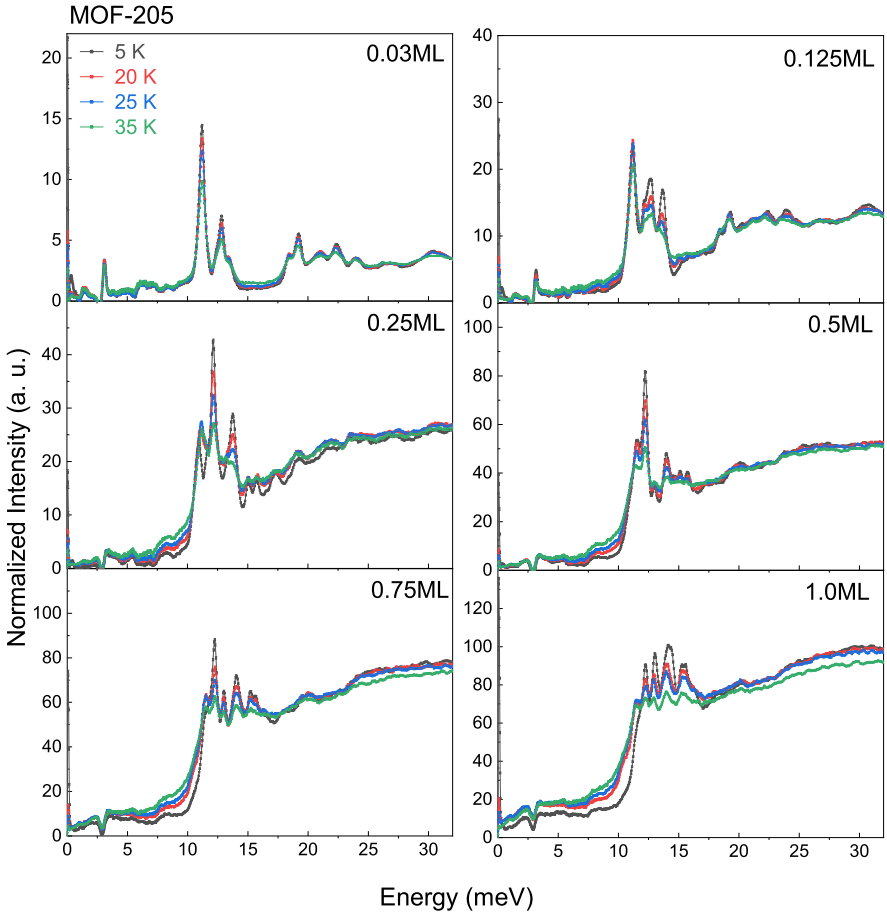

Figure 4.45 *MOF-205 INS spectra for different* pH_2 *dosing and temperature.* The spectra are independent of the temperature (5 - 35 K) at low dosing (0.03ML). At highest dosing (1.0ML) the intensity decreases with temperature.

Discussion

Adsorption at low-pressure

The BET analysis of the adsorption isotherms of MOF-205 yields monolayer capacities very close to each other for Ar (50.0 mmol/g) and H_2 (52.5 mmol/g), indicating that the surface area of MOF-205 is covered by a similar amount of atoms/molecules. Such monolayer capacities are used to calculate the BET areas which yield for H_2 (4477 m^2/g) that is about 5% higher than the area measured by Ar (4277 m^2/g). Both areas are comparable to previously reported BET areas (4400 m^2/g) [101–103].

A previous report by Streepel *et al.* [104] measured the H_2 and N_2 BET area of other MOF, MIL-101, and found similar results with about 10% higher H_2 BET compared to N_2. Duren *et al.* [105] theoretically discussed this difference, explaining as a difference in accessible surface area of a MOF depending on the probe size.

Additionally, the pore volume was obtained from the adsorption isotherms of MOF-205, which yields about ∼25% higher volume for H_2 2.277 cm^3/g compared to Ar 1.804 cm^3/g. This is an indication that hydrogen sees a larger pore volume than argon that is consistent with the larger accessible surface area for H_2.

The molecular cross-sectional of the H_2 adsorbed on MOF-205 at 20.37 K was calculated comparing the BET H_2 monolayer capacity and the BET area obtained by Ar. The H_2 cross-sectional area was calculated using Equation 4.1 to be 13.5 $Å^2$ which correspond to a H_2-H_2 intermolecular distance of 3.95 Å. Assuming that this intermolecular distance is extended in three dimensions the corresponding volumetric density of the H_2 adsorbed phase is ∼76 kg/m^3 (Eq. 4.3). This shows that the average density of the H_2 adsorbed phase on MOF-205 at 20.37 K is, in between the experimental uncertainty, the bulk-liquid density (for H_2 ρ_{lq} = 70.9 kg/m^3). Such observation reveals that in the case of a MOF there is not a high dense 2D phase of hydrogen, observed for flat surfaces (see Table 4.5).

Table 4.5 Comparison of the properties of H_2 adsorbed on different surfaces.

Material	Sample	Cross-sectional area † ($Å^2$)	H_2-H_2 intermolecular distance◇ (Å)	H_2 monolayer density* (kg/m^3)	Monolayer ratio ($n_m(H_2)/n_m(Ar)$)
Silica	KIT-6	7.10	2.9	202	2.0
	Silica-P	7.96	3.0	170	1.8
	Silica-NP	7.14	2.9	200	2.0
Carbon	CMK-3	8.47	3.1	155	1.7
	CarbopackB	8.99	3.2	141	1.6
	SRB-8F	7.88	3.0	173	1.8
MOF	MOF-205	13.5	4.0	76	1.0(1)

†Cross-sectional areas calculated using Ar(87.3 K) and H_2(20.31 K) monolayer capacities;
◇Calculated assuming *hcp* distribution; *Assuming an phase extended in 3D and a *hcp* distribution.

Neutron scattering

MOFs are crystalline materials constructed by metal-oxide clusters, composed of a few atoms, connected by organic linkers resulting in 3D frameworks (Fig. 4.38). The linkers are usually organic molecules with a size in the order of the benzene ring dimensions (d ∼5 Å). Even considering the small size of H_2, the surface of the framework is composed of specific adsorption positions where only a few H_2 molecules can be adsorbed per linker or metal cluster. The adsorption positions on a MOF surface [99, 106] imply that the H_2 molecules are isolated from their neighbors and see a non-continuous surface *i.e.* fragmented surface.

MOFs adsorption sites have been studied using powder neutron diffraction (NPD) with D_2 loaded on the MOF surface, these experiments have shown in all cases well-defined adsorption sites. The first report for MOF-5 by Yildrim *et al.* [107] shows four different adsorption sites, two near the metal center and two near the linker. Recently, Callear *et al.* [108] studied the H_2 adsorption sites for the structure HKUST-1, the occupancies of each adsorption sites are between 1 and 2, indicating that the hydrogen molecules are isolated, or at best, 2 molecules are located near the same site.

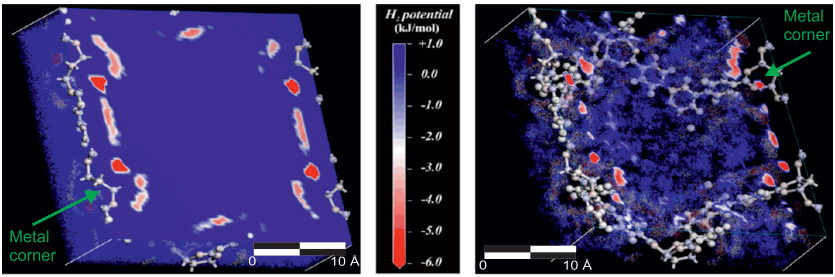

Figure 4.46 *MOF-205 adsorption sites at 50 K.* The distribution of the H_2 adsorption potential calculated by Monte-Carlo simulations; near the metal corners (green arrows) the potential has a value close to 5 kJ/mol. Reprinted (adapted) with permission from H. Lee *et al.* [103]. Copyright 2013 American Chemical Society.

Hydrogen adsorption on MOF-205 has been studied using neutron diffraction by Lee *et al.* [103] showing well-defined Bragg peaks that grow with adsorbed amount indicating that hydrogen is adsorbed in specific positions in the framework. H_2 adsorption on MOF-205 was further investigated by Lee *et al.* [103] using Monte-Carlo simulations to obtain the distribution of the H_2 binding potential at 50 K. Figure 4.46 shows two-color maps that illustrate the adsorption positions at different H_2 dosing. The interaction strength is given by the color indicated in the central bar of the figure. The interaction is stronger near the metal corner $\sim$5 kJ/mol, and several weaker sites are located around the linkers $\sim$3 kJ/mol. This is in agreement with the heat of adsorption (Fig. 4.41) obtained from high-pressure isotherms, which is decreasing from 4.5 to 3.5 kJ/mol with increasing surface coverage.

The state of the hydrogen molecules adsorbed on MOF-205 was studied by *in situ* INS for different dosings and temperatures. The INS spectra (Fig. 4.44) show five peaks close to the free-rotor transition at 14.5 meV, J:1$\rightarrow$0 [57, 58], indicating at least five different adsorption sites. These peaks appear subsequently with increasing dosing indicating that the strong adsorption sites are occupied first,

and then the weaker sites are subsequently filled. This is consistent with the isotherm shape that shows different steps meaning a filling of adsorption sites at different pressure ranges.

The H_2 molecules on these adsorption sites are sufficiently isolated to show rotational transitions close to the energy of the free-rotor. The shifts to higher or lower energies from the free rotor (14.5 meV) are produced by an interaction between the H_2 with the MOF adsorption sites, can be either caused by a hindered rotation or by an elongation of the hydrogen molecule at a strong adsorption site or even a mixture of both.

In a fragmented surface as complex as MOF-205 easily five or more energetic sites are possible, resulting in an adsorption isotherm composed by steps and in a complicated INS spectrum with several peaks. However, for MOFs, the average density of the adsorbed hydrogen is similar to the bulk-liquid at low temperatures. In contrast to flat surfaces showing a high-density 2D layer, this is not observed for fragmented surfaces.

4.3 Summary

Since the 1940s, the adsorption of light-weight gases such as He and H_2 has been studied when experiments revealed very high monolayer capacities at low temperatures close the boiling point. Several explanations have been offered since then, including a high-density monolayer with short intermolecular distances H_2-H_2 or the hypothesis of a bilayer formation.
In a systematic study, the adsorption of hydrogen at low-temperatures ($\sim$20 K) has been investigated on structures with different surface topologies ranging from nearly flat surfaces to fragmented surfaces with the extension of a benzene ring. Several samples of porous silica and carbon were analyzed as examples of a flat surface in comparison to the size of the H_2.
As a model material, the ordered mesoporous silica KIT-6 was examined, which consists of a well-defined 3D network of sole mesopores with a narrow pore size distribution of 10 nm. Porous and non-porous silica nanoparticles were also studied to exclude any influence in the H_2 adsorption by the pore size or reduced pore dimensions. For further comparison, carbon-based materials with different porosities were used. These include the graphitized carbon Carbopack-B as an example of a flat and chemically homogeneous surface, free of functional groups (hydroxyl groups). As a prototype of fragmented surfaces, MOF-205 was chosen from the new class of metal-organic frameworks possessing extremely high surface areas.
A high-resolution gas adsorption apparatus capable of measuring pressures as low as 10^{-8} bar was used to characterize the surfaces at extremely low pressures. The device was couple with a closed-cycle He cryocooler that reaches hydrogen boiling temperatures ($\sim$20 K) with a stability of $\pm$0.05 K. The adsorption of four different gases (Ar, N_2, H_2 and D_2) at their condensation temperature, respectively. It was possible to study the adsorbed phase of H_2 and to determine the layer density of H_2 at 20.37 K by comparing the monolayer capacity of H_2 and D_2 with the specific surface area measured by Ar.

At the high-flux neutron spallation source at the Oak Ridge National Laboratory, the new VISION vibration spectrometer delivers an inelastic count rate that is more than two orders of magnitude greater than comparable instruments available. This allowed for the first time the investigation of the formation of the hydrogen layer *in situ* by inelastic neutron scattering (INS) for different adsorbed amounts and temperatures with unprecedented resolution.

In all the examples studied of flat surfaces (silica and carbon), the H_2 monolayer capacity at condensation temperature (20.37 K) yields almost two times more molecules in the same area, compared the other gases studied (Ar [87.3 K] and N_2 [77.3 K]). The corresponding density of the 2D layer of adsorbed hydrogen is more than two times higher than the bulk solid density of hydrogen (80.0 kg/m^3) equivalent to 200 kg/m^3. Such high densities correspond to short intermolecular distances on the order of 2.9 Å or a molecular cross-sectional area of 7.1 Å^2.

Inelastic neutron scattering experiments for all silica samples show two energy transitions (11 and 14 meV) at the first loading point (0.125ML), which corresponds to 0.125 monolayers. The two rotational peaks at 11 and 14 meV are located close to the free-rotor energy of H_2 (14.5 meV). This indicates that the high-density 2D layer has similar properties to the solid phase of hydrogen (solid-like). Both rotation transitions are explained using the Evett model of a hindered rotor, where hydroxyl groups on the silica surface act as rotational barrier. For a graphitized carbon, the INS spectra show only a peak near 14.5 meV, which is easily explained by the H_2 free-rotor transition in a surface free of hydroxyl groups. Moreover, the H_2 adsorbed on a fragmented surface, *i.e.* MOF-205, shows no highly dense phase and the INS spectra show different adsorption sites which are filled at different pressures.

This combination of adsorption isotherms with the INS spectra shows for the first time a clear indication for the formation of a high-density 2D hydrogen layer on flat surfaces.

The high-density of the 2D layer of adsorbed hydrogen at low-temperature is explained using *ab initio* calculations of the intermolecular interaction H_2-H_2 for a surface attraction ranging from 1 to 10 kJ/mol. For a typical value of the

H_2 adsorption interaction ($\sim$4 kJ/mol for silica), the intermolecular interaction H_2-H_2 is 0.6 kJ/mol that is significantly less than the adsorption interaction. The low intermolecular interaction results in a small intermolecular separation ($\sim$ 2.9 Å), *i.e.* a high-density 2D layer. Such densities are only possible due to the strong compressibility of the H_2 monolayer. Because of the absence of core electrons, it is much easier to compress the first layer of H_2 compared to 2nd row or even heavier elements due to the significantly weaker Pauli repulsion of the electron clouds when overlapping upon compression.
These systematic experiments together with the calculations by the group of Thomas Heine give an explanation to high H_2 monolayer capacity as a high-density phase of adsorbed hydrogen, which have been observed but never fully understood over the past 70 years. High density adsorbed hydrogen could play an interesting role for cryogenic hydrogen storage systems with extremely high storage capacities.

Chapter 5

Hydrogen isotope diffusion in MOFs

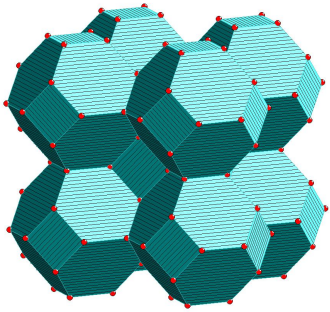

Figure 5.1 *ZIF-8 crystal structure showing a sodalite topology.* ZIF-8 show a structure with cavities with diameter of 11.6 Å interconected by channels with and apperture of 3.4 Å [109].

This Chapter presents a new method to study hydrogen isotope diffusion in porous materials in the low-temperature region (∼20 K). The diffusion of hydrogen at such temperatures in micropores, with a diameter close the kinetic diameter of H_2 and D_2 (2.9 Å), is dominated by kinetic quantum sieving (KQS) that can be used to separate isotopes. As a model system, the metal-organic framework ZIF-8 was studied using two samples with different material configuration, monoliths (ZIF-8-ML) and powder (ZIF-8-PW). The adsorption kinetics is measured simultaneously with the isotherm using a commercial Sieverts'

apparatus. The diffusion coefficients of H_2 and D_2 are obtained analyzing the kinetics of adsorption by Fick's 2nd law (see Chapter 2).

ZIF-8 framework

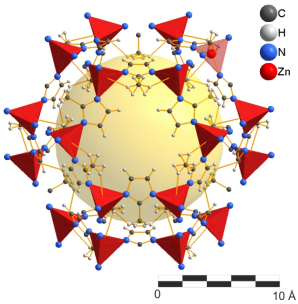

Figure 5.2 *ZIF-8 pore apperture structure.* ZIF-8 possesses cavities with diameter of 11.6 Å with a narrow six-membered-ring opening [109].

Zeolite imidazole frameworks (ZIF) possess topologies with large cages and small apertures [109]. ZIF-8 was first reported by Chen *et al.* [110], it has a sodalite topology (Fig. 5.1) with a chemical formula *Zn(MeIM)$_2$ (MeIM = 2-methyl imidazolate)*, and a high thermal and chemical stability [109, 110]. The ZIF-8 (Fig. 5.2) framework is composed of large cavities (11.6 Å of diameter), interconnected by narrow windows (3.4 Å) making it an ideal candidate for shape- and size- selective separations of a number of small molecules [111, 112].

Oh *et al.* [19] measured H_2 and D_2 isotherms and reported a molar ratio (nD_2/nH_2) of 11 at low pressure ($\sim 1 \cdot 10^{-5}$ bar) and low temperature (19.5 K), indicating that the narrow windows (3.4 Å) of ZIF-8 can even separate hydrogen isotopes. Fairen-Jimenez *et al.* studied the flexible properties of ZIF-8 by nitrogen adsorption [112], XRD experiments [113] and, recently, by INS experiments [114], which show a structural change at cryogenic temperatures ($\sim$77 K) caused by the motion of the imidazolate linker due to gas adsorption.

Two different samples of ZIF-8 were synthesized as powder (ZIF-8-PW) and monoliths (ZIF-8-ML) by the group of Dr. David Fairen-Jimenez from Cambridge University (Fig. 5.3). Figure 5.3 shows photographs of the powder and monolith samples. The powder sample has a particle size between 60 - 70 nm, obtained by TEM. The monolith sample has an average macrostructure with

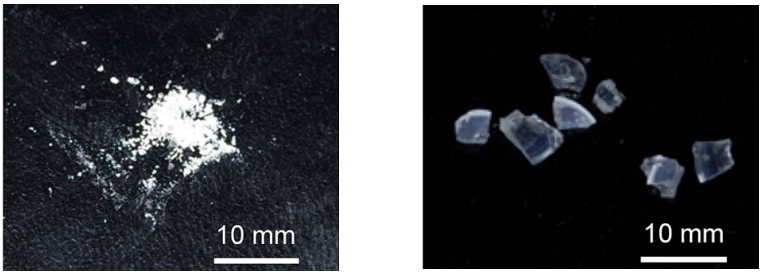

(a) *ZIF-8 Powders.* (b) *ZIF-8 Monoliths.*

Figure 5.3 *Photograph of the ZIF-8 samples synthesized as powder and monoliths* Republished with permission of Royal Society of Chemistry, from T. Tian *et al.* [7] Copyright 2015; permission conveyed through Copyright Clearance Center, Inc.

blocks of ∼3 mm obtained by optical microscopy, showing similar porosity, low light scattering (transparency), high bulk densities and a volumetric surface area three times higher than the conventional powder material (based on the density measured by mercury porosimetry) due to difference in interparticle spaces [7].

Analysis of the adsorption kinetic

H_2 and D_2 adsorption kinetics in ZIF-8 was studied in the vicinity of the boiling point (∼20 K) using a commercially available Sieverts' apparatus *iQ$_2$ Autosorb* (Chapter 2). The device was operated in the *"kinetic mode"* which measures an adsorption isotherm and collects simultaneously the pressure evolution in time for each dosing step of the isotherm.

Figure 5.4a shows a diagram of the experimental device. For each dosing step, a calibrated volume (manifold) is pressurized to a well-defined pressure; then a valve is opened between the manifold and the sample holder allowing the gas flows to the sample (see Chapter 3) while the pressure is continuously recorded as a function of time by a pressure transducer until the equilibrium pressure, p_{eq}, is reached.

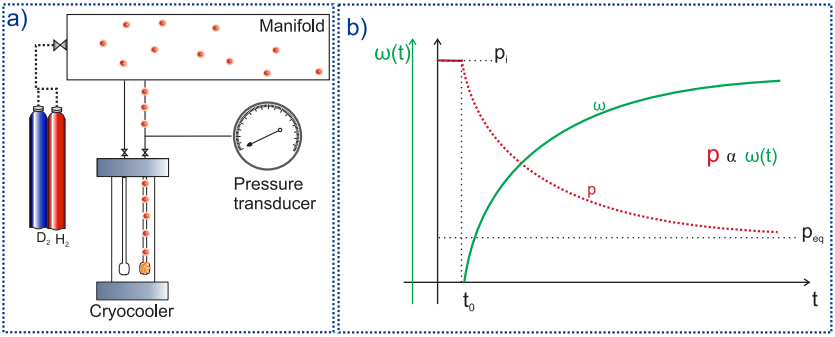

Figure 5.4 *Kinetic curves collected by a volumetric adsorption device.* (a) First, the gas is dosed using a previously calibrated volume (manifold); then a valve between the sample holder and the manifold is open. The pressure P is recorded as function of time t by the pressure transducer. (b) The amount of adsorbed gas ω(t) is proportional to the pressure and is plotted as a function of the time (kinetic curve).

The time dependence of the pressure is called "*kinetic curve*" and is schematized in Figure 5.4b; the gas pressure decreases over time because part of the gas molecules diffuses into the sample. The amount of gas adsorbed by the sample (red curve) is proportional to the gas pressure (green curve), $\omega(t) \propto -p$. For each dosing step (point in the isotherm), the adsorbed amount is normalized to $\hat{\omega}$ by the final adsorbed amount ω_∞ (at equilibrium pressure p_{eq}) using the Equation 5.1.

$$\hat{\omega}(t) = \frac{\omega(t) - \omega_0}{\omega_\infty - \omega_0} \tag{5.1}$$

where $\omega(t)$ is the amount of adsorbed gas as a function of time; ω_0 is the initial amount at t=0 measured in the previous dosing step.
The diffusion of a gas through a porous solid is described by the Fick's laws, discussed in Chapter 2. All kinetic curves (one per point in the isotherm) were fitted using a particular solution of the 2nd Fick's law (Eq. 5.2) which considers as boundary conditions the diffusion of gas into spherically shaped particles in a

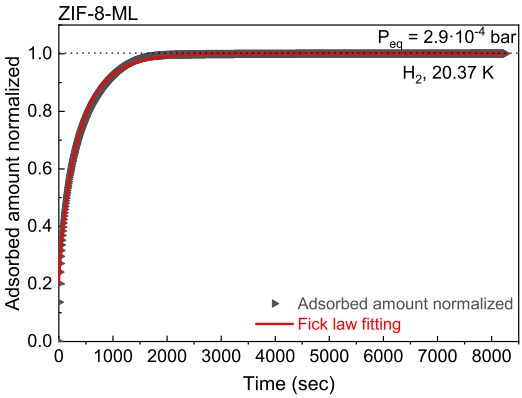

Figure 5.5 *Fitting of the adsorption kinetics using 2nd Fick's law.* The kinetic data of the adsorption is modeled using a solution of 2nd Fick's law that considers a spherical porous particle in container of finite volume.

limited volume[1] homogeneously filled with gas (well-stirred condition, which considers uniform gas concentration outside of the particle), where the radius of the particle is a and the volume of the gas (excluding the space occupied by the sphere) is V [51].

$$\hat{\omega}(t) = \frac{\omega(t) - \omega_0}{\omega_\infty - \omega_0} = 1 - \sum_{n=1}^{\infty} \frac{6\alpha(\alpha+1)}{9 + 9\alpha + q_n^2\alpha^2} \, e^{(-Dq_n^2 t/a^2)} \tag{5.2}$$

where D is the diffusion coefficient, q_n are the non-zero roots of

$$tan\ q_n \ = \ \frac{3q_n}{3 + \alpha q_n^2} \tag{5.3}$$

and α is the ratio between the volumes of solution and sphere ($\alpha = 3V/(4\pi a^3)$) obtained by a He expansion test.

[1] Such assumption considers that concentration of the gas outside of the porous medium is decreased by the diffusion of part of the gas into the spherical particle.

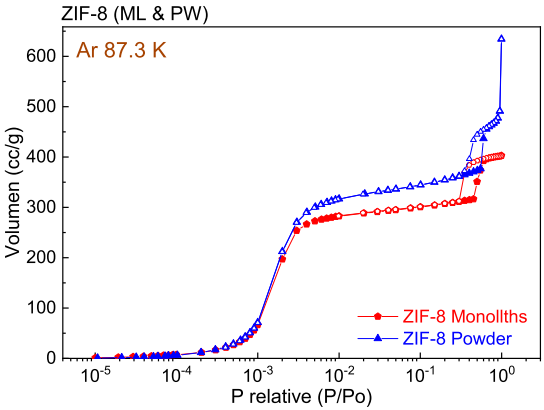

Figure 5.6 *Ar isotherms of the monolith and powder ZIF-8.* The isotherm shows a hysteresis loop at a relative pressure $P/P_0 = 0.4$.

Figure 5.5 shows, as an example, the analysis of the hydrogen kinetic curve at 20.37 K, for the pressure point $P_{eq} = 2.9 \cdot 10^{-4}$ bar. The data points are given in black triangles and the fitting is presented in a red line over the data points. Equation 5.2 is used to fit all kinetic curves to obtain the diffusion coefficient D, which is independent of the particle dimensions and is given in units of [m^2/s]. The diffusion coefficient can only be calculated for a sample with a narrow particle size distribution, thus the kinetic coefficient $D^* = D/a^2$ is often found in literature [115] which has units of [1/s] and is dependent on the particle dimension.

5.1 ZIF-8 surface characterization

To determine the BET area of the two samples Ar adsorption experiments were carried out at 87.3 K (Fig. 5.6). The Ar isotherms show a step at the relative pressure 0.001 P/P_0 and a hysteresis loop in the range 0.3 - 0.65 P/P_0. The Ar BET areas of ZIF-8-PW and ZIF-8-ML were obtained using the relative pressure

range (0.003 - 0.03) according to the recommendations of Rouquerol *et al.* [42] (see Chapter 2), yielding 1231 and 1084 m^2/g, respectively, in agreement with previous reports [7].
The isotherms of both samples show a step located at 0.001 P/P_0 for Ar and a similar hysteresis loop which is an indication that both samples have the same pore structure with a small difference in specific surface area. The pore volume was calculated using the Ar isotherms and the Gurvich rule at 0.95 P/P_0, ZIF-8-ML yields 0.506 cm^3/g , while in the case of ZIF-8-PW the pore volume is 0.620 cm^3/g.

5.2 H_2 and D_2 adsorption and diffusion

5.2.1 Adsorption isotherms

Figure 5.7 shows the H_2 and D_2 adsorption isotherms of ZIF-8-ML and ZIF-8-PW at 20.37, 30, 40, 50 and 60 K. The isotherms show in all cases a type-I shape associated with micropores (see Chapter 2) and the amount of adsorbed gas decreases with increasing temperature. At 0.97 bar and 20.37 K, the H_2 isotherm of ZIF-8-ML has a maximum uptake of 17.9 mmol/g (saturation). Under the assumption of a perfect crystalline ZIF-8 structure, 1 g contains $2{\cdot}10^{20}$ cavities (cages), and 17.9 mmol/g is equivalent to 50 molecules per cage; while ZIF-8-PW has 24.4 mmol/g corresponding to 64 molecules per cage.

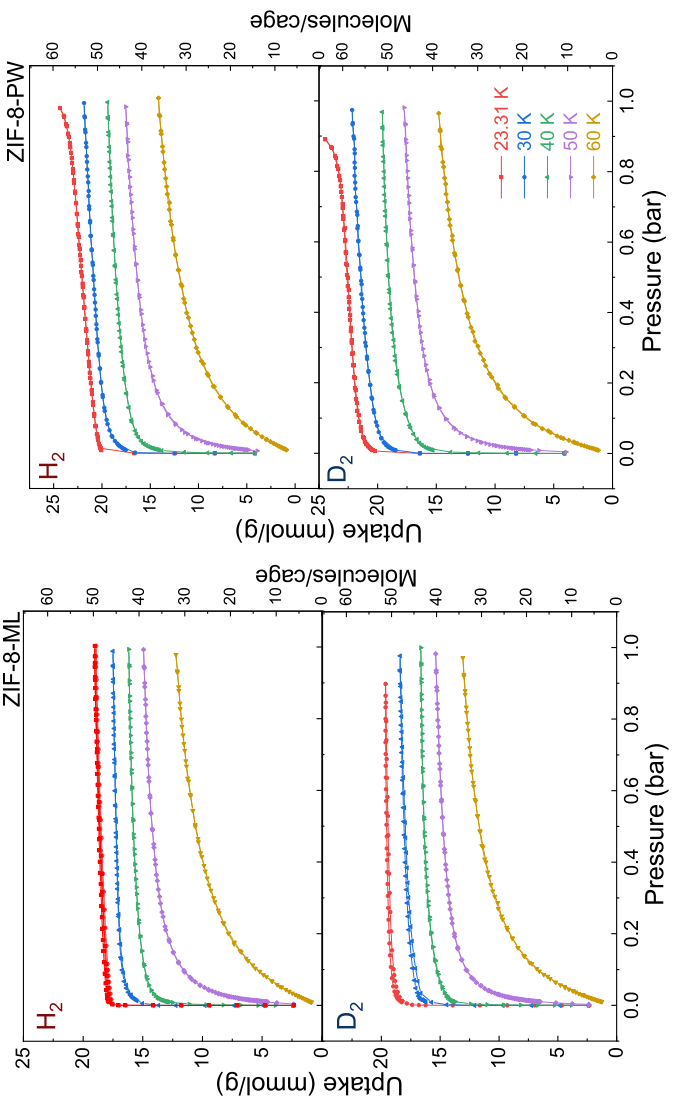

(a) *ZIF-8-ML isotherms.*

(b) *ZIF-8-PW isotherms.*

Figure 5.7 *H_2 and D_2 adsorption isotherms of monoliths and powders ZIF-8.* In all cases, the isotherm show a type-I shape associated with micropores.

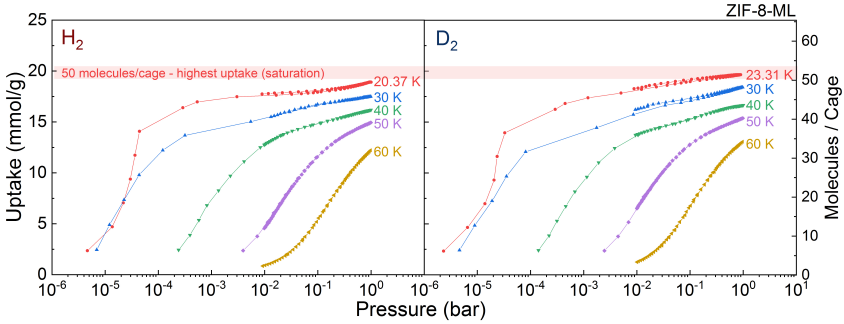

Figure 5.8 *H_2 and D_2 adsorption isotherms of ZIF-8-ML in semi-log scale.* For both gases, the low-pressure points of the isotherms collected at the condensation temperature respectively are close to the isotherm at 30 K. The maximum uptake of the H_2 isotherm (saturation) is 47 molecules/cage.

The low-pressure region of the isotherms is shown by the semi-log plot (Fig. 5.8), in the range (10^{-6} - 10^{-4} bar), the H_2 and D_2 isotherms collected at their respective condensation temperature (∼20 K) are close to the 30 K isotherms, suggesting a poor equilibrium at low-pressure. However, an increase in the time to reach equilibrium (from 16 to 60 hrs per isotherm) does not result in a higher uptake, yielding the highest uptake (∼50 molecules/cage) at pressures close to saturation (0.97 bar). At higher temperature (T $\geqslant$ 30 K), the isotherms are completely separated from each other for all pressures (0 -1 bar).

Figure 5.9 shows H_2 and D_2 isosteric heat of adsorption as a function of coverage for both, monoliths and powders; calculated using the isotherms (30, 40, 50 and 60 K) and the Clausius-Clapeyron equation (see Chapter 2). The H_2 and D_2 heat of adsorption of both, monolith and powder, as a function of coverage remains constant (∼4 kJ/mol) up to half of the total coverage (∼30 molecules/cage or ∼13 mmol/g) and then it decreases with coverage.

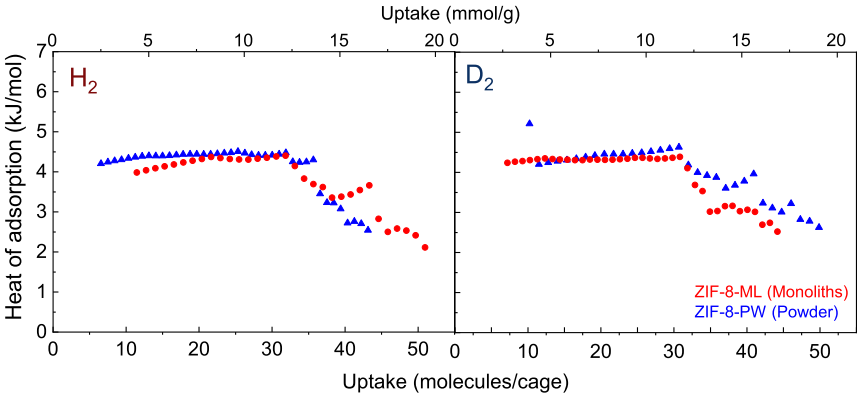

Figure 5.9 *H_2 and D_2 heat of adsorption of ZIF-8-ML and ZIF-8-PW.* The isosteric heat of adsorption was calculated using the isotherms at 30, 40, 50 and 60 K and the Clausius-Clapeyron equation. In all cases, the heat of adsorption remains constant ($\sim$ 4 kJ/mol) up to half of the total uptake.

Table 5.1 Isotherm surface analysis of ZIF-8: monolayer capacity, BET area, pore volume, and average heat of adsorption.

			BET		Gurvich	Isosteric
	Gas	Temperature (K)	Monolayer capacity (mmol/g)	BET area (m^2/g)	Pore volume (cm^3/g)	Heat of adsorption (kJ/mol)
ZIF-8-ML	Ar	87.3	12.7$^{\diamond}$	1084†	0.50	–
	N_2	77.36	13.9$^{\diamond}$	1357†	0.50	–
	H_2	20.37	–	–	0.53	4.4*
	D_2	23.31	–	–	0.47	4.2*
ZIF-8-PW	Ar	87.3	14.4$^{\diamond}$	1231†	0.62	–
	N_2	77.36	14.1$^{\diamond}$	1372†	0.63	–
	H_2	20.37	–	–	0.73	4.2*
	D_2	23.31	–	–	0.61	4.4*

$^{\diamond}$The BET range correspond to 0.003 - 0.03 P/P_0 obtained using the Rouquerol recommendation for micropores; †The specific surface area was calculated using the cross-sectional area Ar (14.2 Å^2) and N_2 (16.2 Å^2) assuming a bulk liquid density; *Average isosteric heat of adsorption calculated using values obtained only up to 0.5 of the total coverage.

5.2.2 Adsorption kinetics

Powder vs Monoliths kinetics

Figure 5.10 shows as an example a direct comparison of the kinetic curves of the monolith (ZIF-8-ML) and powder (ZIF-8-PW) samples for deuterium at the same temperature (23.31 K) and same relative pressure (0.015 P/P_0). The equilibrium time for the monoliths is 8.6 hrs while for the powder sample, the total time necessary to achieve equilibrium is in the order of a few seconds with most of the gas (90%) adsorbed in the first seconds (20 s) of the experiment.
The device was set to collect a pressure point every 3 seconds. For a quantitative analysis of the adsorption kinetics applying 2nd Fick's law, several well-resolved points are required during the maximum uptake rate. In the case of powders at all dosings and temperatures, the maximum uptake occurs during the first 30 seconds owing to the short diffusion distance into the small particles ($\sim$70 nm). Therefore, the diffusion coefficient cannot be analyzed for the powder sample or low uptakes (n < 20 molecules/cage) in the monolith. At higher uptakes, the monolith sample ZIF-8-ML shows a time of equilibration in the order of hours caused by the larger particle size of $\sim$3 mm that implies longer diffusion distances. Because the gas molecules in the pores have a longer distance to diffuse, the time to reach equilibrium is longer, allowing the analysis of the kinetic curves and diffusion coefficients.
In general, this method can be used to measured kinetic curves that reach equilibrium in at least 30 s owing the time resolution of the device (3 s), which set an experimental upper limit for the kinetic coefficient to D^*_{max} = 0.03 1/s. Typically, the diffusion coefficient of H_2 in a microporous material is in the range of ($10^{-7} < D < 10^{-9}$ m^2/s) [24, 116]. Assuming a diffusivity of 10^{-7} m^2/s, the time resolution may imply that only materials with a minimum particle size of $\sim$0.001 m can be measured.
The kinetic curves of the points close to saturation, which correspond to pressures higher than 0.1 bar, show large fluctuations in the adsorbed amount indicating a

large sensitivity to temperature fluctuations. At higher pressures, the isotherms are saturated after which only a small amount of gas is adsorbed (Fig. 5.7) Therefore, for all kinetic curves collected at higher pressures (p > 0.1 bar) close to saturation, only a small change in adsorbed amount is recorded, which reduces the resolution of the kinetic curve measurement. Hence, the measurement of the diffusion is limited by the change in the adsorbed amount per point in the isotherm, and the kinetic curves can only be measured in the pressure points where most of the adsorption occurs (in the case of ZIF-8-ML is 10^{-5} - 10^{-3} bar).

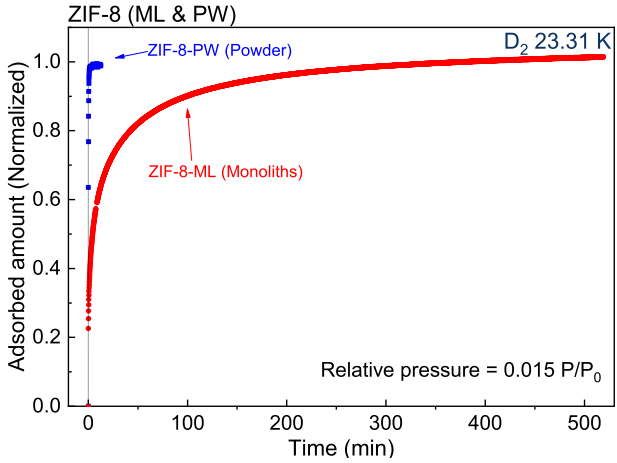

Figure 5.10 *Monoliths and powder ZIF-8 kinetic data comparison.* The kinetic data correspond to deuterium at 23.31 K at the relative pressure 0.015 P/P_0.

Kinetics analysis of monoliths

Figure 5.11 shows the H_2 kinetic curves of ZIF-8-ML (Monoliths) at 20.37 K for every dosing step in the isotherm up to 50 molecules/cage. All the kinetic curves are included in Appendix B.

In the first kinetic curves (n < 20 molecules/cage), the time to reach equilibrium is in the order of a few seconds with 90% of the gas adsorbed at the respective point is adsorbed in the first 20 s. At higher dosing (n > 20 molecules/cage), the kinetic curves in (Fig. 5.11) show longer equilibrium times in several minutes or hours.

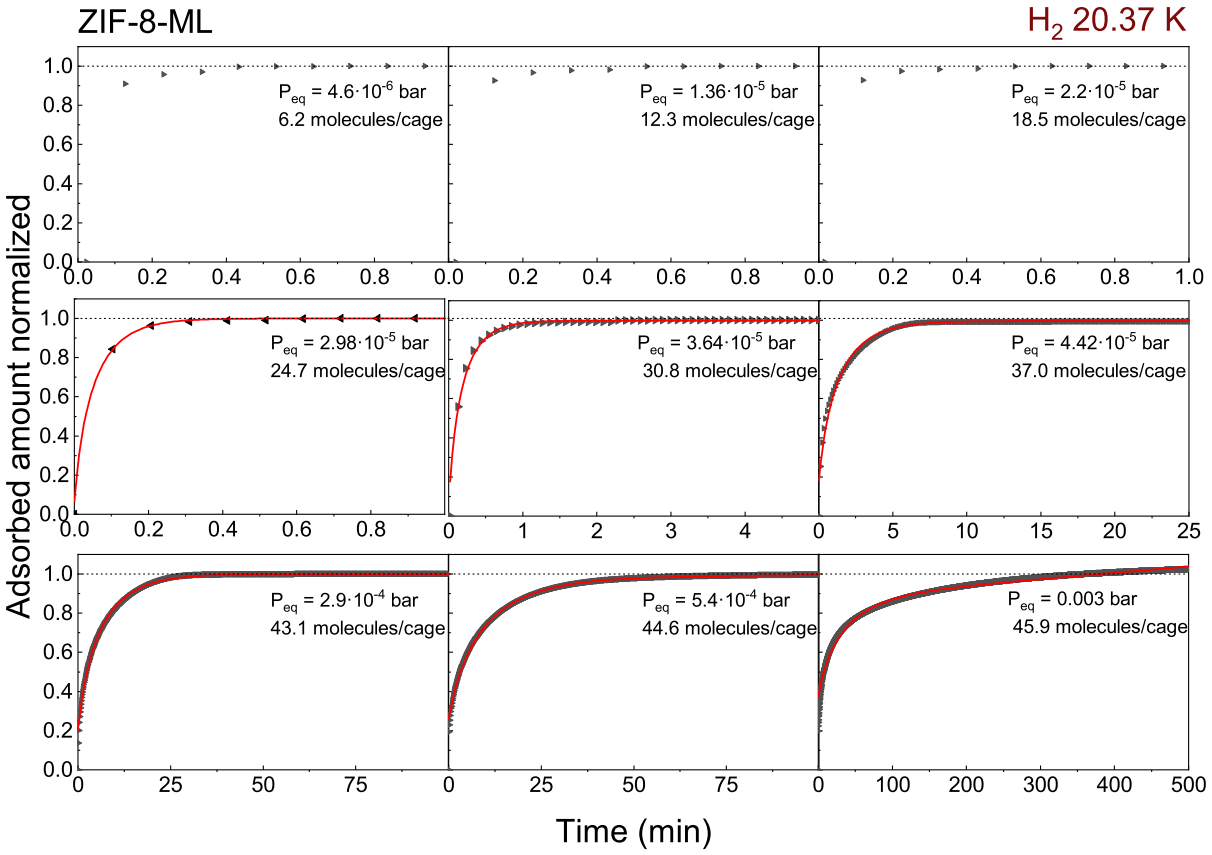

Figure 5.11 *H_2 kinetic data of ZIF-8-ML at 20 K.* The kinetic data (black triangles) at the respective isotherm point was fitted using the 2nd Fick's law (red line).

Firstly, the kinetics is analyzed by taking the time required to reach 90% of the equilibrium uptake at the respective pressure point ($t_{90\%}$). Figure 5.12 shows this time $t_{90\%}$ for each dosing point comparing H_2 and D_2 at different temperature. The kinetics of uptake, strongly depends on the temperature getting much slower with decreasing temperature. This can be seen on the time scale in Figure 5.12 which is getting longer from 40 to 30 K and from 30 to 20 K, each time by and order of magnitude.
At 40 K, the kinetics between 10 and 40 molecules/cage is very similar for H_2 and D_2, with H_2 slightly faster. At 30 K, the cages are filled much faster for H_2 than for D_2; at 25 molecules/cage, the time to reach 90% is about 90 s longer for D_2. However, near the maximum uptake ($\sim$45 molecules/cage), H_2 and D_2 behave similar. At boiling temperature, H_2 and D_2 shows a similar equilibration time up to 30 molecules/cage, but for higher filling of the cages, H_2 diffuses much slower than D_2.

Diffusion coefficients analysis

H_2 and D_2 kinetic curves of ZIF-8-ML were analyzed using the Fick's 2nd law (Eq. 5.2) for filings of the cage from 20 to 50 molecules/cage that show equilibrium times in the order of minutes ($t_{90\%} > 20$s). Figure 5.11(red line) shows the fitting curves for model of 2nd Fick's law (Equation 5.2). All corresponding fitting are also included in Appendix B.
The kinetic coefficient D^* obtained from the kinetic curve fitting (Fig. 5.5) can be directly converted to the diffusion coefficient D, which is given by relation $D^* = D/a^2$, using average particle size of the monoliths, a, is $3{\cdot}10^{-3}$ m, obtained by optical microscopy.
Figure 5.13 shows the H_2 kinetic coefficient D^* (left axis) and diffusion coefficient D (right axis) as function of the uptake, at the temperatures 40, 30 and 20.37 K. At fillings close to 25 molecules/cage, the H_2 diffusion coefficients D_{H_2} for the three temperatures have a similar value $5{\cdot}10^{-7}$ m^2/s and then they decrease with increasing uptake.

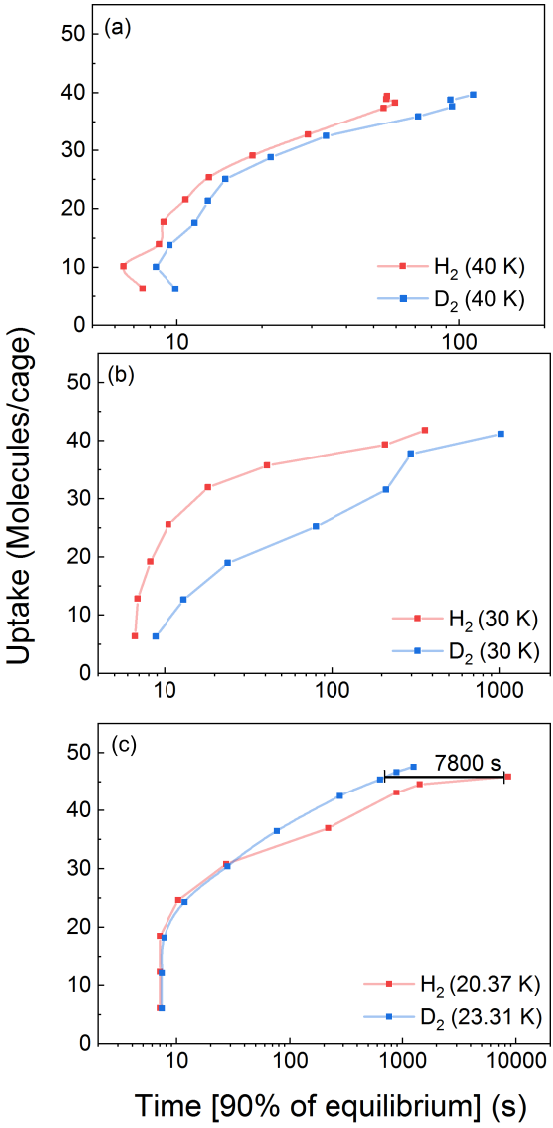

Figure 5.12 *H_2 and D_2 adsorbed amount as function of the equilibrium time.* The adsorbed amount is show as function of the time that the kinetic curve requires to reach 90% of equilibrium ($t_{90\%}$).

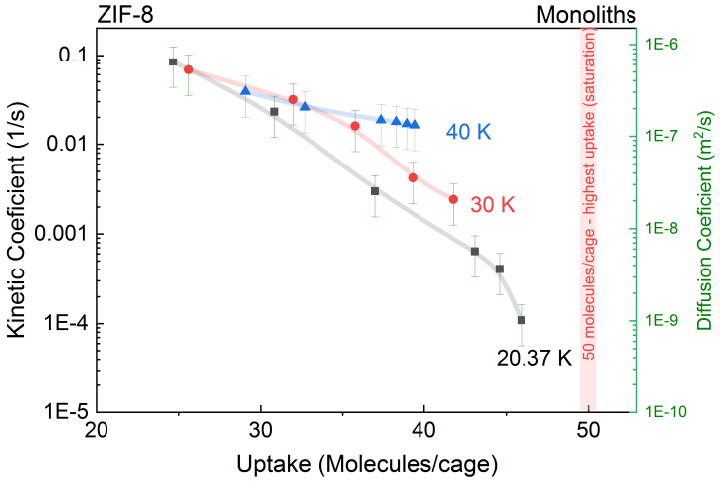

Figure 5.13 *Hydrogen kinetic and diffusion coefficient for the temperatures 20, 30 and 40 K.* The kinetic (left scale) and diffusion (right scale) coefficients decrease with increasing gas uptake.

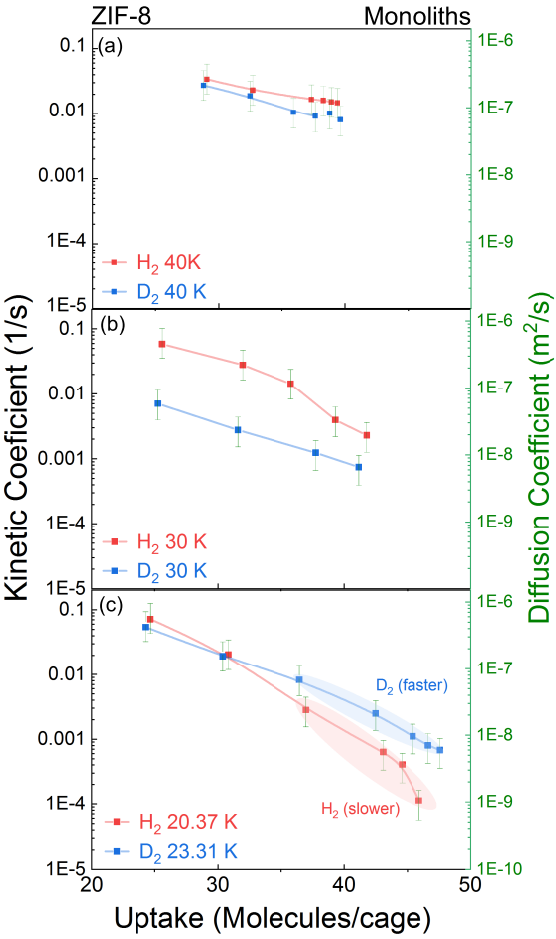

Figure 5.14 *H_2 and D_2 kinetic and diffusion coefficient for the temperatures (a) 20, (b) 30 and (c) 40 K.* The D_2 diffusion coefficient for high uptakes at 20 K is higher than H_2 that clearly show faster diffusivity for the heavier isotope.

Figure 5.14 (right axis) shows the comparison of the hydrogen D_{H_2} and deuterium D_{D_2} diffusion coefficients for different temperatures. For all temperatures, the kinetic D^* and diffusion D coefficient decreases as a function of the adsorbed amount.
The diffusion coefficients at 40 K decrease also with increasing uptake with D_{D_2} close below D_{H_2} for all dosing points.
At 30 K, D_2 diffusion coefficient decreases faster than H_2, starting at low uptakes. In consequence, close to 25 molecules/cage D_{D_2} is $6{\cdot}10^{-8}$ m^2/s below D_{H_2}, $6{\cdot}10^{-7}$. At 35 molecules/cage, the H_2 coefficient also decreases reaching values close above D_2. The faster decrease of D_2 is observable in Figure 5.12b where both gases show similar fast equilibration at low uptakes.
Figure 5.14c, show the comparison at the respective condensation temperature of H_2 and D_2. The diffusion coefficients are close to $1{\cdot}10^{-7}$ m^2/s at fillings below 30 molecules/cage. At higher uptakes, both diffusion coefficients decrease and D_{D_2} is higher than D_{H_2}. Close to saturation of the isotherm ($\sim$50 molecules/cage), D_{D_2} is $\sim 1{\cdot}10^{-8}$ m^2/s and D_{H_2} is $\sim 1{\cdot}10^{-9}$ m^2/s.

Discussion

H_2 and D_2 adsorption

The H_2 and D_2 isotherms show a "slightly" higher uptake for powder compared to monoliths. The BET area obtained for the powder sample (1084 m^2/g) by adsorption experiments is higher than for monolith (1357 m^2/g) which is a result of the different particle size and yields a "slightly" higher gas capacity of the powder sample. The heat of adsorption (Fig. 5.9) have a value close to 4 kJ/mol for both samples, which remains constant up to half of the total uptake ($\sim$ 30 molecules/cage) and then decreases. The isotherms of both samples show identical steps at the same pressure, a similar uptake and the same heat of adsorption indicating a similar pore structure for both monolith and powder samples.

ZIF-8 framework flexibility and pore aperture

The H_2 and D_2 diffusion coefficient of ZIF-8-ML for all temperatures decrease with the uptake (Fig. 5.13), which indicates that the diffusivity is reduced due to the presence of adsorbed molecules on the framework. The change in diffusivity of H_2 and D_2 can be explained by the change in the pore channel aperture. This modification in the aperture is induced by gas adsorption in the pores of ZIF-8.

Previous N_2 adsorption experiments have shown that the ZIF-8 structure has flexible behavior [113] which has been observed also for other gases such as CH_4 and CO_2 [112]. The ZIF-8 structure changes the shape and size of the pore aperture modifying the accessible surface area.
Ar adsorption modifies the structure of ZIF-8, observed in the hysteresis loop of the isotherm (Fig. 5.6). The hysteresis loop indicate that the structure has a defined transition that modifies the accessible surface area at a certain concentration of Ar. In the case of H_2 and D_2, adsorption induces changes in the pore aperture of ZIF-8 decreasing the transport of gas through the pore channels.

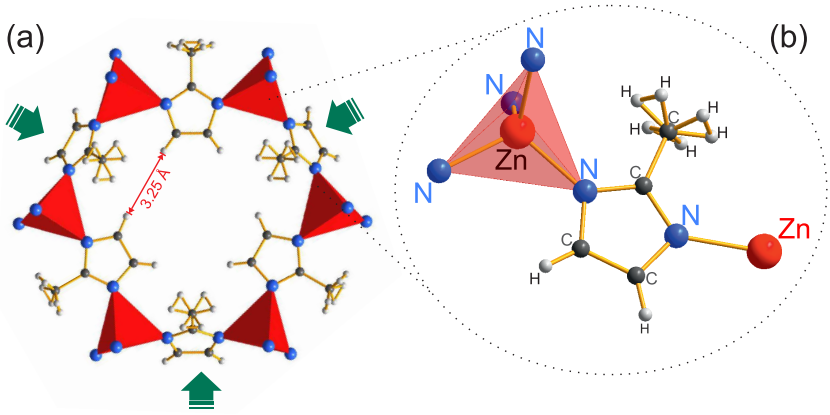

Figure 5.15 *ZIF-8 pore aperture and linker.* (a) The green arrows show the linkers that swing in the direction of the pore aperture upon gas adsorption. (b) ZIF-8 imidazolate linker connected to two Zn atoms.

Recently, M. Casco *et al.* [114] studied the flexibility of ZIF-8 under N_2 adsorption using neutron vibrational spectroscopy and demonstrated experimentally that the gas-induced flexibility. Figure 5.15a shows the pore aperture of the empty structure ZIF-8. The imidazolate linkers (Fig. 5.15b) are pushed to the outside of the pore with increasing gas uptake. The motion of the imidazolate linker, or *"swing"*, rotates the linker towards the pore aperture, effectively reducing it. Three of the six linkers close to the aperture are responsible for the reduction in pore aperture (marked with green arrows in Fig. 5.15).

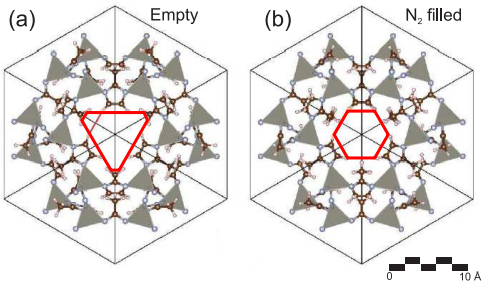

Figure 5.16 *Pore aperture change of ZIF-8 by N_2 adsorption.* Reprinted from M. Casco *et al.* [114] - Published by The Royal Society of Chemistry. *Licensed under a Creative Commons Attribution-NonCommercial 3.0 Unported Licence (CC BY-NC 3.0)*

Figure 5.16 shows the structural change of the ZIF-8 framework upon N_2 adsorption obtained by M. Casco *et al.* [114]. Figures 5.16a and 5.16b show the pore aperture of the empty cage and the one loaded with N_2, respectively. The dimension of the aperture was highlighted with a triangle for the empty structure (Fig. 5.16a) and a hexagon after N_2 loading (Fig. 5.16b) to show that the linker swings to the direction of the pore aperture upon gas adsorption, effectively reducing the size of the aperture. This reduction of the pore aperture is responsible for the decreasing H_2 and D_2 diffusivities with increasing uptake (Fig. 5.14).

Pantatosaki *et al.* [116] also studied the diffusion of hydrogen in the framework ZIF-8 using quasi-elastic neutron scattering (QENS) and molecular dynamics simulations. Figure 5.17 shows the hydrogen self-diffusion coefficient measured by QENS at 77 K (Fig.5.17-black circles) decreasing as a function of the uptake with values in the range of $1{\cdot}10^{-7}$ - $5{\cdot}10^{-8}$ m^2/s, which is close to the values obtained here (Fig. 5.13).

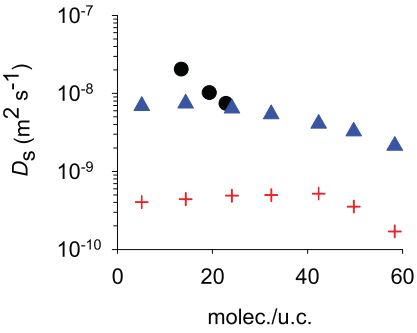

Figure 5.17 *Reproduction of the ZIF-8 hydrogen diffusion coefficient by QENS.* The diffusion coefficients at 77 K were obtained by QENS (black circles), and by molecular dynamics simulations assuming a flexible (blue triangles) and a rigid (red crosses) framework model. Reprinted from Pantatosaki *et al.* [116], with the permission of AIP Publishing.

Molecular dynamics simulations by Pantatosaki *et al.* [116] were used to compute the diffusion coefficients of hydrogen for different degrees of mobility of the imidazolate linker. The simulation for a quasi-free rotation of the imidazolate linker of the ZIF-8 (Fig. 5.17- blue triangles) results in diffusivities approaching the experimental data. Indicating that the mobility of the imidazolate linker plays a fundamental role in the diffusion of hydrogen.

Hence, the swing of the imidazolate linker of ZIF-8 upon gas adsorption effectively reduces the size of the pore aperture, which then reduces the transport of molecules through the pore channels explaining the decreasing H_2 and D_2 diffusivities with increasing uptake shown in Figure 5.14.
At 40 K, both gases are above the critical point (see phase diagram, Fig. 2.3) and behave as (supercritical) gas. In this case, the diffusion coefficients of H_2 and D_2 are very similar with H_2 slightly higher. Both decrease with increasing filing of the cages.

At 30 K, the diffusion of D_2 is much slower than for H_2. However, for higher filling close to 40 molecules/cage, they approach to each other. The condensation pressure of D_2 at 30 K is 4.76 bar whereas for H_2 is almost double 8.04 bar. Furthermore, the critical points for D_2 and H_2 are 38.3 and 33.2 K, respectively. Hence, the difference in the flexible behavior of the framework at 30 K for H_2 and D_2 is a product of complex interaction of the gases with the pore framework. This difference in diffusivities may originate from a stronger interaction of the heavier D_2 with the framework, especially with the imidazolate linkers, leading to more rigid and effectively smaller aperture of the pore for D_2.
In comparison, at the respective condensation temperature, both gases have the similar thermodynamical properties with a pressure of condensation of 1 bar in both cases, resulting in a similar flexible behavior an allowing a more direct comparison of the coefficients. In this case, H_2 decreases faster and the tendencies are crossing, resulting in a much slower diffusion of H_2 coefficient at higher uptakes.

Hydrogen isotope separation

Figure 5.18 shows the comparison of the hydrogen (D_{H_2}) and deuterium (D_{D_2}) diffusion coefficient at their condensation temperature, respectively. The diffusion coefficient decreases with increasing uptake (n > 30 molecules/cage). At the highest uptake (∼50 molecules/cage), deuterium diffuses approximately 10 times faster ($D_{D_2} \approx 1{\cdot}10^{-8}$ m^2/s) compared to the hydrogen molecules ($D_{H_2} \approx 1{\cdot}10^{-9}$ m^2/s). At such uptakes, the swing of the imidazole linker of ZIF-8 towards the pore aperture effectively reduces the size of the pore aperture that reduces the molecular transport through the pore channel, decreasing the diffusivities of both H_2 and D_2. The smaller pore aperture is closer then to the kinetic diameter of H_2 and D_2 (∼2.9 Å) enhancing the kinetic quantum sieving producing higher diffusivities for D_2 (heavier molecule) compared to H_2 (lighter molecule).

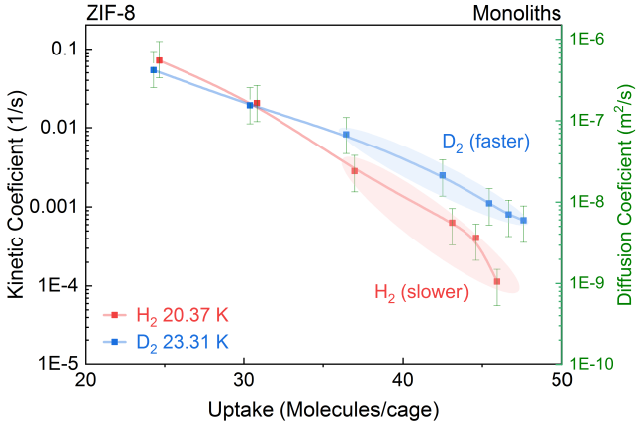

Figure 5.18 *H_2 and D_2 diffusion coefficients at condensation temperature.* The kinetic (left scale) and diffusion (right scale) coefficients decreases with the adsorbed amount. D_{D_2} is ten times larger than D_{H_2} at the highest uptake (∼50 molecules/cage).

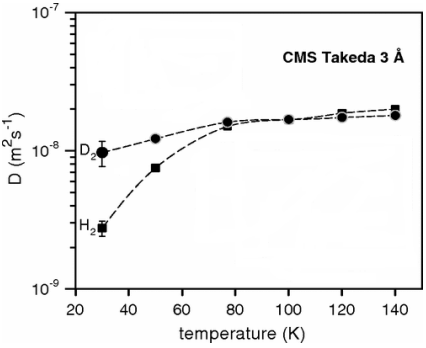

Figure 5.19 *H_2 and D_2 diffusion coefficient of Takeda 3A.* D_2 diffuses faster than H_2 at 30 and 50 K. Image reproduced from Nguyen *et al.* [24]. Copyright (2010) by The American Physical Society.

Very few measurements of H_2 isotope diffusion are reported in the literature, Nguyen *et al.* [24] determined the self-diffusion coefficients of H_2 and D_2 in the microporous carbon Takeda 3A by quasi-elastic neutron scattering. Takeda 3A possesses ink-bottle shaped pores with apertures of about 3Å.

Figure 5.19 shows the diffusion coefficients of H_2 and D_2 as function of temperature obtained for the loading 0.5 mmol/g by QENS. At 30 K, the D_2 diffusivity is close to $1{\cdot}10^{-8}$ m^2/s while H_2 diffusivity is $3{\cdot}10^{-9}$ m^2/s. D_2 has a higher diffusivity at the tempe-

ratures 30, 50 and 77 K which is an indication of kinetic quantum sieving due to the narrow aperture size (3Å) of Takeda 3A. In comparison, the diffusivities obtained here using the framework ZIF-8-ML (with a pore aperture close to 3.4 Å) at condensation temperature ($D_{D_2} \approx 1{\cdot}10^{-8}$ m^2/s, $D_{H_2} \approx 1{\cdot}10^{-9}$ m^2/s) are in the same order of magnitude as for Takeda 3A at 30 K.

At 30 K, H_2 diffusion coefficient is larger than D_2, resulting in the opposite behavior with H_2 diffusing faster than D_2. However, the large difference in diffusivities is attribute to the flexible response of the material at 30 K, since both H_2 and D_2 have different condensation temperatures. In a competitive experiment at 30 K (using mixture D_2/H_2), the flexibility would allow both gases to diffuse simultaneously, yielding no separation effect.

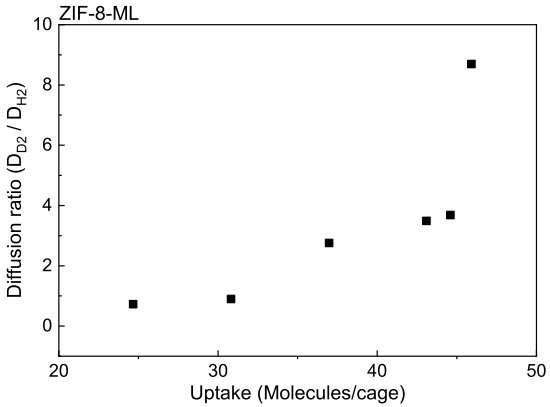

Figure 5.20 *Diffusion ratio of hydrogen isotopes in ZIF-8 at 20 K.* The $S_{diff} = D_{D_2}/D_{H_2}$ diffusion ratio increases with the amount of gas adsorbed as a result of the change in the pore aperture size.

The selectivity of a material is directly related to the diffusion ratio (S_{diff}), defined as $S_{diff} = D_{D_2}/D_{H_2}$ where D_i are the diffusivities of the gas species, respectively [117]. Figure 5.20 shows that the D_2/H_2 diffusion ratio of ZIF-8-ML at condensation temperature increases as function of the adsorbed amount. The diffusivities (Fig. 5.14) decreases with the adsorbed amount but the diffusion

selectivity is increased due to kinetic quantum sieving. The resultant diffusion ratio of ZIF-8 are as high as 10, at concentrations close to the saturation ($\sim$50 molecules/cage).

5.3 Summary

Here, hydrogen isotope diffusion in porous materials at low temperatures is studied using a novel method based on adsorption experiments. The method presents advantages in terms of simplicity compared to other methods to study gas diffusion such as neutron scattering that requires large experimental setups. The framework ZIF-8 is a model material to study hydrogen storage and diffusion because of its relatively large surface area ($\sim$1200 m^2/g) and narrow pore aperture (3.4 Å) close to the kinetic diameter of H_2 (2.9 Å). Recent advances in the synthesis of metal-organic frameworks by the group of D. Fairen-Jimenez at Cambridge University have allowed the synthesis of the framework ZIF-8 as a monolith with macroscopic dimensions.

The diffusion of H_2 and D_2 in ZIF-8 at low-temperature was investigated using two samples with different particle size; monoliths ($\sim$3 mm) and powders (60 - 70 nm). The surface area of both samples was characterized using Ar adsorption experiments showing that both samples (monoliths and powders) possess a similar surface area and pore structure.

A high-resolution adsorption apparatus, capable to measure pressures as low as $1{\cdot}10^{-8}$ bar, was used to collect H_2 and D_2 adsorption isotherms. The temperature was controlled with a closed-cycle He cryocooler that reaches hydrogen boiling temperatures ($\sim$20 K) providing high stability $\pm$0.05 K. Simultaneously, the adsorption kinetics was measured for every point in the isotherms. A model based on Fick's second law with boundary conditions for spherical porous particles was used to analyze the adsorption kinetics, and thus calculate the diffusion coefficients.

The measurement of the adsorption kinetics is limited by the time resolution and temperature stability of the adsorption apparatus. The small particle size

(∼60 nm) of the powder sample yields fast adsorption kinetics (in the order of seconds). Consequently, the use of this method had to rely on particles of macroscopic size *i.e* monoliths, which in combination with low temperatures (∼20 K) yield hydrogen diffusion times in the order of hours per dosing point.
The H_2 and D_2 diffusion coefficients of the monoliths decrease with increasing gas uptake. Such reduction, in the molecular transport, is rationalized in terms of a structural transformation of the material upon gas adsorption. The imidazolate linker of ZIF-8 swings towards the direction of the pore aperture effectively reducing the size, which is consistent with the Ar adsorption experiments and know from the literature.
A higher D_2 diffusion coefficient compared to H_2 is observed at high uptakes and condensation temperature (∼20 K). This indicates that the reduced pore aperture not only limits the molecular transport but also enhances the kinetic quantum sieving, resulting in faster transport of the heavier isotope (D_2).
The presented method uses a commercially available adsorption apparatus to measure the low-temperature adsorption isotherms of H_2/D_2, and simultaneously calculate the H_2/D_2 diffusivities as a function of temperature and gas uptake. Establishing that gas adsorption experiments can be used to study hydrogen diffusion and isotope separation at temperatures close to condensation.

Conclusions

High-density adsorbed hydrogen

In a systematic study, the adsorption of hydrogen at low-temperatures ($\sim$20 K) was investigated using high-resolution adsorption isotherms and *in situ* inelastic neutron scattering. Several structures with different surface topologies ranging from nearly flat surfaces to fragmented surfaces with the extension of a benzene ring were investigated. Porous silica and carbon were analyzed as examples of a flat surface in comparison to the size of the H_2. As a prototype of fragmented surfaces, MOF-205 was chosen from the new class of metal-organic frameworks possessing extremely high surface areas.

Hydrogen adsorption at low-temperature on flat surfaces

- Mesoporous silica and carbon samples with pore diameters in the order of a few nanometers, which are examples of flat surfaces compared to the size of H_2 molecule, show twice as high H_2 monolayer capacity compared to the Ar or N_2 at their condensation temperature, respectively.

- The analysis of the isotherms of silicas and carbons indicates that the H_2 molecules in first adsorbed layer at 20.37 K has a small molecular cross-sectional of $\sim$7 - 8 $Å^2$, which is equivalent to high density layer. In mesoporous silica KIT-6 this H_2 layer density is equivalent to 201 kg/m^3,

which is more than two times higher than the bulk-solid density (80.0 kg/m^3).

- A high-resolution H_2 adsorption isotherm was obtained at 20.37 K for the graphitized porous carbon (Carbopack-B) showing for the first time H_2 layering transition. Layering transitions are only observed for chemically homogeneous surfaces at sub-critical temperatures, which indicates that Carbopack B has a surface free of functional groups.

- The high-flux neutron spallation source at Oak Ridge National Laboratory and the new vibrational spectrometer VISION, allow for the first time to study the formation of an adsorbed hydrogen layer *in situ* by inelastic neutron scattering (INS) with an unprecedented resolution as a function of the adsorbed amount and temperature.

- Hydrogen on a silica surface yields an INS spectrum with two rotational peaks at 11 and 14 meV. Both energies are close to the free-rotor transition of the H_2 molecule J:1→0, with an energy of 14.5 meV. Rotational transitions are only observed for bulk hydrogen in the solid state while in the liquid these transitions disappear. The observation of rotational transitions is a clear indication that the first layer of adsorbed hydrogen has properties similar to the solid phase of hydrogen (solid-like).

- The transitions at 11 and 14 meV are explained in terms of a hindered rotation caused by the presence of hydroxyl groups on the silica surface. Using the Evett model of a hindered rotation, the energies were associated to the degenerated rotational-vibrational transitions E[0,0→0,1] and E[0,1→1,0] for a rotational barrier of 1.8 kJ/mol.

- The INS spectrum of hydrogen on graphitized carbon shows only one rotational peak at 14.5 meV showing that the hydrogen molecule has free-rotor transition when is adsorbed on a chemically homogeneous surface, free of hydroxyl groups.

- The high monolayer density observed for all flat surfaces at low-temperature is explained by the H_2-surface interactions that strongly exceed the intermolecular repulsion. *Ab initio* calculations show that the intermolecular H_2-H_2 interaction accounts for 0.6 kJ/mol, significantly less than the 4 kJ/mol adsorption interaction of H_2 with silica. The theoretically calculated intermolecular H_2-H_2 separation of 2.9 Å or a cross-sectional area of 7.5 $Å^2$, is in good agreement with the experimental observations.

- The high densities of adsorbed hydrogen are only possible due to the strong compressibility of the H_2 monolayer caused by the low intermolecular interaction. Because of the absence of core electrons, it is much easier to compress H_2 compared to heavier elements due to the significantly weaker Pauli repulsion of the electron clouds when overlapping upon compression.

Hydrogen adsorption at low-temperature on fragmented surfaces

- The chemically heterogeneous surface of MOF-205 is composed of energetically different adsorption sites forming a fragmented surface, which results in several steps in the H_2 isotherms indicating a filling of the adsorption sites at different pressures.

- The analysis of the hydrogen adsorption isotherms of MOF-205 shows similar monolayer capacities for H_2 and Ar, indicating that the average density of the adsorbed hydrogen at low temperatures ($\sim$76 kg/m^3) is close to the bulk-liquid (70.5 kg/m^3).

- The INS experiments of hydrogen adsorbed on MOF-205 show a complex spectrum composed of several peaks close to the free-rotor (14.5 meV) that appear subsequently with increasing dosing. This indicates that the most favorable adsorption sites are occupied first, and then the weaker sites are subsequently filled.

These systematic experiments together with the calculations by the group of Thomas Heine give an explanation to high H_2 monolayer capacity as a high-density phase of adsorbed hydrogen, which have been observed but never fully understood over the past 70 years. High density adsorbed hydrogen could play an interesting role for cryogenic hydrogen storage systems with extremely high storage capacities.

Hydrogen isotope diffusion in ZIF-8

Hydrogen isotope diffusion was studied at low temperatures using a commercially available adsorption apparatus. A high-resolution device, capable of measure pressures as low as $1{\cdot}10^{-8}$ bar, was coupled to a closed-cycle He cryocooler that reaches H_2 boiling temperatures ($\sim$20 K) providing a high temperature stability $\pm$0.05 K. The diffusion coefficients were obtained analyzing the adsorption kinetic data. ZIF-8 is investigated as model material using two samples with different particle size, monoliths and powders, to directly compare the adsorption kinetics and diffusion in the same pore structure for different particle sizes.

- A model based on the Fick's 2nd law was used to calculate the diffusion coefficients from the adsorption kinetic data. The model was selected to include boundary conditions for spherical porous particles immersed in a gas of finite volume.

- The H_2 and D_2 diffusion coefficients for the monoliths decrease as a function of the uptake. Such reduction, in the molecular transport, is rationalized in terms of a structural transformation of the material upon gas adsorption. In presence of H_2 or D_2, the imidazolate linker of ZIF-8 swings towards the direction of the pore aperture effectively reducing the size.

- A higher D_2 diffusion coefficient compared to H_2 is observed at high uptake and condensation temperature ($\sim$20 K), indicating that the reduction

of the pore aperture not only limits the molecular transport but also enhances the kinetic quantum sieving, resulting in faster transport of the heavier isotope (D_2).

The presented method uses a commercially available adsorption apparatus that measures the adsorption isotherms and simultaneously measures the gas diffusivities at given temperature and gas uptake. Proving, for the first time, that adsorption experiments combined with a fine temperature control can be used to study hydrogen diffusion and isotope separation at temperatures close to condensation.

Appendix A

High-monolayer capacity of H_2 and He

Table A.1 shows the reported values of the monolayer capacity of light gases (He and H_2) adsorbed at low-temperature compared to N_2 or Ar monolayer values. The ratio between monolayer capacities of the light gases (H_2, D_2 or He) and N_2 or Ar was calculated for all reported values. Assuming that the light gases see the same surface area that N_2 or Ar, the monolayer ratio indicates that a light gas (H_2, D_2 or He) can cover the same surface with at least 1.5 times more molecules/atoms than N_2 or Ar.

Table A.1 Reported values of the monolayer capacity of light gases (He and H_2) adsorbed at low-temperature compared to N_2 or Ar monolayer values.

Author	Material	BET normal gas (Ar or N_2)		BET light gas (H_2, D_2 or He)		Ratio
		Monolayer capacity	Specific surface area†	Monolayer Capacity	BET area†	Monolayer ratio◇ $(n_m(He,H_2)/n_m(N_2,Ar))$
Schaeffer *et al.* (1949) [13]	Carbon black (Spheron 6)	N_2(78K) 129.5 cc/g	N_2(78K) 113 m^2/g	He(4.2K) 310.5 cc/g	He(4.2K) 258 m^2/g	$n_m(H_2)/n_m(N_2)$ = 2.2
Schaeffer *et al.* (1949) [13]	Carbon black (Spheron C)	N_2(78K) 260.5 cc/g	N_2(78K) 227 m^2/g	He(4.2K) 569.5 cc/g	He(4.2K) 472 m^2/g	$n_m(He)/n_m(N_2)$ = 2.1
Pace and Siebert (1959) [4]	Graphon	N_2 (77K) 0.9 mmol/g‡	N_2(77 K) 85.9 m^2/g	H_2(20.4K) 2.0 mmol/g‡ D_2(23.5K) 2.2 mmol/g‡	H_2(20.4K) 169 m^2/g D_2(23.5K) 174 m^2/g	$n_m(H_2)/n_m(N_2)$ = 2.2
Brewer and Champeney (1962) [92]	Vycor glass disk	N_2(77K) 25.9 cc/g	N_2(77 K) 113 m^2/g	He(4.2K) 62.5 cc/g He(3.2K) 66.8 cc/g He(2.0K) 75.3 cc/g He(1.8K) 78.3 cc/g	–	$n_m(He(4.2K))/n_m(N_2)$ = 2.4 $n_m(He(3.2K))/n_m(N_2)$ = 2.6 $n_m(He(2.0K))/n_m(N_2)$ = 2.9 $n_m(He(1.8K))/n_m(N_2)$ = 3.0
Huber and Huber (1987) [5, 73]	Vycor glass	N_2(77K) 2.1 mmol/cc	–	H_2(18K) 3.5 mmol/cc	–	$n_m(H_2)/n_m(N_2)$ = 1.7
Setoyama and Kaneko (1995) [118]	Zeolite NaY	N_2(77K) 126 molecules/unit cell	–	He (4.2K) 223 molecules/unit cell	–	$n_m(He)/n_m(N_2)$ = 1.8
Setoyama and Kaneko (1995) [118]	Zeolite KL	N_2(77K) 10 molecules/unit cell	–	He(4.2K) 21.8 molecules/unit cell	–	$n_m(He)/n_m(N_2)$ = 2.2
Edler *et al.* (1997) [11]	MCM-41	N_2(77K) 10.0 mmol/g	N_2(77 K) 980 m^2/g	H_2(21.5K) 15.8 mmol/g	–	$n_m(H_2)/n_m(N_2)$ = 1.6
Tanaka *et al.* (2004) [17]	SWCH	N_2(77K) 9.6 mmol/g	N_2(77 K) 938 m^2/g	H_2(20K) 15.7 mmol/g	H_2(20K)1353 m^2/g	$n_m(H_2)/n_m(N_2)$ = 1.6
Prisk et al. (2014) [74]	MCM-41	N_2(77K) 10.0 mmol/g	N_2(77 K) 979 m^2/g	H_2(19.4K) 15.7 mmol/g	–	$n_m(H_2)/n_m(N_2)$ = 1.6
This work	KIT-6	Ar(87K) 4.2 mmol/g N_2(77K) 4.6 mmol/g	Ar (87K) 359 m^2/g N_2(77K) 450 m^2/g	H_2(20.3K) 8.4 mmol/g D_2(23.1K) 8.6 mmol/g	H_2(20.3K) 719 m^2/g D_2(23.1K) 664 m^2/g	$n_m(H_2)/n_m(Ar)$ = 2.0 $n_m(D_2)/n_m(Ar)$ = 2.0

†Surface areas estimated using the cross-sectional areas, which were calculated from the respective bulk liquid density and hexagonal close-packing N_2 (16.2 $Å^2$), Ar (14.2 $Å^2$), H_2 (14.2 $Å^2$), D_2 (12.9 $Å^2$) and He (15.4 $Å^2$); ‡Calculated based on the reported surface areas by Pace and Siebert [4]; ◇Calculated for this work under the assumption that both molecules see the same surface area, the monolayer capacity ratio indicates how many more molecules (He or H_2) cover the surface compared to Ar or N_2; *.

Appendix B

Kinetic curves of H_2 and D_2

Figure B.1 - B.6 show the kinetic curves of H_2 and D_2 measured at different temperature.

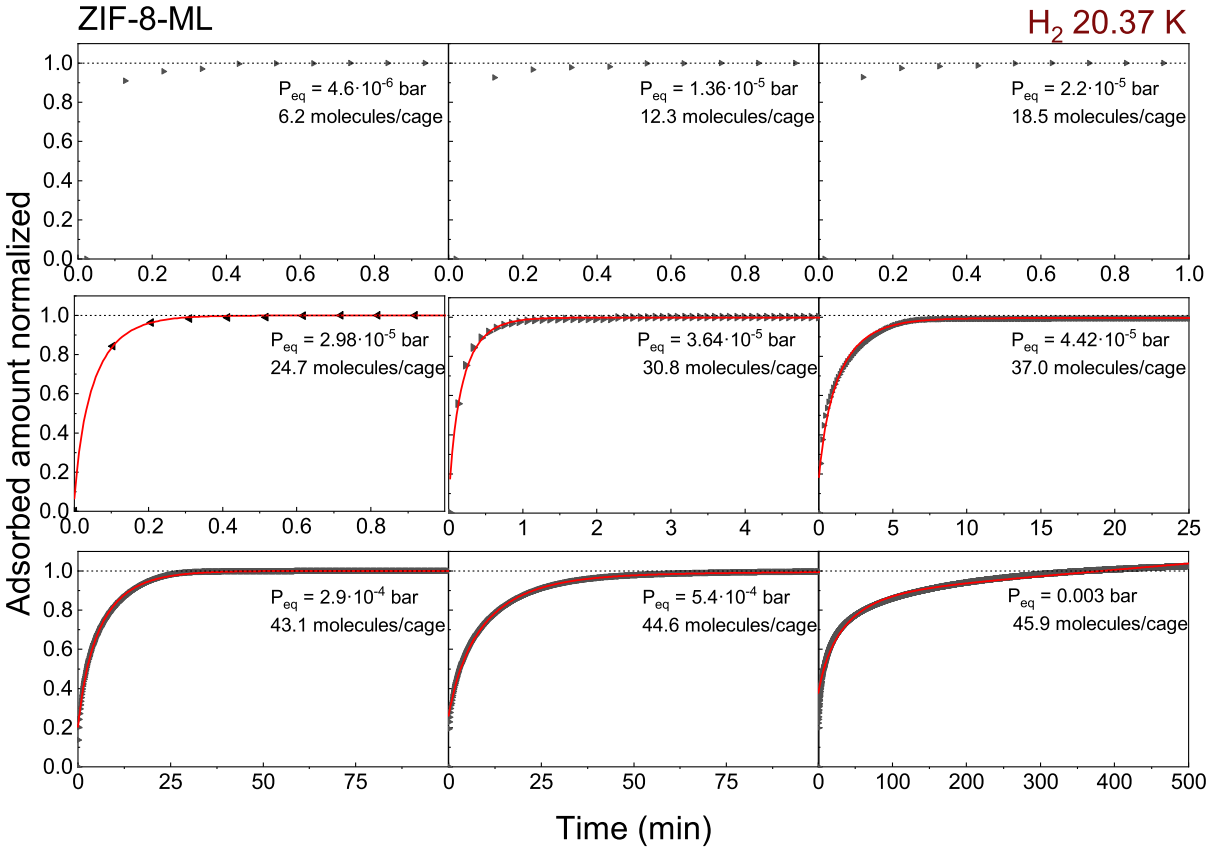

Figure B.1 *H_2 kinetic data of ZIF-8-ML at 20.37 K.* The kinetic data (black triangles) at the respective isotherm point was fitted using the 2nd Fick's law (red line).

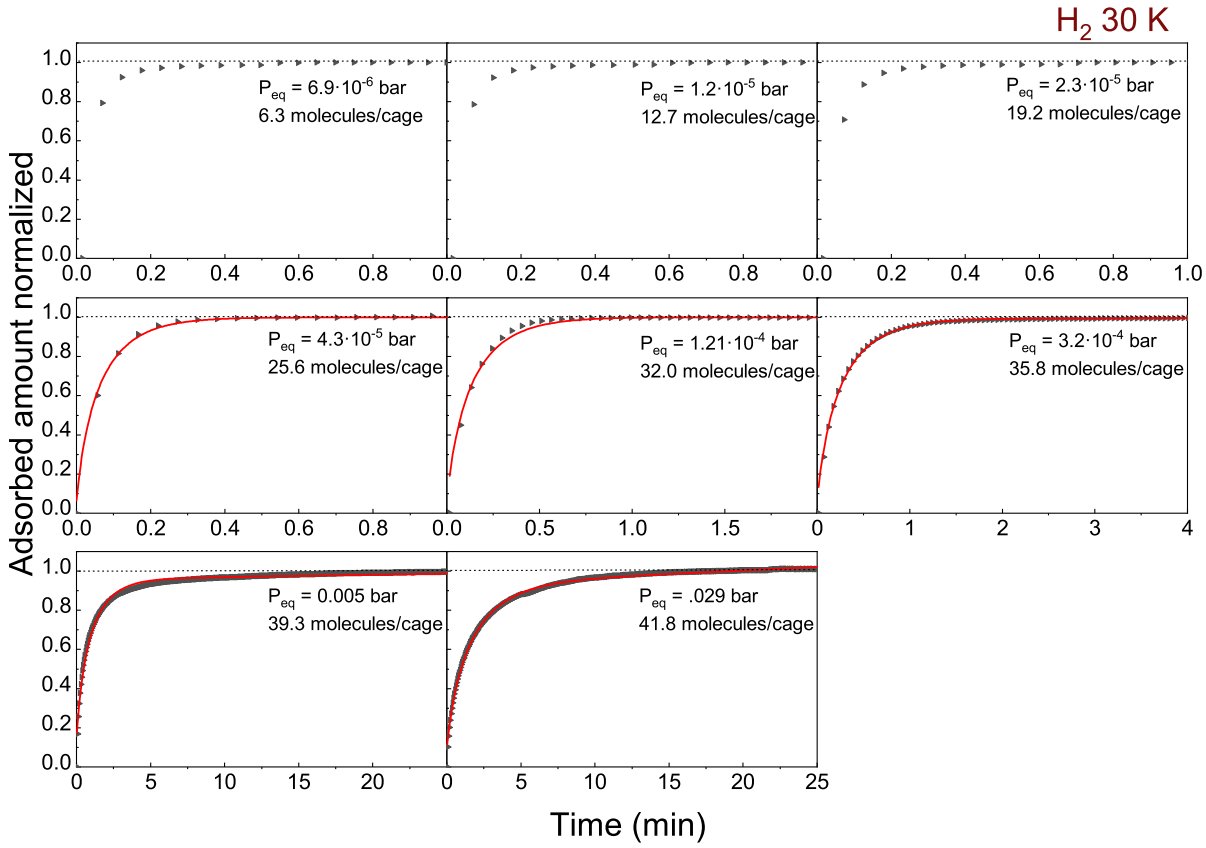

Figure B.2 *H_2 kinetic data of ZIF-8-ML at 30 K.* The kinetic data (black triangles) at the respective isotherm point was fitted using the 2nd Fick's law (red line).

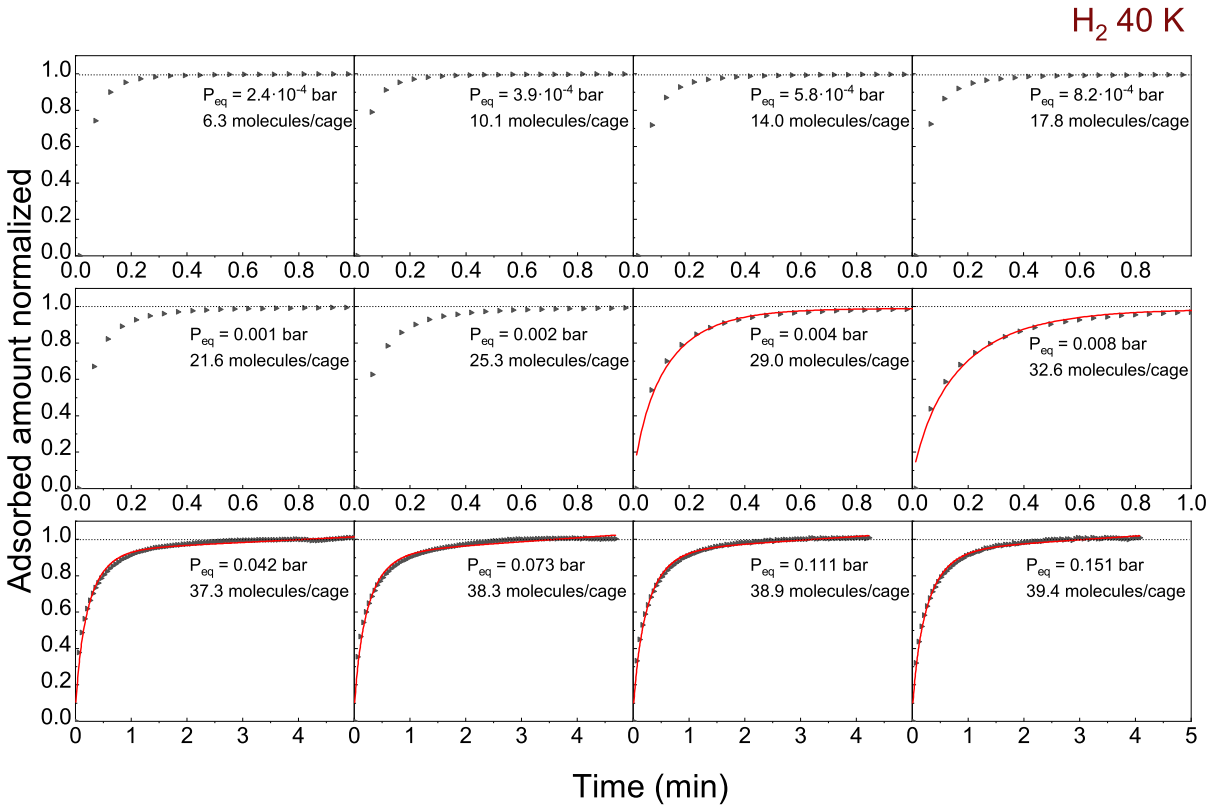

Figure B.3 *H_2 kinetic data of ZIF-8-ML at 40 K.* The kinetic data (black triangles) at the respective isotherm point was fitted using the 2nd Fick's law (red line).

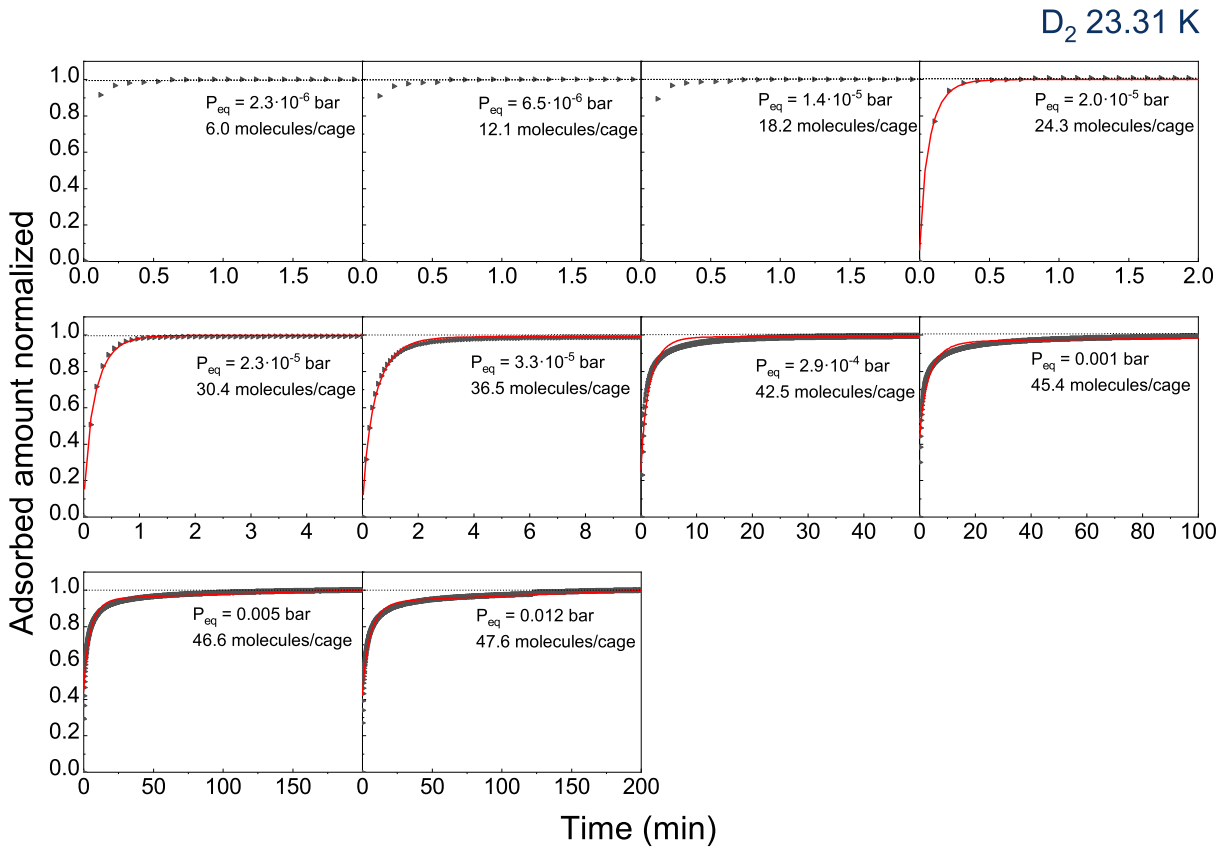

Figure B.4 *D_2 kinetic data of ZIF-8-ML at 23.31 K.* The kinetic data (black triangles) at the respective isotherm point was fitted using the 2nd Fick's law (red line).

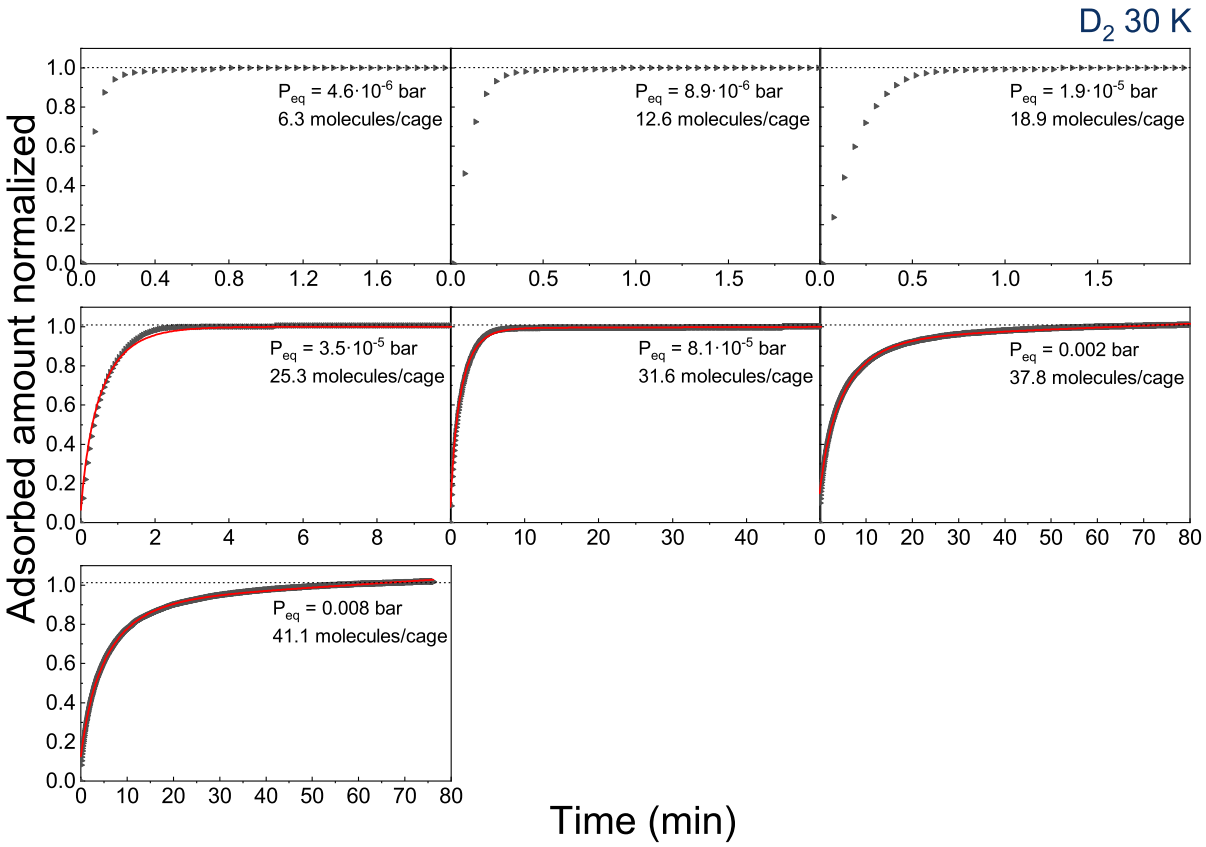

Figure B.5 *D_2 kinetic data of ZIF-8-ML at 30 K.* The kinetic data (black triangles) at the respective isotherm point was fitted using the 2nd Fick's law (red line).

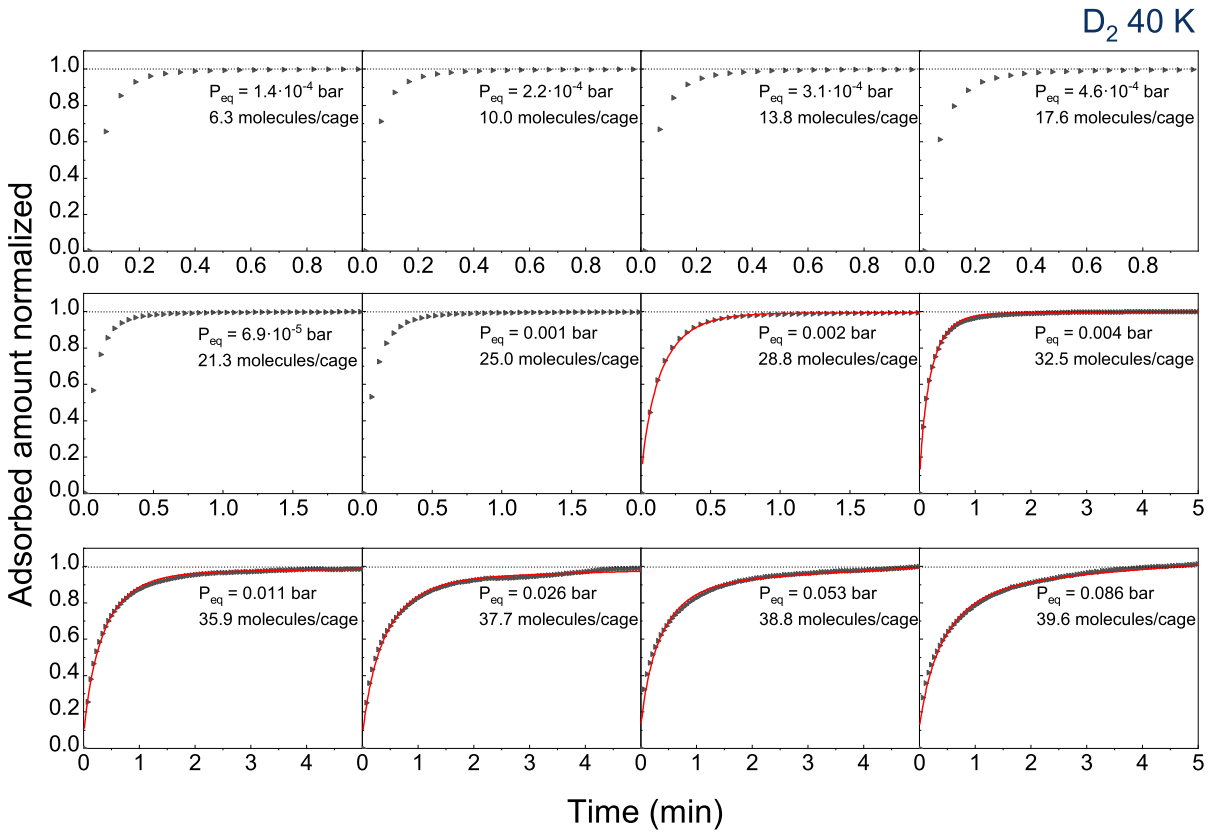

Figure B.6 *D_2 kinetic data of ZIF-8-ML at 40 K.* The kinetic data (black triangles) at the respective isotherm point was fitted using the 2nd Fick's law (red line).

References

[1] M. Hirscher. “Hydrogen Storage by Cryoadsorption in Ultrahigh-Porosity Metal-Organic Frameworks.” *Angewandte Chemie-International Edition* 50.3 (2011), pp. 581–582.

[2] D. P. Broom et al. “Outlook and challenges for hydrogen storage in nanoporous materials.” *Applied Physics A - Materials Science and Processing* 122.3 (2016), p. 151.

[3] R. Balderas-Xicohtencatl, M. Schlichtenmayer, and M. Hirscher. “Volumetric Hydrogen Storage Capacity in Metal-Organic Frameworks.” *Energy Technology* 6.3 (2018), pp. 578–582.

[4] E. L. Pace and A. R. Siebert. “Heat of Adsorption of Parahydrogen and Orthodeuterium on Graphon.” *The Journal of Physical Chemistry* 63.9 (1959), pp. 1398–1400.

[5] T. E. Huber and C. A. Huber. “Vibrational spectroscopy of H_2 in porous Vycor glass: First evidence for the bilayer structure.” *Physical Review Letters* 59.10 (1987), pp. 1120–1123.

[6] T. E. Huber and C. A. Huber. “Adsorption of hydrogen on porous Vycor glass.” *Journal of Low Temperature Physics* 80.5 (1990), pp. 315–323.

[7] Tian Tian et al. “Mechanically and chemically robust ZIF-8 monoliths with high volumetric adsorption capacity.” *Journal of Materials Chemistry A* 3.6 (2015), pp. 2999–3005.

[8] R. Chahine and T. K. Bose. “Characterization and optimization of adsorbents for hydrogen storage.” *Hydrogen Energy Progress Xi, Vols 1-3* (1996), pp. 1259–1263.

[9] B. Panella, M. Hirscher, and S. Roth. “Hydrogen adsorption in different carbon nanostructures.” *Carbon* 43.10 (2005), pp. 2209–2214.

[10] H. W. Langmi et al. “Hydrogen adsorption in zeolites A, X, Y and RHO.” *Journal of Alloys and Compounds* 356 (2003), pp. 710–715.

[11] Karen J. Edler et al. “Structure and dynamics of hydrogen sorption in mesoporous MCM-41.” *Journal of the Chemical Society, Faraday Transactions* 93.8 (1997), pp. 1667–1674.

[12] M. S. Anderson and C. A. Swenson. “Experimental compressions for normal hydrogen and normal deuterium to 25 kbar at 4.2 K.” *Physical Review B* 10.12 (1974), pp. 5184–5191.

[13] W. D. Schaeffer, W. R. Smith, and C. B. Wendell. “The Adsorption of Helium on Carbon Black at Liquid Helium Temperatures.” *Journal of the American Chemical Society* 71.3 (1949), pp. 863–867.

[14] Rudra Pal Singh and William Band. “The Anomalous Monolayer Adsorption of Helium.” *The Journal of Physical Chemistry* 59.7 (1955), pp. 663–665.

[15] William A. Steele. “Concerning a Theory of Multilayer Adsorption, with Particular Reference to Adsorbed Helium.” *The Journal of Chemical Physics* 25.5 (1956), pp. 819–823.

[16] Phong Diep and J. Karl Johnson. “An accurate H2–H2 interaction potential from first principles.” *The Journal of Chemical Physics* 112.10 (2000), pp. 4465–4473.

[17] Hideki Tanaka et al. “Quantum Effects on Hydrogen Adsorption in Internal Nanospaces of Single-Wall Carbon Nanohorns.” *The Journal of Physical Chemistry B* 108.45 (2004), pp. 17457–17465.

[18] J. J. M. Beenakker, V. D. Borman, and S. Y. Krylov. “Molecular-Transport in Subnanometer Pores - Zero-Point Energy, Reduced Dimensionality and Quantum Sieving.” *Chemical Physics Letters* 232.4 (1995), pp. 379–382.

[19] H. Oh et al. “Quantum cryo-sieving for hydrogen isotope separation in microporous frameworks: an experimental study on the correlation between effective quantum sieving and pore size.” *Journal of Materials Chemistry A* 1.10 (2013), pp. 3244–3248.

[20] H. Oh and M. Hirscher. “Quantum Sieving for Separation of Hydrogen Isotopes Using MOFs.” *European Journal of Inorganic Chemistry* 27 (2016), pp. 4278–4289.

[21] Ying-Pin Chen and Hong-Cai Zhou. *Characterization of H2 Adsorption Sites: Where Are the Hydrogens Stored in the Materials?* Nanostructured Materials for Next-Generation Energy Storage and Conversion: Hydrogen Production, Storage, and Utilization. Berlin, Heidelberg: Springer Berlin Heidelberg, 2017, pp. 257–290. ISBN: 978-3-662-53514-1.

[22] R. A. Pollock et al. “Kinetic Trapping of D-2 in MIL-53(Al) Observed Using Neutron Scattering.” *Journal of Physical Chemistry C* 118.31 (2014), pp. 18197–18206.

[23] C. I. Contescu et al. “Isotope Effect on Adsorbed Quantum Phases: Diffusion of H-2 and D-2 in Nanoporous Carbon.” *Physical Review Letters* 110.23 (2013).

[24] T. X. Nguyen, H. Jobic, and S. K. Bhatia. “Microscopic Observation of Kinetic Molecular Sieving of Hydrogen Isotopes in a Nanoporous Material.” *Physical Review Letters* 105.8 (2010).

[25] J. Teufel et al. “MFU-4 - A Metal-Organic Framework for Highly Effective H-2/D-2 Separation.” *Advanced Materials* 25.4 (2013), pp. 635–639.

[26] F. Rouquerol, J. Rouquerol, and K. S. W. Sing. *Adsorption by powders and porous solids: principles, methodology, and applications*. San Diego: Academic Press, 1999, xvi, 467 p.

[27] S. Lowell et al. *Characterization of Porous Solids and Powders: Surface Area, Pore Size and Density*. Particle Technology Series. Springer Netherlands, 2004. ISBN: 1567-827X.

[28] J. W. Leachman et al. “Fundamental Equations of State for Parahydrogen, Normal Hydrogen, and Orthohydrogen.” *Journal of Physical and Chemical Reference Data* 38.3 (2009).

[29] R.D. McCarty. *Correlations for the Thermophysical Properties of Carbon Monoxide*. TechReport. National Institute of Standards and Technology (NIST), 1989.

[30] NIST. “Thermophysical Properties of Fluid Systems.” *Chemistry WebBook, SRD 69, URL:webbook.nist.gov/chemistry/fluid/* (2017).

[31] T. Y. Wei et al. “A review on the characterization of hydrogen in hydrogen storage materials.” *Renewable and Sustainable Energy Reviews* 79 (2017), pp. 1122–1133.

[32] E. MacA Gray. “7 - Reliably measuring hydrogen uptake in storage materials.” In: *Solid-State Hydrogen Storage*. Ed. by Gavin Walker. Woodhead Publishing, 2008, pp. 174–204. ISBN: 978-1-84569-270-4.

[33] C. J. Webb and E. MacA Gray. “Analysis of uncertainties in gas uptake measurements using the gravimetric method.” *International Journal of Hydrogen Energy* 39.13 (2014), pp. 7158–7164.

[34] A. F. Kloutse et al. “Isosteric heat of hydrogen adsorption on MOFs: comparison between adsorption calorimetry, sorption isosteric method, and analytical models (vol 121, pg 1417, 2015).” *Applied Physics A - Materials Science and Processing* 122.6 (2016).

[35] Nuno Bimbo et al. “Analysis of hydrogen storage in nanoporous materials for low carbon energy applications.” *Faraday Discussions* 151.0 (2011), pp. 59–74.

[36] M. Thommes et al. “Physisorption of gases, with special reference to the evaluation of surface area and pore size distribution (IUPAC Technical Report).” *Pure and Applied Chemistry* 87.9-10 (2015), pp. 1051–1069.

[37] K. S. W. Sing et al. “Reporting Physisorption Data for Gas Solid Systems with Special Reference to the Determination of Surface-Area and Porosity (Recommendations 1984).” *Pure and Applied Chemistry* 57.4 (1985), pp. 603–619.

[38] S. Brunauer, P. H. Emmett, and E. Teller. “Adsorption of gases in multimolecular layers.” *Journal of the American Chemical Society* 60 (1938), pp. 309–319.

[39] Alexander V. Neimark, Kenneth S. W. Sing, and Matthias Thommes. “Surface Area and Porosity.” In: *Handbook of Heterogeneous Catalysis*. Wiley-VCH, 2008. ISBN: 9783527610044.

[40] Titus S. van Erp and Johan A. Martens. “A standardization for BET fitting of adsorption isotherms.” *Microporous and Mesoporous Materials* 145.1–3 (2011), pp. 188–193.

[41] M. Thommes and K. A. Cychosz. “Physical adsorption characterization of nanoporous materials: progress and challenges.” *Adsorption-Journal of the International Adsorption Society* 20.2-3 (2014), pp. 233–250.

[42] J. Rouquerol, P. Llewellyn, and F. Rouquerol. “Is the BET equation applicable to microporous adsorbents?” In: *Studies in Surface Science and Catalysis*. Ed. by F. Rodriquez-Reinoso J. Rouqerol P.L. Llewellyn and N. Seaton. Vol. Volume 160. Elsevier, 2007, pp. 49–56. ISBN: 9780444520227.

[43] M. Thommes. “Textural Characterization of Zeolites and Ordered Mesoporous Materials by Physical Adsorption.” *Introduction to Zeolite Science and Practice* 168 (2007), pp. 495–523.

[44] P. A. Monson. “Understanding adsorption/desorption hysteresis for fluids in mesoporous materials using simple molecular models and classical density functional theory.” *Microporous and Mesoporous Materials* 160 (2012), pp. 47–66.

[45] Matthias Thommes. *Pore Size Analysis by Gas Adsorption Part I: Aspects of the Application of Density Functional Theory (DFT) and Monte Carlo simulation (MC) for micro/mesopore size analysis*. TechReport.

[46] Instruments Quantachrome. *State-of-the-Art Zeolite Characterization: Argon Adsorption at 87.3 K and Advanced Density Functional Theory Methods (NLDFT, QSDFT)*. TechReport.

[47] Andreas Züttel. "Materials for hydrogen storage." *Materials Today* 6.9 (2003), pp. 24–33.

[48] A. Zuttel et al. "Hydrogen density in nanostructured carbon, metals and complex materials." *Materials Science and Engineering B* 108.1-2 (2004), pp. 9–18.

[49] D. Pukazhselvan, V. Kumar, and S. K. Singh. "High capacity hydrogen storage: Basic aspects, new developments and milestones." *Nano Energy* 1.4 (2012), pp. 566–589.

[50] Jorg Kärger and Douglas M. Ruthven. *Diffusion in zeolites and other microporous solids*. New York: Wiley, 1992, xxxiv, 605 p. ISBN: 0471509078 (alk. paper).

[51] John Crank. *The mathematics of diffusion*. 2d. Oxford, Eng: Clarendon Press, 1975, viii, 414 p. ISBN: 0198533446.

[52] B. S. Hudson. "Vibrational spectroscopy using inelastic neutron scattering: Overview and outlook." *Vibrational Spectroscopy* 42.1 (2006), pp. 25–32.

[53] A. J. Dianoux, G. H. Lander, and Institut Laue-Langevin. *Neutron data booklet*. 2nd. Philadelphia, PA: Old City, 2003. ISBN: 0970414374.

[54] Timmy Ramirez-Cuesta. "Neutron Vibration Spectroscopy." *Online Multimedia (Presentation), Courtesy of Oak Ridge National Laboratory, U.S. Dept. of Energy, URL: neutrons.ornl.gov/sites/default/files/Timmy_ Ramirez_ NXS_ 2018.pdf* (2018), pp. 1–64.

[55] Roger Pynn. *neutron scattering: A primer*. Los Alamos Science. 1990.

[56] P. C. H. Mitchell et al. *Vibrational spectroscopy with neutrons : with applications in chemistry, biology, materials science and catalysis*. Series on neutron techniques and applications. Hackensack, NJ: World Scientific, 2005, xxvi, 642 p. ISBN: 9812560130.

[57] P. A. Georgiev et al. "Hydrogen site occupancies in single-walled carbon nanotubes studied by inelastic neutron scattering." *Journal of Physics-Condensed Matter* 16.8 (2004), pp. L73–L78.

[58] A. Requena, R. Peña, and A. Serna. “Perturbation for a rigid rotator in an electric field.” *International Journal of Quantum Chemistry* 22.6 (1982), pp. 1263–1270.

[59] Isaac F. Silvera. “The solid molecular hydrogens in the condensed phase: Fundamentals and static properties.” *Reviews of Modern Physics* 52.2 (1980), pp. 393–452.

[60] Qinyu Wang et al. “Quantum Sieving in Carbon Nanotubes and Zeolites.” *Physical Review Letters* 82.5 (1999), pp. 956–959.

[61] S. R. Challa, D. S. Sholl, and J. K. Johnson. “Light isotope separation in carbon nanotubes through quantum molecular sieving.” *Physical Review B* 63.24 (2001).

[62] Y. Hattori et al. “Quantum sieving effect of modified activated carbon fibers on H-2 and D-2 adsorption at 20 K.” *Journal of Physical Chemistry B* 110.20 (2006), pp. 9764–9767.

[63] H. Kagita et al. “Quantum Molecular Sieving Effects of H-2 and D-2 on Bundled and Nonbundled Single-Walled Carbon Nanotubes.” *Journal of Physical Chemistry C* 116.39 (2012), pp. 20918–20922.

[64] A. Gotzias et al. “Experimental and theoretical study of D-2/H-2 quantum sieving in a carbon molecular sieve.” *Adsorption-Journal of the International Adsorption Society* 19.2-4 (2013), pp. 373–379.

[65] A. J. Lachawiec, T. R. DiRaimondo, and R. T. Yang. “A robust volumetric apparatus and method for measuring high pressure hydrogen storage properties of nanostructured materials.” *Review of Scientific Instruments* 79.6 (2008).

[66] R. Radebaugh. “Cryocoolers: the state of the art and recent developments.” *Journal of Physics-Condensed Matter* 21.16 (2009).

[67] W. V. Loebenstein. “Calculations and Comparisons of Nonideal Gas Corrections for Use in Gas Adsorption.” *Journal of Colloid and Interface Science* 36.3 (1971), p. 397.

[68] Maurice Ulrich Schlichtenmayer. “Wasserstoffspeicherkapazität poröser Materialien in Kryoadsorptionstanks.” Thesis. 2012.

[69] ORNL. “Courtesy of Oak Ridge National Laboratory, U.S. Dept. of Energy, URL: neutrons.ornl.gov/vision.” Accessed: April 2018 (2018).

[70] D. D. Betts, F. D. Manchester, and E. J. Woods. “Adsorbed helium as a quantum fluid.” *Physics Letters* 10.1 (1964), pp. 59–61.

[71] Adrien Noury et al. “Layering Transition in Superfluid Helium Adsorbed on a Carbon Nanotube Mechanical Resonator.” *Physical Review Letters* 122.16 (2019), p. 165301.

[72] Lothar Meyer. “First Adsorbed Layer of Helium.” *Physical Review* 103.6 (1956), pp. 1593–1596.

[73] T. E. Huber and C. A. Huber. “Vibrational spectroscopy of porous Vycor glass: surface hydroxyl perturbations upon adsorption of hydrogen.” *The Journal of Physical Chemistry* 94.6 (1990), pp. 2505–2511.

[74] T. R. Prisk, M. S. Bryan, and P. E. Sokol. “Diffusive and rotational dynamics of condensed n-H2 confined in MCM-41.” *Physical Chemistry Chemical Physics* 16.33 (2014), pp. 17960–17974.

[75] A. Vinu et al. “Three-Dimensional Ultralarge-Pore Ia3d Mesoporous Silica with Various Pore Diameters and Their Application in Biomolecule Immobilization.” *Chemistry-a European Journal* 14.36 (2008), pp. 11529–11538.

[76] L. Almar et al. “High-temperature long-term stable ordered mesoporous Ni–CGO as an anode for solid oxide fuel cells.” *Journal of Materials Chemistry A* 1.14 (2013), pp. 4531–4538.

[77] F. Kleitz, S. H. Choi, and R. Ryoo. “Cubic Ia3d large mesoporous silica: synthesis and replication to platinum nanowires, carbon nanorods and carbon nanotubes.” *Chemical Communications* 17 (2003), pp. 2136–2137.

[78] Changbum Jo, Kyoungsoo Kim, and Ryong Ryoo. “Syntheses of high quality KIT-6 and SBA-15 mesoporous silicas using low-cost water glass, through rapid quenching of silicate structure in acidic solution.” *Microporous and Mesoporous Materials* 124.1–3 (2009), pp. 45–51.

[79] N. Suzuki, S. Kiba, and Y. Yamauchi. “Fabrication of mesoporous silica KIT-6/polymer composite and its low thermal expansion property.” *Materials Letters* 65.3 (2011), pp. 544–547.

[80] W. Stober, A. Fink, and E. Bohn. “Controlled Growth of Monodisperse Silica Spheres in Micron Size Range.” *Journal of Colloid and Interface Science* 26.1 (1968), pp. 62–69.

[81] S. Jun et al. “Synthesis of new, nanoporous carbon with hexagonally ordered mesostructure.” *Journal of the American Chemical Society* 122.43 (2000), pp. 10712–10713.

[82] R. Ryoo et al. “Ordered mesoporous carbons.” *Advanced Materials* 13.9 (2001), pp. 677–681.

[83] Minkee Choi and Ryong Ryoo. “Ordered nanoporous polymer-carbon composites.” *Nat Mater* 2.7 (2003), pp. 473–476.

[84] I. V. Ponomarenko et al. “Template synthesis of CMK-3 nanostructured carbon material and study of its properties.” *Glass Physics and Chemistry* 40.1 (2014), pp. 79–87.

[85] J. Rouquerol et al. *Recommendations for the characterization of porous solids (Technical Report)*. TechReport 13653075. 1994.

[86] L. Gurvich. “Physico-chemical attractive force.” *J. Phys. Chem. Soc. Russ.* 47 (1915), pp. 805–827.

[87] Michal Kruk et al. “Nitrogen Adsorption Study of Surface Properties of Graphitized Carbon Blacks.” *Langmuir* 15.4 (1999), pp. 1435–1441.

[88] P. C. Ball and R. Evans. “Structure and adsorption at gas–solid interfaces: Layering transitions from a continuum theory.” *The Journal of Chemical Physics* 89.7 (1988), pp. 4412–4423.

[89] Brian K. Peterson et al. “Layering transitions in cylindrical pores.” *The Journal of Chemical Physics* 93.1 (1990), pp. 679–685.

[90] L. Xu, C. H. Wang, and J. Q. Guan. “Preparation of acid-base bifunctional mesoporous KIT-6 (KIT: Korea Advanced Institute of Science and Technology) and its catalytic performance in Knoevenagel reaction.” *Journal of Solid State Chemistry* 213 (2014), pp. 250–255.

[91] A. K. Ladavos et al. “The BET equation, the inflection points of N2 adsorption isotherms and the estimation of specific surface area of porous solids.” *Microporous and Mesoporous Materials* 151.0 (2012), pp. 126–133.

[92] D. F. Brewer and D. C. Champeney. “Sorption of Helium and Nitrogen on Vycor Porous Glass.” *Proceedings of the Physical Society* 79.4 (1962), p. 855.

[93] Marvin Ross and William A. Steele. “Multilayer Adsorption of Helium on Argon.” *The Journal of Chemical Physics* 35.3 (1961), pp. 871–882.

[94] L. T. Zhuravlev. “Concentration of hydroxyl groups on the surface of amorphous silicas.” *Langmuir* 3.3 (1987), pp. 316–318.

[95] A. A. Evett. “Comparison of Exact and Approximate Energy Levels for a Hindered Rotator.” *Journal of Chemical Physics* 31.5 (1959), pp. 1419–1420.

[96] A. A. Evett. “Hindered Rotator Model for Adsorbed Hydrogen at Low Temperatures.” *Journal of Chemical Physics* 31.2 (1959), pp. 565–566.

[97] P. J. R. Honeybone et al. “Inelastic Neutron-Scattering of Molecular-Hydrogen in Amorphous Hydrogenated Carbon.” *Chemical Physics Letters* 180.3 (1991), pp. 145–148.

[98] Raina J. Olsen et al. “Quantum excitation spectrum of hydrogen adsorbed in nanoporous carbons observed by inelastic neutron scattering.” *Carbon* 58 (2013), pp. 46–58.

[99] Ievgeniia Savchenko et al. “Nuclear quantum effects on adsorption of H2 and isotopologues on metal ions.” *Chemical Physics Letters* 670 (2017), pp. 64–70.

[100] I. Weinrauch et al. “Capture of heavy hydrogen isotopes in a metal-organic framework with active Cu(I) sites.” *Nat Commun* 8 (2017), p. 14496.

[101] N. Klein et al. “A Mesoporous Metal-Organic Framework.” *Angewandte Chemie-International Edition* 48.52 (2009), pp. 9954–9957.

[102] H. Furukawa et al. “Ultrahigh Porosity in Metal-Organic Frameworks.” *Science* 329.5990 (2010), pp. 424–428.

[103] H. Lee et al. “Liquid-Like Hydrogen Stored in Nanoporous Materials at 50 K Observed by in Situ Neutron Diffraction Experiments.” *Journal of Physical Chemistry C* 117.6 (2013), pp. 3177–3184.

[104] B. Streppel and M. Hirscher. “BET specific surface area and pore structure of MOFs determined by hydrogen adsorption at 20 K.” *Physical Chemistry Chemical Physics* 13.8 (2011), pp. 3220–3222.

[105] T. Duren et al. “Calculating geometric surface areas as a characterization tool for metal-organic frameworks.” *Journal of Physical Chemistry C* 111.42 (2007), pp. 15350–15356.

[106] A. Uzun and S. Keskin. “Site characteristics in metal organic frameworks for gas adsorption.” *Progress in Surface Science* 89.1 (2014), pp. 56–79.

[107] T. Yildirim and M. R. Hartman. “Direct observation of hydrogen adsorption sites and nanocage formation in metal-organic frameworks.” *Physical Review Letters* 95.21 (2005).

[108] Samantha K. Callear et al. “High-resolution inelastic neutron scattering and neutron powder diffraction study of the adsorption of dihydrogen by the Cu(II) metal–organic framework material HKUST-1.” *Chemical Physics* 427.0 (2013), pp. 9–17.

[109] K. S. Park et al. “Exceptional chemical and thermal stability of zeolitic imidazolate frameworks.” *Proceedings of the National Academy of Sciences of the United States of America* 103.27 (2006), pp. 10186–10191.

[110] X. C. Huang et al. “Ligand-directed strategy for zeolite-type metal-organic frameworks: Zinc(II) imidazolates with unusual zeolitic topologies.” *Angewandte Chemie-International Edition* 45.10 (2006), pp. 1557–1559.

[111] H. Bux et al. “Zeolitic Imidazolate Framework Membrane with Molecular Sieving Properties by Microwave-Assisted Solvothermal Synthesis.” *Journal of the American Chemical Society* 131.44 (2009), pp. 16000–+.

[112] D. Fairen-Jimenez et al. “Flexibility and swing effect on the adsorption of energy-related gases on ZIF-8: combined experimental and simulation study.” *Dalton Transactions* 41.35 (2012), pp. 10752–10762.

[113] D. Fairen-Jimenez et al. “Opening the Gate: Framework Flexibility in ZIF-8 Explored by Experiments and Simulations.” *Journal of the American Chemical Society* 133.23 (2011), pp. 8900–8902.

[114] Mirian Casco et al. “Gate-opening effect in ZIF-8: First experimental proof using inelastic neutron scattering.” *Chemical Communications* (2016).

[115] G. Blanita et al. “Kinetics of hydrogen adsorption in MIL-101 single pellets.” *International Journal of Hydrogen Energy* 42.5 (2017), pp. 3064–3077.

[116] E. Pantatosaki et al. “Probing the hydrogen equilibrium and kinetics in zeolite imidazolate frameworks via molecular dynamics and quasi-elastic neutron scattering experiments.” *Journal of Chemical Physics* 138.3 (2013).

[117] C. Chmelik et al. “Adsorption and Diffusion - Basis for Molecular Understanding of Permeation through Molecular Sieve Membranes.” *Chemie Ingenieur Technik* 83.1-2 (2011), pp. 104–112.

[118] N. Setoyama and K. Kaneko. “Density of He adsorbed in micropores at 4.2K.” *Adsorption* 1.2 (1995), pp. 165–173.

List of publications

1. Kloutse, A. F., R. Zacharia, D. Cossement, R. Chahine, R. Balderas-Xicohtencatl, H. Oh, B. Streppel, M. Schlichtenmayer and M. Hirscher (2015). *"Isosteric heat of hydrogen adsorption on MOFs: comparison between adsorption calorimetry, sorption isosteric method, and analytical models."* **Applied Physics A - Materials Science and Processing** 121(4): 1417-1424.

2. Kim, J. Y., R. Balderas-Xicohtencatl, L. Zhang, S. G. Kang, M. Hirscher, H. Oh and H. R. Moon (2017). *"Exploiting Diffusion Barrier and Chemical Affinity of Metal-Organic Frameworks for Efficient Hydrogen Isotope Separation."* **Journal of the American Chemical Society** 139(42): 15135-15141.

3. Kim, J. Y., L. Zhang, R. Balderas-Xicohtencatl, J. Park, M. Hirscher, H. R. Moon and H. Oh (2017). *"Selective Hydrogen Isotope Separation via Breathing Transition in MIL-53(Al)."* **Journal of the American Chemical Society** 139(49): 17743-17746.

4. Oh, H., S. Maurer, R. Balderas-Xicohtencatl, L. Arnold, O. V. Magdysyuk, G. Schutz, U. Muller and M. Hirscher (2017). *"Efficient synthesis for large-scale production and characterization for hydrogen storage of ligand exchanged MOF-74/174/184-M (M = Mg^{2+}, Ni^{2+})."* **International Journal of Hydrogen Energy** 42(2): 1027-1035.

5. Vilela, D., A. C. Hortelao, R. Balderas-Xicohtencatl, M. Hirscher, K. Hahn, X. Ma and S. Sanchez (2017). *"Facile fabrication of mesoporous silica micro-jets with multi-functionalities."* **Nanoscale** 9(37): 13990-13997.

6. Balderas-Xicohtencatl, R., M. Schlichtenmayer and M. Hirscher (2018). *"Volumetric Hydrogen Storage Capacity in Metal-Organic Frameworks."* **Energy Technology** 6(3): 578-582.

7. Balderas-Xicohténcatl, R., P. Schmieder, D. Denysenko, D. Volkmer and M. Hirscher (2018). *"High Volumetric Hydrogen Storage Capacity using Interpenetrated Metal-Organic Frameworks."* **Energy Technology** 6(3): 510-512.

8. Minuto, F. D., R. Balderas-Xicohtencatl, A. Policicchio, M. Hirscher and R. G. Agostino (2018). *"Assessment methodology of promising porous materials for near ambient temperature hydrogen storage applications."* **International Journal of Hydrogen Energy** 43(31): 14550-14556.

9. Xiong, R., R. Balderas Xicohténcatl, L. Zhang, P. Li, Y. Yao, G. Sang, C. Chen, T. Tang, D. Luo and M. Hirscher (2018). *"Thermodynamics, kinetics and selectivity of H_2 and D_2 on zeolite 5Å below 77K."* **Microporous and Mesoporous Materials** 264: 22-27.

10. Katherine Hurst, Thomas Gennett, Jesse Adams, Mark D. Allendorf, Rafael Balderas-Xicohtencatl, Marek Bielewski, Bryce Edwards, Laura Espinal, Brent Fultz, Michael Hirscher, M. Sterlin L. Hudson, Zeric Hulvey, Michel LaTroche, Di-Jia Liu, Matthew Kapelewski, Emilio Napolitano, Zachary Perry, Justin Purewal, Vitalie Stavila, Mike Veenstra, James L. White, Yuping Yuan, Hong-Cai Zhou, Claudia Zlotea and Philip Parilla (2019). *"An International Laboratory Comparison Study of Volumetric and Gravimetric Hydrogen Adsorption Measurements"*, **ChemPhysChem** 20, 1-14.

11. Ming Liu, Linda Zhang, Marc A. Little,Venkat Kapil, Siyuan Yang, Michele Ceriotti, Lifeng Ding, Daniel L. Holden, Rafael Balderas-Xicohténcatl, Donglin He, Rob Clowes, Samantha Y. Chong, Gisela Schütz, Linjiang Chen, Michael Hirscher, Andrew I. Cooper (2019). *"Barely porous organic cages for hydrogen isotope separation"*, **Science** 366, 613-620.

In preparation

- Rafael Balderas-Xicohténcatl, Luke Daemen, Hung-Hsuan Lin, Katie A. Cychosz, Rémy Guillet-Nicolas, Yongqiang Cheng, Gisela Schütz, Thomas Heine, Anibal J. Ramirez-Cuesta, Matthias Thommes, Michael Hirscher. *"High-density two-dimensional hydrogen"*, in preparation.
- Rafael Balderas-Xicohténcatl, Matthias Thommes, Michael Hirscher *"Hydrogen layering transition on graphitized carbon"*, in preparation.
- Rafael Balderas-Xicohténcatl, Tian Tian, David Fairen-Jimenez, Michael Hirscher. *"Hydrogen isotope diffusion in ZIF-8 monoliths by a volumetric adsorption experiment"*, in preparation.

Acknowledgements

Especial thanks to Dr. Michael Hirscher for his supervision and support throughout this work, for the discussions and guidance, and for the opportunity that he gave me to come to Germany and work in his research group.
Most of the work was carried out in the department for Modern Magnetic Systems at Max Planck Institute for Intelligent Systems, I especially thank Prof. Dr. Gisela Schütz for all the support and encouragement that I received during these years, for the time and dedication she invested to review this work and for the valuable comments that highly improved this work.
Timmy Ramirez, Luke Daemen and Cheng Yonqiang from ORNL that synthesized the Silica-P and Silica-NP samples. Thank you for the expert guidance and support for the neutron scattering experiments that were done at VISION.
Matthias Thommes, Katie Cychosz and Remmy Guillet-Nicolas provided several samples of porous silica and carbon. Thank you for the discussions and valuable insight concerning the adsorption results.
Thomas Heine, Hung-Hsuan Lin and Christian Lurz from Dresden University for the discussions and their theoretical work, which is a fundamental part of the description of the phenomena studied in this work. David Fairen and Tian Tian from Cambridge University for the discussion and for providing the unique samples of ZIF-8. Stephan Muller from BASF for providing the sample MOF-205.
Group members and alumni: Hyunchul Oh, Linda Zhang, Ingrid Zaiser, Nadine Kotzur, Linda Bondorf for the support, nice discussion and friendship. Bern

Ludescher for the expert technical support and the incredible travel stories that he shared with me.
To all my Stuttgart friends (Nese, Matt, Graham, Valentino, Umut, Ekin, Filipa, Moni, Hana, Jeni and many more) you made this time abroad a fun and wonderful adventure.
To Dr. Ciro Falcony and the members of his group, without you, I would have never come here.
To Deniz Görk, for the love, affection, encouragement, and patience. Thank you my love.

Especial thanks to my sister, you have always understood me like no one. Especial thanks to my mother, you have always guided my thoughts. Especial thanks to my father, you have always guided my actions and you have taught me how to understand the world. All I am I owe to you. During all these years far away from you, you all were always close to me.

Gracias por toda su ayuda y apoyo
THANKS FOR ALL YOUR HELP AND SUPPORT
Vielen Dank für Ihre Hilfe und Unterstützung
Tlasojkamati uel miek
Kuajnu'un xaan - Tixa'vi i̲ tixa'vi

Táxi'vi ni̲ tixa'vi nda'á Ndióxi̲ chi xi̲ndáá ra̲ ye̲'e̲
kŏó ya̲ ndíndóó i̲ ndi̲xa'an i̲ inka núú ◇

◇ *Translation from Mixtec to Spanish* - Doy muchas gracias a Dios por que me cuidó; no me pasó nada cuando fuí a otro país.